Energy Storage and Conversion

https://ojs.acad-pub.com/index.php/esc

2024 VOLUME 2 ISSUE 4
ISSN: 3029-2778 (Online)

4

Editorial Team

Editor-in-Chief

Associate Editor

Editorial Board Members

Muhammad Shahzad Nazir
Huaiyin Institute of Technology
China

Rahim Zahedi
University of Tehran
Iran

Yong Wang
Shanghai University
China

Volume 2 Issue 4 • 2024

Energy Storage and Conversion

ACADEMIC
ACADEMIC PUBLISHING PTE LTD

2024 | Volume 2 | Issue 4

Energy Storage and Conversion

https://ojs.acad-pub.com/index.php/esc

Contents

Articles

Reviews

Energy Storage and Conversion 2024, 2(4), 562.
https://doi.org/10.59400/esc.v2i4.562

Article

Tailored copper doped indium sulfide nanostructures as electrode material for supercapacitor and nano photocatalyst for dye degradation

K. Lilly Mary[1,*], D. Geetha[1,*], P.S. Ramesh[2]

[1] Department of Physics, Annamalai University, Chidambaram, Tamil Nadu 608002, India
[2] Thiru Kolanjiappar Government Arts College, Virudhachalam, Tamil Nadu 606001, India
*** Corresponding authors:** K.Lilly Mary, lillyjoy1305@gmail.com; D.Geetha, geeramphyau@gmail.com

CITATION

Mary KL, Geetha D, Ramesh PS. Tailored copper doped indium sulfide nanostructures as electrode material for supercapacitor and nano photocatalyst for dye degradation. Energy Storage and Conversion. 2024; 2(4): 562. https://doi.org/10.59400/esc.v2i4.562

ARTICLE INFO

Received: 21 February 2024
Accepted: 18 September 2024
Available online: 3 October 2024

Abstract: The unique copper-doped indium sulfide nanocrystals are synthesized by a gentle hydrothermal process. XRD, FTIR, XPS, FESEM/EDX, UV-DRS, and PL were used to characterize the final samples. Copper-doped indium sulfide nanostructures can be exploited as an active catalyst in photodegradation and as an electroactive material in supercapacitors due to their distinctive architecture. The copper-doped indium sulfide catalyst exhibits 85 percent photodegradation using methylene blue dye under natural sunlight irradiation, and the electrochemical test showed a capacitance of 668 Fg^{-1} at 1 Ag^{-1} in a 2 M KOH electrolyte solution. For future generations, photocatalyst and electrode can function as more desirable materials.

Keywords: copper-doped indium sulfide; supercapacitors; methylene blue; photodegradation

1. Introduction

Nano-sized semiconducting materials are great interest in materials research due to their size- and shape-dependent optical, electrical, and catalytic characteristics. In particular, Cadmium and lead chalcogenides have been the topic of extensive investigation during the last 20 years [1,2]. Despite their fascinating properties, the toxicity of cadmium and lead limits their potential for widespread application. As a result, tertiary and quaternary materials such as semiconductors based on copper, indium, zinc, and tin scientific interest as potential alternatives. Indium sulfide, a major group III-VI semiconductor, has shown potential for solar applications, band gap energy (2.0–2.4 eV), excellent transparency photoconductive behaviour. Energy and environmental crises are the most pressing issues of the twenty-first century, and indium sulfide, an n-type semiconductor that had most stability at room temperature, is being investigated as a potential photoconductive material as replacement material for hazardous CdS [3,4]. As a result, photocatalytic technology is a desired way for generating renewable energy and cleaning up the environment [5–7]. Photocatalytic water splitting is a successful approach for producing solar hydrogen [8–10]. Several photocatalysts have been thoroughly researched up to this point for both pollutant oxidation and hydrogen production.

The indium sulfide photocatalyst is a viable option among photocatalytic materials with advantageous properties that can be used in a variety of environmental and energy applications. Only one review study in the Journal of Photochemistry and Photobiology [11] discusses indium sulfide as a photocatalyst for solar energy conservation. The Scopus database was searched over the last ten years to assess the most recent works on indium sulfide as a photocatalyst. It was observed that indium

sulfide is a potent catalyst for numerous photocatalytic purposes.

In view of the growing need for electric energy especially the portable consumer electronics and hybrid electric vehicles, there has been a worldwide interest in developing new type of electrode materials [12]. In terms of power density is higher than previous electrode, quick charge-discharge process, and extended lifespan, supercapacitors and ultracapacitors are emerging as a new force in the field of energy storage devices. The charge storage mechanism is mostly awaited in energy storage, supercapacitors are classified into two types: electrical double-layer capacitors controlled by the charge of electrostatic forces separates in the electrode/electrolyte interface and pseudo capacitors controlled at the electrode interface by faradic processes [13]. Supercapacitors have several advantages over traditional electric storage devices, including the capacity to deliver up to 10 times the power of batteries, fast charging in seconds, and high long-cycle stability. These characteristics lend themselves to useful applications. The properties of the electrode materials employed in ultracapacitors have a significant impact on their capacitive performance [14]. Nano powders properties are improved by Doping of metal ions. The standard hydrothermal approach is employed in this study to produce both pure and Cu-doped InS nanoparticles. In addition to sol-gel processing, hydrothermal, co-precipitation, chemical vapor deposition, and microemulsion methods have been used to successfully manufacture indium sulfide nanoparticles. The hydrothermal approach is frequently used to create pure and doped nanoparticles (NPs) at room temperature and at a reasonable cost [15–17]. Cu-doped InS nanoparticles were synthesized using a simple hydrothermal approach for application in electrochemical and photocatalytic processes, and the effects of the dopants on the materials generated were investigated. The Cu (0.1) g-doped indium sulfide nano samples developed are suitable for use in energy storage applications.

2. Experimental approaches

2.1. Materials and methods

Indium chloride ($InCl_3$), thiourea $CS(NH_2)_2$, oxalic acid, ammonia, copper (II) chloride ($CuCl_2$) reagents were purchased from Sigma Aldrich and utilized without further purification

2.2. Copper-doped indium sulfide synthesis

To make a standardized solution, 25 mmol of indium chloride, 350 mmol of thiourea, and 25 mL of filtered water were mixed in a conical flask and constantly swirled. After 10 min, reducing and complexing agents, oxalic acid and ammonia, were added. Copper chloride ($CuCl_2$) was added in varying proportions to $InCl_3$ and CS $(NH_2)_2$ to make copper-doped indium sulfide. The next solution was kept into a Teflon-lined autoclave, sealed, and kept at 120 C for 5 h. To create nanoparticles, the sample was dried in a hot air oven at 80 ℃ for 5 h, followed by 1 h in a muffle furnace at 300 ℃. The autoclave was allowed to cool naturally to room temperature. The precipitate was centrifuged for separation, rinsed the precipitate with ethanol and distilled water in many times.

2.3. Characterization procedure

Using an X-ray diffractometer, the crystal size of copper-doped indium sulfide nano samples was determined to describe photoluminescence spectra obtained using a spectrophotometer excited between 400 and 800 nm. The morphology was observed with FE-SEM, and UV-DRS measurements in the 220–1400 nm range were performed with a diffuse reflectance spectrometer. X-ray photo electron spectroscopy (XPS), cyclic voltammetry (CV), galvanostatic charge—discharge (GCD), and electrochemical impedance (EIS) were used.

3. Result and discussion

3.1. Structural analysis (XRD)

XRD is used to analyze the crystalline structure of pure indium sulfide and copper-doped indium sulfide. **Figure 1a** shows pure indium sulfide, while **Figure 1b–d** show various amounts of copper-doped indium sulfide nanoparticles.

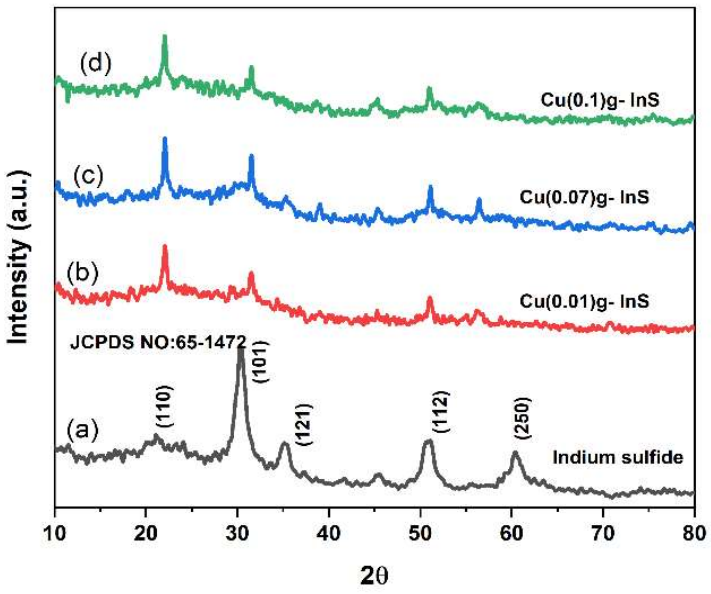

Figure 1. XRD pattern of synthesized. **(a)** Indium sulfide; **(b)** Cu (0.01) g; **(c)** Cu (0.07) g; **(d)** Cu (0.1) g doped Indium sulfide NPs.

According to the XRD pattern, the synthesized nanoparticles are polycrystalline and have an orthorhombic structure, which is consistent with the theoretical expectations (JCPDS No; 65–1472). The XRD pattern of copper-doped indium sulfide nanoparticles are remarkably identical to that of undoped indium sulfide nanoparticles since new phases were found and there was no structural change. The addition of (0.01) g of copper enhanced the peak intensity greatly in the XRD pattern of synthesized copper-doped indium sulfide. This could be attributed to an increase in the size of the crystalline structure [18,19].

The average size of a Crystallite could be calculated using the Debye—Scherer formula [20,21].

$$D = \frac{k\lambda}{\beta \cos\theta}$$

The calculated values, where D, and k denote the crystallite size, incident radiation wavelength, geometrical factor (0.9), measured angle, and FWHM, respectively.

When the copper concentration was increased to 0.1 g, the crystallite sizes grew, and the lattice parameter of the generated nanoparticles was calculated using the following expression:

$$\frac{1}{d^2} = \frac{h^2}{a^2} + \frac{k^2}{b^2} + \frac{l^2}{c^2}$$

Interplanar spacing and miller indices are represented by d and h, k, l, respectively. Doping occurs proved by the comparative study of radius of Cu^{2+} (0.73 Å) is less than that of In^{3+} (0.80 Å). The dislocation density and micro strain of copper-doped indium sulfide nanoparticles were calculated using the following equations [22–24].

$$\delta = \frac{1}{D^2}$$

$$\varepsilon = \beta \cos \theta/4$$

The dislocation density and micro strain of copper-doped indium sulfide nanoparticles were determined using the equations are in the **Table 1**.

Table 1. Structural parameters of pure InS and Cu-doped InS nanoparticles.

Samples	Average Crystallite Size (nm)	Dislocation Density (δ) (X 1015 M-2)	MicroStrain (ε) X 10-3	Lattice Parameters (Å)		
				A	B	C
Indium Sulfide	10	3.73	5.56	4.442	10.64	3.939
Cu(0.01)g doped Ins	14	3.54	5.10	3.939	4.442	10.50
Cu(0.07)g doped Ins	17	2.82	3.46	3.939	4.442	10.50
Cu(0.1)g doped Ins	20	2.37	2.50	3.939	4.442	10.50

3.2. Spectral analysis (FTIR)

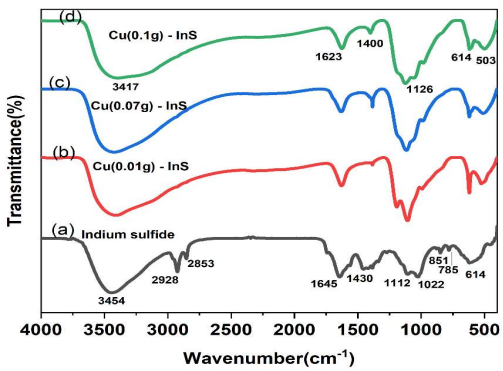

Figure 2. FTIR spectra of synthesized. **(a)** Indium sulfide; **(b–d)** Cu (0.01, 0.07, 0.1) g doped InS NPs.

The FTIR spectrum was shown in **Figure 2** to help comprehend the synthesis of indium sulfide nanoparticles and the numerous functional groups found in the samples. The **Figure 2** depicts an analysis of the FTIR spectrum from 4000 to 400 cm^{-1} [25]. The optical band gap, surface form, and crystallite structure all have an effect on band locations and presence of the number of absorption peaks.

It is also in responsible of determining the material's elemental makeup. Broad absorption bands in all samples, with wavelengths ranging from 3550 to 3200 cm^{-1}, confirmed the presence of the O–H and the hydroxyl group of H_2O molecules from stretching vibration absorbed on the surfaces [26,27]. The existence of absorbed compounds on the surfaces of pure nanocrystals is indicated by absorption peaks in between the range of 3000–2840 cm^{-1}, which correspond to specific symmetric and asymmetric C–H stretching mode groups reduced in the Cu-doped InS spectra. Because of the presence of organic compounds in the samples, absorption bands between 1600 and 1400 cm^{-1} were observed, which correspond to the C = C stretching. The stretching modes of the In-S band may be responsible for the absorption peaks below 1000 cm^{-1}. S band stretching peaks are responsible for the absorption peak at 614 cm^{-1} for pure indium sulfide (0.1) g. The FTIR and XRD patterns demonstrate the efficacy of doping indium sulfide with an impurity-free crystalline substance. Cu doping of 0.01 g, 0.07 g, and 0.1 g improved the In-S, Cu stretching absorption band at 614 cm^{-1} and 503 cm^{-1}. The incorporation of Cu doped-InS lattice structure is shifted at little frequency in absorption band. As a result, these bands absorbed more FTIR wavelengths are extended than undoped InS nanoparticles. Infrared peaks with wavelengths less than 700 cm^{-1} are ideal for analyzing InS bands and functional groupings [28].

3.3. Morphological analysis (FESEM /EDX)

FESEM micrographs of indium sulfide and copper doped indium sulfide nanocrystals (0.01 g, 0.07 g, 0.1 g) were recorded. Indium sulfide has an uneven spherical shape with particle agglomeration, as shown in **Figure 3a–d** depicts the spherical form of evenly distributed nanocrystals. The degree of agglomeration increases with doping concentration, as seen in the graph for copper-doped indium sulfide.

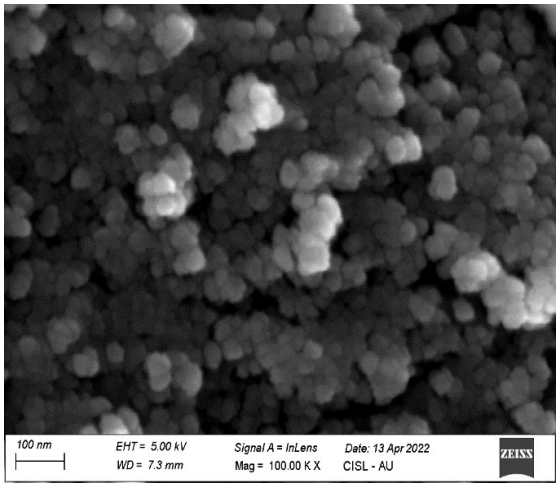

(a)

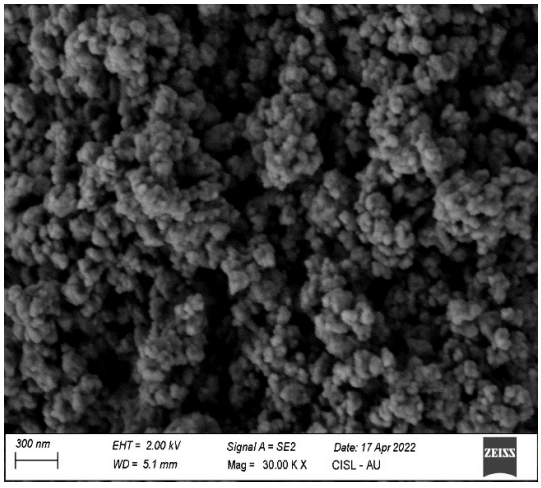

(b)

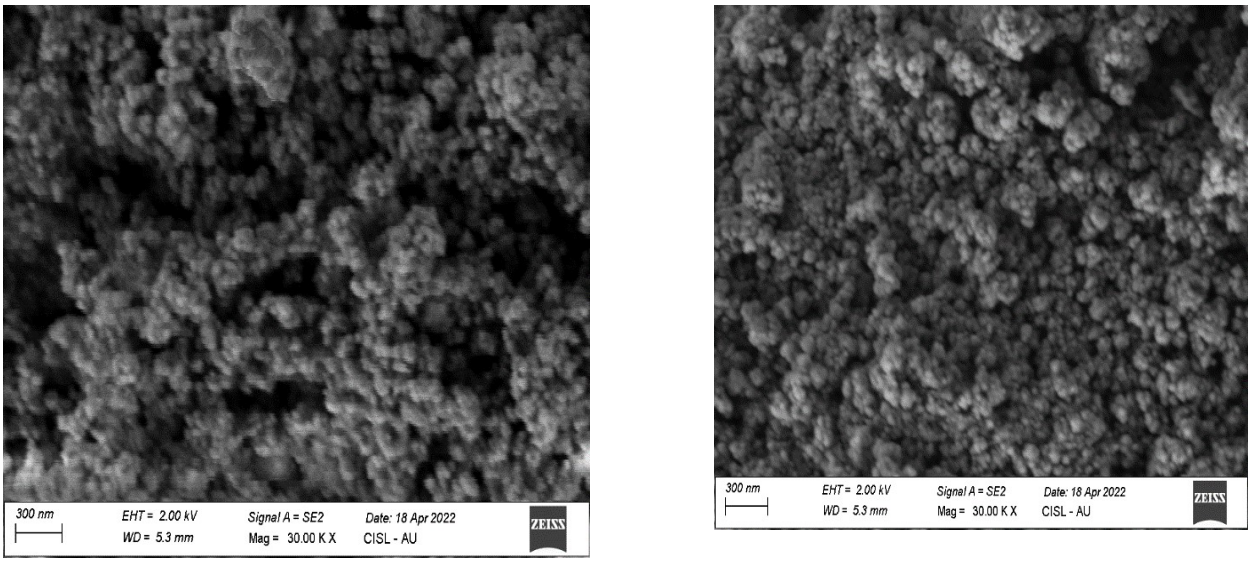

(c) **(d)**

Figure 3. FE-SEM images of **(a)** Indium sulfide; **(b)** Cu (0.01) g; **(c)** Cu (0.07) g; **(d)** Cu (0.1) doped Indium sulfide.

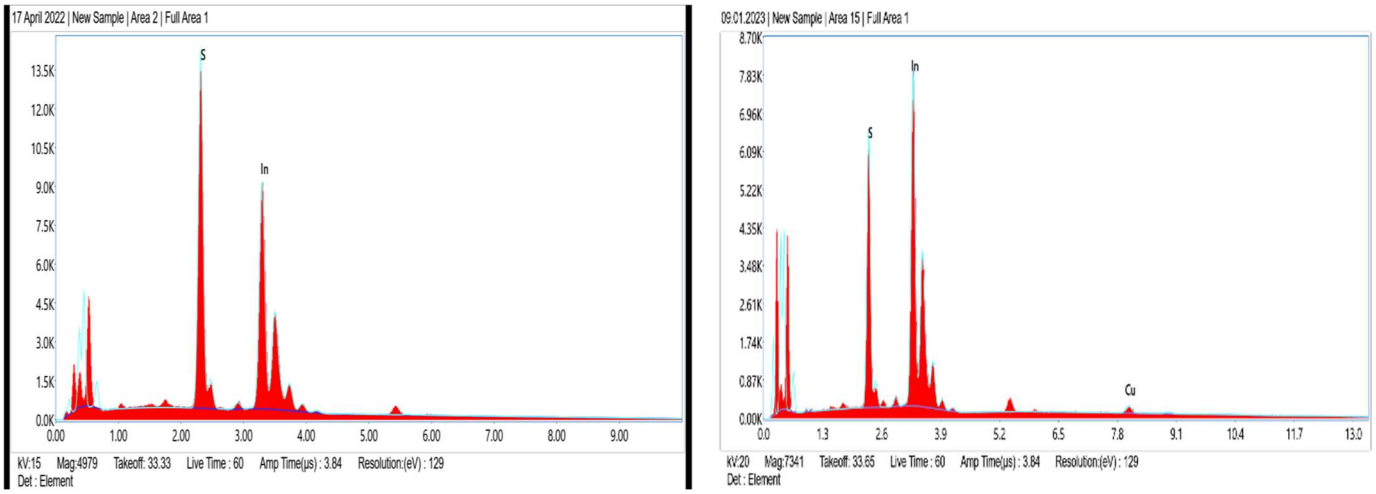

(a) **(b)**

Figure 4. EDX spectrum of pure **(a)** InS; **(b)** Cu-doped InS.

EDX analysis was used to determine the elemental contact of the synthesised samples [28–30]. The existence of In and S is confirmed by the EDX spectra of indium sulfide nanocrystals. **Figure 4a–b**. The presence of copper ions in the EDX spectra of copper-doped indium sulfide indicates that copper was successfully doped in InS. EDX spectra revealed that $CuCl_2$ doped InS had In, S, and Cu atomic percentages of 52.91, 43.17, and 03.93, respectively.

3.4. Optical absorption studies (UV-DRS)

To explore the optical quality, a UV-Visible diffuse reflectance spectra (UV-Vis DRS) investigation was carried out the light absorption capacity of the manufactured items. Reflectance is commonly defined as the ratio of radiant flux reflected to radiant flux incident. In the case of diffuse reflectance, the energy of the reflected radiation has been partially absorbed, transmitted, and scattered by a surface with no set angle

of reflection [31–34]. The UV-Vis DRS findings of pure indium sulfide and copper (0.01 g, 0.07 g, 0.1 g) doped indium sulfide nanocrystals recorded at 220 nm–1200 nm wavelength range are depicted in **Figure 5a–d.**

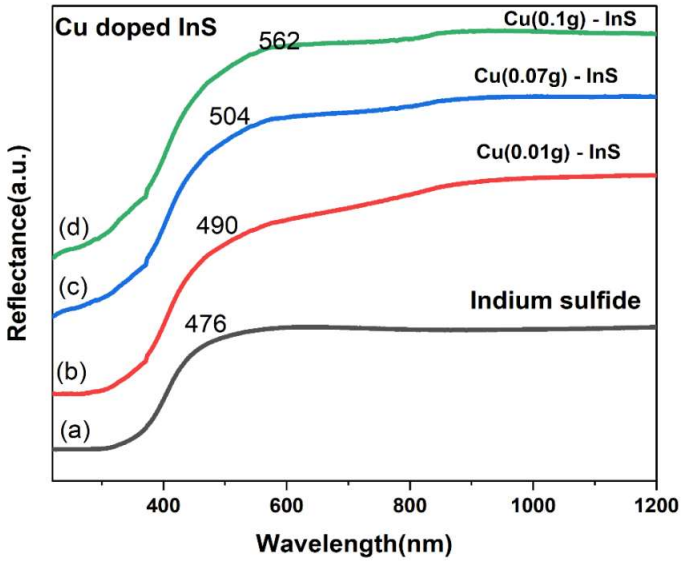

Figure 5. UV-Vis DRS of synthesized **(a)** Indium sulfide; **(b)** Cu (0.01) g; **(c)** Cu (0.07) g; **(d)** Cu (0.1) doped InS.

As shown in **Figure 5a–d** all the samples had optical activity in the UV range, with total reflectance ranging from 450 to 600 nm. The Kubelka—Munk function [35] can be used to calculate Eg.

$$[F(R)\,h]\,n = A\,(h - Eg),\ F(R) = (1-R)^2/2R)$$

where $F(R)$ is the Kubelka-Munk function for assistance and R is the reflectance of the sample.

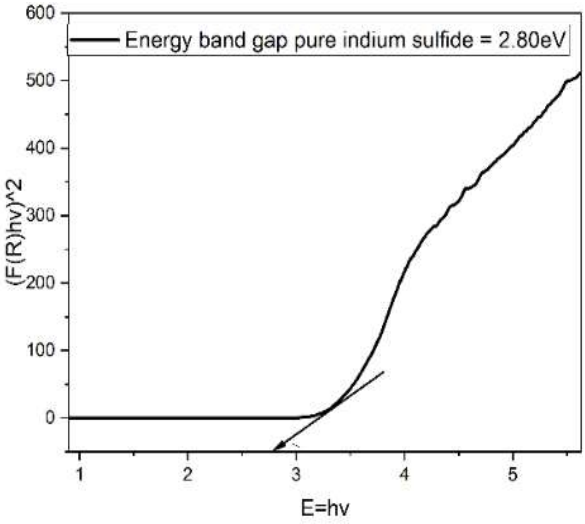

(a)

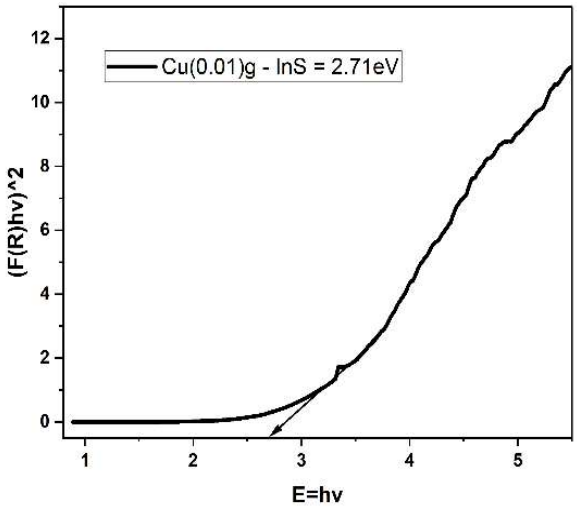

(b)

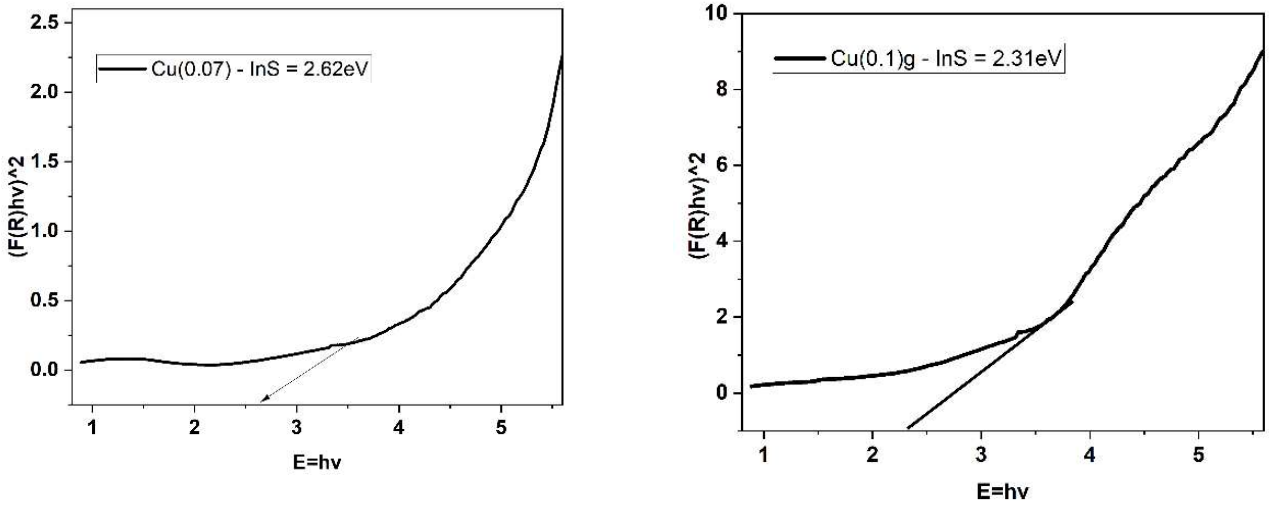

(c) **(d)**

Figure 6. Optical band gap spectra of **(a)** Indium sulfide; **(b)** Cu (0.01) g; **(c)** Cu (0.07) g; **(d)** Cu (0.1) doped InS NPs.

Extrapolating the linear component of the $(F(R)\ \mathrm{hv})^2$ curve versus the photo energy hv yields the optical band gap Eg. **Figure 6a–d** The figure shows that undoped indium sulfide has a band gap of 2.80 eV, whereas copper doped indium sulfide has estimated band gaps of 2.71 eV, 2.62 eV, and 2.31 eV. Doping indium sulfide with a low concentration of Cu (0.01) g resulted in a decrease in band gap due to a decrease in carrier concentration. Yet, as the concentration of copper (0.07 g and 0.1 g) increases, the value of the band gap falls. The band gap of nanocrystals appears to vary somewhat with doping concentration. This slight movement may be the result of a considerable surge in free-of-charge carriers. About copper ion doping and the subsequent shift of the Fermi level below the band edge. The mechanism for reducing the band gap is described below.

In terms of unstrained E_g, the band gap of a stressed E_g can be defined as

$$E_g = E_c - E_v = -E_v = -(E_g^0 + \Delta E_v)$$

With reference the band gap position in stressed E_g can be expressed unstrained E_g, unstressed position, the E_v is change in valance band the position gives stresses, the negative E_v value represents decrease of band gap. the positive E_v value represents increase of band gap. The band gap stressed versus unstressed position there is change in strained and unstrained E_g.

Doping can generate the energy required to accommodate extended electrons by substituting copper ions for indium sites. These energy levels shrank, resulting in impurity-induced bands derived mostly from interactions between the Cu 2p and In 3d states. The impurity-of dopant induced bands now mix with the conductance band, narrowing the band gap [36–38].

3.5. Photoluminescence studies

The graphic displays the PL emission characteristics are recorded at a wavelength of 465 nm. The spectra (**Figure 7**) revealed the presence of two visible emission features at 465 and 528 nm. The appearance of an intense green peak at 528 nm and a

faint emission at 465 nm is due to intense intrinsic defects such as indium interstitials and vacancies.

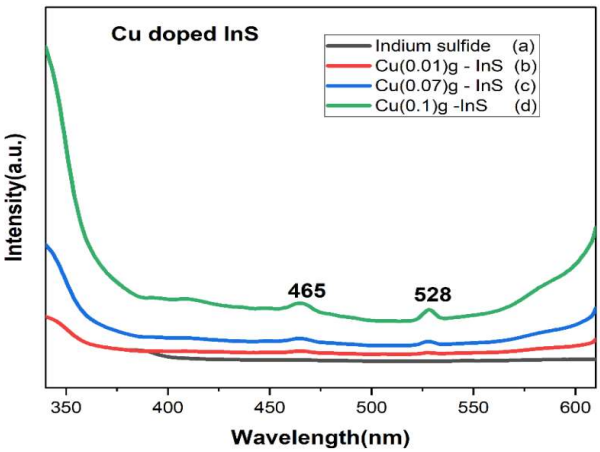

Figure 7. Photoluminescence spectra of synthesized **(a)** Indium sulfide; **(b)** Cu (0.01) g; **(c)** Cu (0.07) g; **(d)** Cu (0.1) doped InS NPs.

The presence of an emission band at 528 nm is caused by sulfur interstitials and lattice vacancies. Copper doping optimises the sulfur emission behaviour of indium sulfide. Doping can typically generate crystal structural strain in the host material. The strain produced may change the lattice's band length and band angle, resulting in the creation of numerous defect sites within the crystal structure. The visual emission intensity of all doped products is reduced when compared to indium sulfide that has not been doped for two reasons. One possibility is that the inherent weaknesses have been reduced. Despite the fact that doping increases the number of defect sites, the charge carriers can be kept from recombining in the defect sides. Copper (0.1 g) doped indium sulfide emits the most light, demonstrating its suitability for photocatalytic applications [39–41]. Furthermore, doping moves the red and blue emission peaks, while the green emission shifts substantially. These variations may be related to the differing depth levels of the problematic locations.

3.6. X-Ray photoelectron spectral analysis

The chemical composition determination and binding energy state of copper-doped indium sulfide are investigated using XPS. The graphic **Figure 8** illustrates the sample's intensity versus binding energy curves. The peaks obtained show the percentage of core-level electrons without collide at their initial energy level.

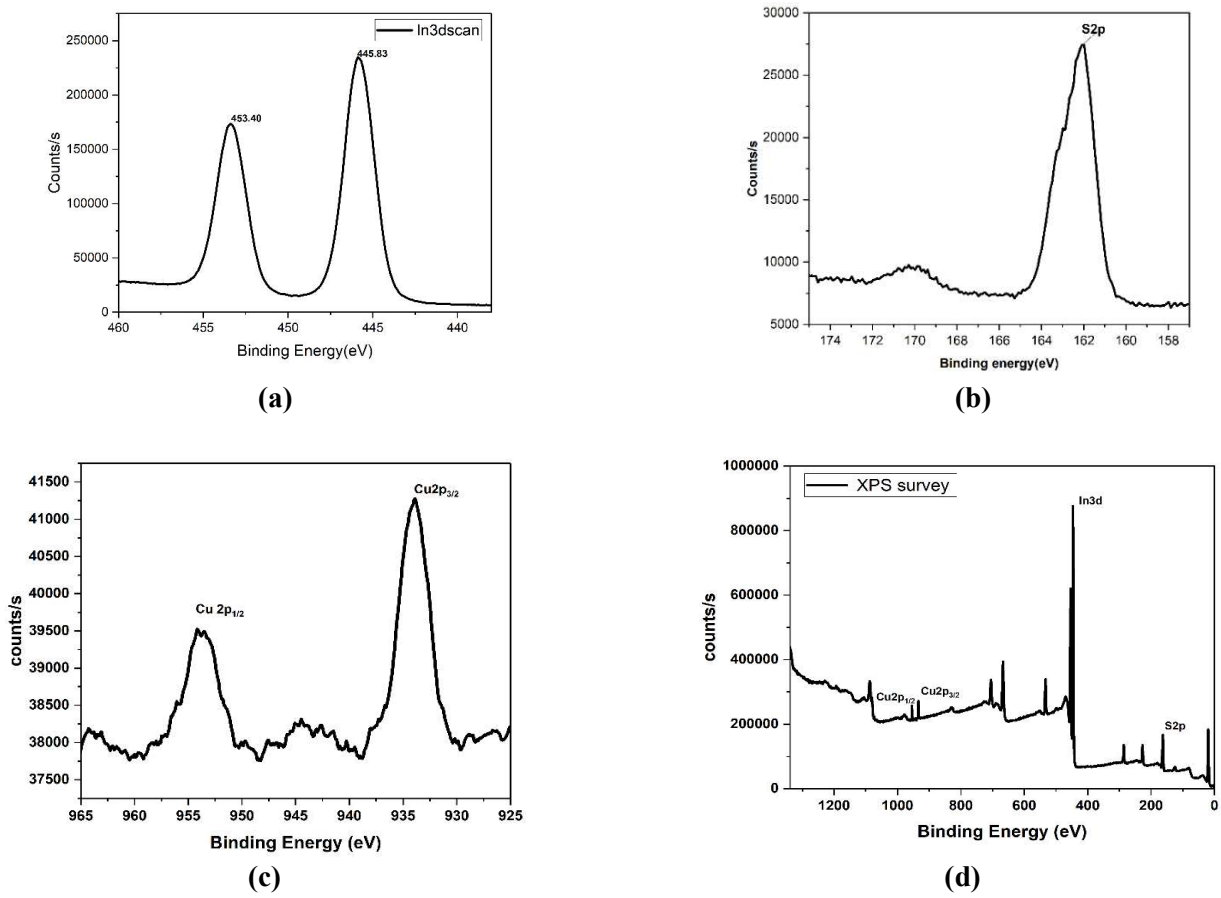

Figure 8. (a) In 3d; **(b)** S 2p; **(c)** Cu 2p binding energy spectrum of CuInS NPs; **(d)** XPS survey spectrum.

For core-level signals, the XPS notation is Xn_j^l, where X is the element, n is the principal quantum number (n = 1, 2, 3), and l is the angular momentum quantum number designated as s, p, and f for l = 0, 1, 2, 3... (n − 1). The quantum number of total angular momentum is represented by the letter j (j = l + s). The In 3d spectrum displays two significant peaks at 445.83 and 453.40 eV with a spin orbital splitting of 7.57 eV. These peaks match the binding energies of In $3d_{5/2}$ and In $3d_{3/2}$ perfectly, suggesting that In is present as In^{3+}. The S 2p and XPS areas of copper-doped indium sulfide are depicted in the figure. Because of the combination of sulfur ions and indium sulfide ions, the S 2p peaks are split into two at 162 eV and 170.55 eV. The Cu $2p_{3/2}$, Cu $2p_{1/2}$ spin orbital splitting of 19.93 eV suggests that copper ions in copper doped indium sulfide could have a valence of +2. As a result of the XPS results, Cu^{2+} ions are successfully doped into indium sulfide lattices [42].

3.7. Photocatalytic studies

100 mL of a 0.03 mg/L methylene blue aqueous solution was mixed with 0.3 g of indium sulfide catalyst to compare the photocatalytic activity of indium sulfide and copper-doped indium sulfide against methylene blue. The sun was used as an irradiation source [43].

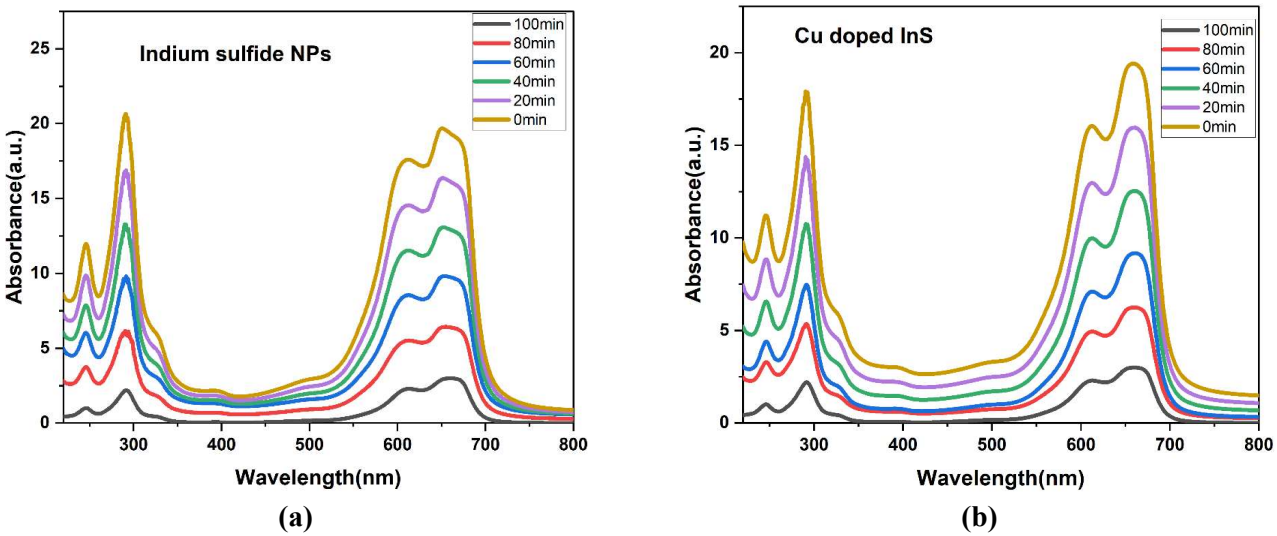

Figure 9. Absorption spectra of the MB solution presence of catalyst **(a)** InS; **(b)** Cu (0.1 g)—doped InS.

During light irradiation, 5 mL of material was examined using a UV-Vis spectrophotometer at P_{max} = 660 nm, and photodegradation was calculated using an equation.

$$X = (C_0 - C_t/C_0 \times 100\%)$$

C_0 = denotes the initial colourant concentration.

C_t = dye concentration after irradiation within the specified time span

The electron-hole pair in reactive nature determines the photocatalytic activity of semiconductor nanoparticles. When exposed to light with a higher energy than the semiconductor's band gap reduce, one electron is excited to the conduction band, and another electron in the conduction band migrates to the lattice surface. The **Figure 9a–b** exhibit changes in the absorption pattern of methylene blue when exposed to sunlight for varied durations of time in the presence of indium sulfide and copper-doped indium sulfide.

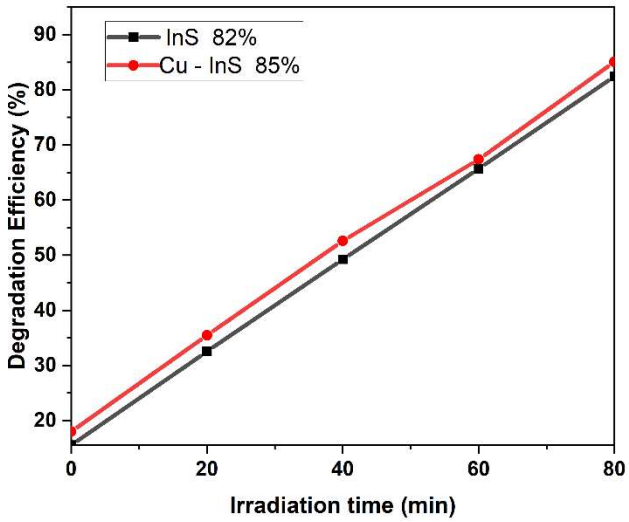

Figure 10. Percentage of photocatalytic degradation curves for different photocatalysts.

After 100 min of light irradiation, it is clear that indium sulfide destroyed 82% of the dye but not copper-doped indium sulfide. The degradation rate soared to 85 percent after 100 min of light exposure. This study (**Figure 10**) found that copper-doped indium sulfide has higher photocatalytic activity than pure indium sulfide. The rate constant values were calculated by using first order equation.in dye degradation reactions [44].

$$\ln (C_0/C) = kt$$

where k represents the first order rate constant, t is the time, and C and C_0 are the dye concentrations before and after degradation.

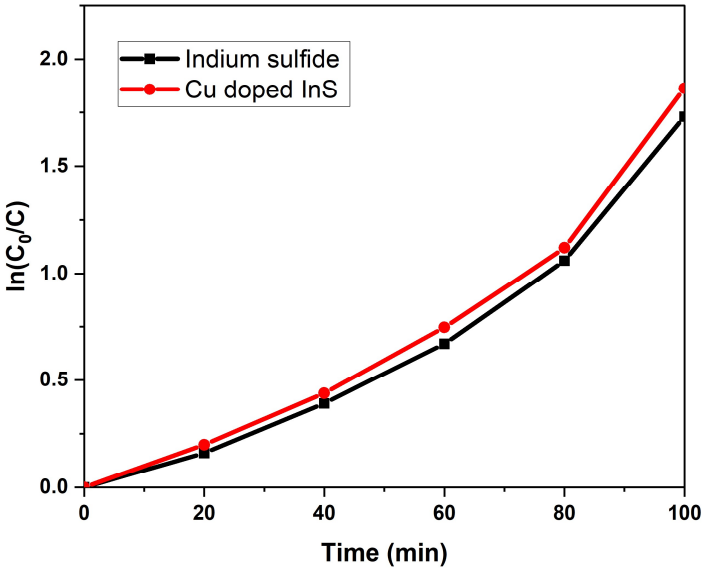

Figure 11. Pseudo-first-order reaction kinetic linear relationship curves for different photocatalysts.

For all samples, the **Figure 11** indicates a linear connection between ln C_0/C and time, and rate constant values were computed based on the slope of the graph [45,46]. The rate constant of undoped indium sulfide was found to be on the order of 1.73051 min^{-1}, whereas the enhanced k value (1.863 min^{-1}) shows an increase in photocatalytic activity for copper-doped indium sulfide.

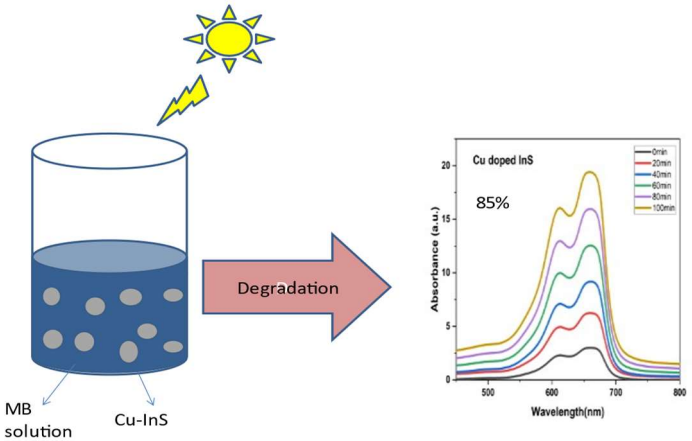

Figure 12. Photocatalytic mechanism of Cu (0.1g)-doped InS NPs.

The potential mechanism underlying the improved the photocatalytic activity of copper-doped indium sulfide is explained below **Figure12**.

When electrons from the valence band are exposed to light with an energy greater than the forbidden gap, they can make a quantum leap to the conduction band. Dopant Cu^{2+} can occupy photogenerated electrons or holes, which are then transported to adsorbed oxygen, hydroxyl ions to produce super oxide radicals (O^{2-}) and hydroxide radicals (OH^{-}) [47]. This action inhibits electron-hole pair recombination and promotes the formation of free radicals, which are responsible for the breakdown of methylene blue. In this way, copper-doped indium sulfide exhibits enhanced activity in the breakdown of methylene blue dye.

3.8. Electrochemical studies (CV)

In 2 M aqueous KOH electrolytes, CV, GCD, and EIS measurements were performed on indium sulfide and copper-doped indium sulfide. The picture depicts CV curves of pure indium sulfide and copper doped indium sulfide electrodes at scan speeds of 5, 10, 15, 20, and 25 mV/s getting across the range of −0.0 eV to 0.4 eV.

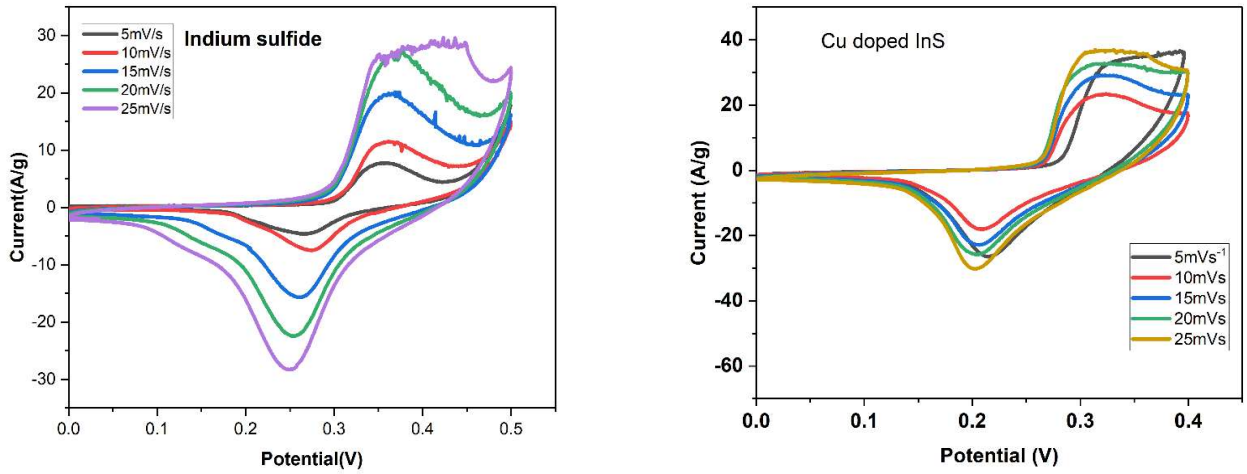

(a) **(b)**

Figure 13. (a) CV curve of Pure Indium sulfide; **(b)** CV curve of pure InS and Cu (0.1)g doped indium sulfide.

The CV curves of pure indium sulfide and copper-doped indium sulfide electrodes are roughly rectangular in shape and overlaid with a broad faradic curve spanning 0.00 to 0.35 eV. This **Figure 13** indicates that in pure indium sulfide and copper-doped indium sulfide electrodes, electrical double layer and faradic pseudo capacitance coexist. Furthermore, the *CV* curves behave similarly to the zero current line, revealed at each potential limit with a rapid current response to voltage.

$$C_{sp} = \frac{A}{k\Delta vm}$$

C_{sp}—Specific capacitance
A—Area of the quasi rectangular
K—Scan rate
M—mass of the active material
Δv—anodic and cathodic changes on each scanning.

Table 2. The specific capacitance of the Cu doped InS nanoparticles at the different scan rates.

S. No.	Scan Rate (mV/s)	Specific Capacitance (Indium sulfide) (F/g)	Specific Capacitance (Cu-InS) (F/g)
1.	5	276	505
2.	10	181	433
3.	15	174	376
4.	20	168	345
5.	25	167	223

The results show that the copper-doped indium sulfide electrode outperforms the pure indium sulfide electrode in supercapacitor rate performance. The CV curves appear quasi-rectangular [48–50].

Curve deviation occurred moderately, as per **Table 2** when the scan rate was increased from 5 to 15 mV/s, but not when the scan rate was consistently increased to 20 and 25 mV/s. This can happen as a result of the electrode's overpotential and polarisation effect.

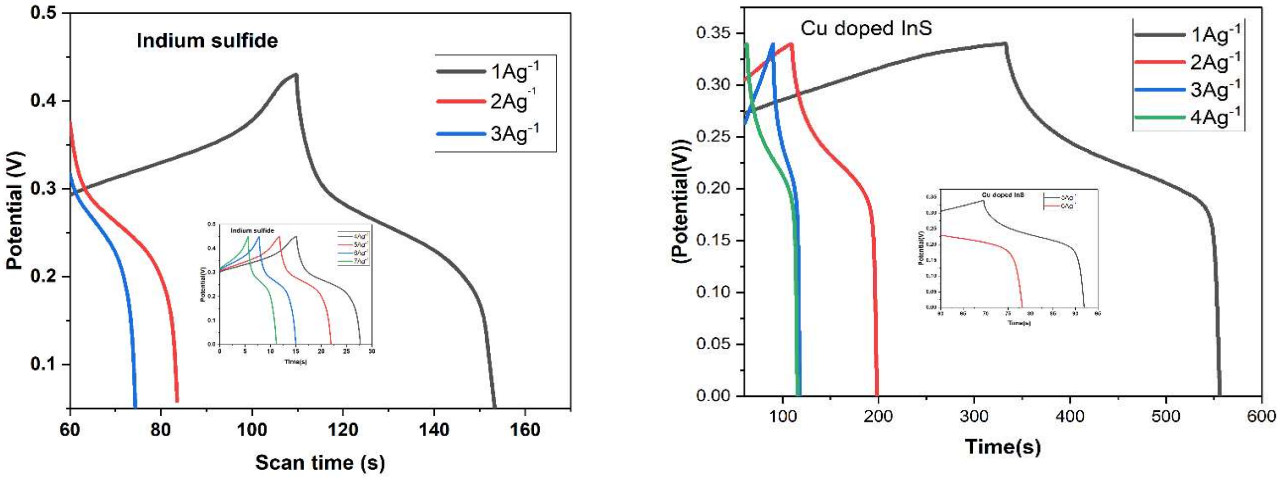

(a) **(b)**

Figure 14. (a) GCD curve of pure InS at different current densities; **(b)** GCD curve of pure InS and Cu (0.1) g doped indium sulfide at different current densities.

The graph (**Figure 14**) shows the galvanostic charging and discharging profiles of a copper-doped indium sulfide electrode with current densities of 1, 2, 3, 4, 5, 6, 7 Ag^{-1} over a potential range of 0.0 to 0.4 V. The *C*s were calculated in accordance with

$$Cs = \frac{i\Delta t}{\Delta vm}$$

Δt—discharge time, i—discharge current, Δv—Potential change during discharge, m-mass of active material.

At 1, 2, 3, 4, 5, and 6 Ag^{-1}, the optimal value of the copper-doped indium sulfide electrode is 639, 505, 450, 394, 384, and 206 Fg^{-1}, respectively. Because of the increase in voltage drop and more or less insufficient use of electro-active material which are involved in the redox process, the Cs steadily declined as the current density grew, the values are presented in **Table 3**.

Table 3. The specific capacitance of the Cu doped InS nanoparticles at different current densities.

S. No.	Current density (mA)	Specific Capacitance (Indium sulfide) (F/g)	Specific Capacitance (Cu-InS) (F/g)
1.	1	300	639
2.	2	210	505
3.	3	167	450
4.	4	163	394
5.	5	156	384
6.	6	127	206
7.	7	124	-

Response as current density increases. The copper doped indium sulfide electrode, on the other hand, exhibits exceptional specific capacitance at all current densities and excellent rate capability because the zero-dimensional nanostructure of copper doped indium sulfide enables rapid transport of electrolyte ions, which is conducive to the development of rate capability in electrodes.

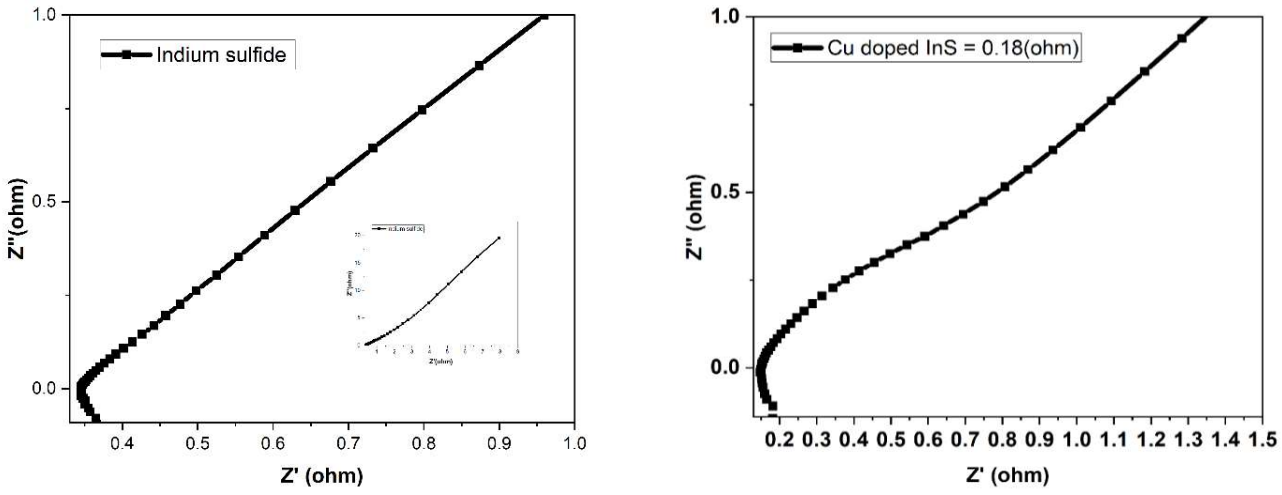

(a) **(b)**

Figure 15. (a) Electrochemical impedance spectra of pure InS; **(b)** Electrochemical impedance spectra of pure InS and Cu (0.1 g) doped InS.

The electrochemical behaviour of a copper-implanted indium sulfide electrode. Using an open circuit potential, electrochemical impedance study was performed in the frequency range of 100 mHz to 100 kHz. The Nyquist curve of the copper-doped indium sulfide electrode is shown in **Figure 15 a–b**. A single semicircle region in the high frequency zone corresponds to the apparent resistance during charge transfer at the solid sulfide electrolyte interface, but a practically straight line in the low frequency zone shows electrolyte ionic diffusion. According to the electrochemical impedance analysis, the copper-doped indium sulfide electrode is suitable for supercapacitor applications [51].

4. Conclusion

The easy hydrothermal procedure provides a simple and efficient method for producing pure indium sulfide and copper-doped indium sulfide nanoparticles (NPs).

Both pure and Cu-doped Indium sulfide nanoparticles (NPs) were polycrystalline with an orthorhombic structure and somewhat displaced due to an increase in volume with increasing Cu doping concentration, according to XRD data. Cu-doped InS nanoparticles had an orthorhombic BCC form with a particle size range of 14 to 20 nm. The band gap energy level of the manufactured InS nanoparticles with dopant Cu^{2+} is raised due to the quantum confinement effect. In PL data, Cu-doped InS nanoparticles showed increased visible emissions. Photocatalytic tests demonstrated that doped NPs increased the MB dye's photodegradation percentage, suggesting a unique way to treating water contamination and environmental pollution. The Cu-doped InS electrode outperformed pure indium sulfide in electrochemical performance, with a maximum specific capacitance of 639 Fg^{-1}. According to the findings, the cu-doped indium sulfide nanoparticles produced might be used in MB photocatalytic degradation and electrochemical performance.

Author contributions: Conceptualization, investigation, original draft preparation, reviewing and editing, LMK; supervision, GD and RPS. All authors have read and agreed to the published version of the manuscript.

Conflict of interest: The authors declare no conflict of interest.

References

1. Motaung MP, Onwudiwe DC, Wei L, et al. CuS, In2S3 and CuInS2 nanoparticles by microwave-assisted solvothermal route and their electrochemical studies. Journal of Physics and Chemistry of Solids. 2022; 160: 110319. doi: 10.1016/j.jpcs.2021.110319
2. Soni V, Raizada P, Kumar A, et al. Indium sulfide-based photocatalysts for hydrogen production and water cleaning: a review. Environmental Chemistry Letters. 2021; 19(2): 1065−1095. doi: 10.1007/s10311-020-01148-w
3. Sanchez-Tizapa M, Sosa-Muñiz MC, Flores-Martínez M, et al. Electrical characterization of electrodeposited indium sulfide thin films by electrochemical impedance spectroscopy and electrical force microscopy. Materials Science in Semiconductor Processing. 2020; 120: 105248. doi: 10.1016/j.mssp.2020.105248
4. Sawant JP, Bhujbal PK, et al. Copper Indium Disulfide Thin Films: Electrochemical Deposition and Properties. ES Materials & Manufacturing; 2022. doi: 10.30919/esmm5f629
5. Kennedy A, Ganesan H, Marnadu R, et al. An effect of metal ions (Cu, Mn) doping on the structural, morphological, optical, photoluminescence, electrical and photocatalytic properties of In2S3 nanoparticles. Optical Materials. 2022; 124: 111769. doi: 10.1016/j.optmat.2021.111769
6. Vakalopoulou E, Rath T, Warchomicka FG, et al. Honeycomb-structured copper indium sulfide thin films obtainedviaa nanosphere colloidal lithography method. Materials Advances. 2022; 3(6): 2884-2895. doi: 10.1039/d2ma00004k
7. Suthakaran S, Dhanapandian S, Krishnakumar N, et al. Surfactants assisted SnO2 nanoparticles synthesized by a hydrothermal approach and potential applications in water purification and energy conversion. Journal of Materials Science: Materials in Electronics. 2019; 30(14): 13174−13190. doi: 10.1007/s10854-019-01681-7
8. Yan D, Lim YV, Wang G, et al. Unlocking Rapid and Robust Sodium Storage Performance of Zinc-Based Sulfide via Indium Incorporation. ACS Nano. 2021; 15(5): 8507-8516. doi: 10.1021/acsnano.1c00131
9. Farzi M, Moradi M, Hajati S, et al. Synthesis of rod-like ternary Cu(Cd)-In-S and quaternary Cu-Cd-In-S by controlled ion exchange of MIL-68(In) derived indium sulfide for high energy-storage capacitor. Synthetic Metals. 2021; 278: 116815. doi: 10.1016/j.synthmet.2021.116815
10. Kennedy A, Ganesan H, Govindaraj T, et al. Effect of Metal (Cu, Mn) Doping on the Structural, Morphological, Optical, Photoluminescence, Electrical and Photocatalytic Properties of In2s3 Nanoparticles. https://doi.org/10.21203/rs.3.rs-588347/v1.
11. Ethiraj AS, Uttam P, KV, et al. Photocatalytic performance of a novel semiconductor nanocatalyst: Copper doped nickel oxide for phenol degradation. Materials Chemistry and Physics. 2020; 242: 122520. doi:

10.1016/j.matchemphys.2019.122520
12. Chen YX, Li F, Wang W, et al. Optimization of thermoelectric properties achieved in Cu doped β-In2S3 bulks. Journal of Alloys and Compounds. 2019; 782: 641-647. doi: 10.1016/j.jallcom.2018.12.138
13. Jiao M, Huang X, Ma L, et al. Biocompatible off-stoichiometric copper indium sulfide quantum dots with tunable near-infrared emission via aqueous based synthesis. Chemical Communications. 2019; 55(100): 15053−15056. doi: 10.1039/c9cc07674c
14. Higashimoto S, Nakase T, Mukai S, et al. Copper-indium-sulfide colloids on quantum dot sensitized TiO2 solar cell: Effects of capping with mercapto-acid linker molecules. Journal of Colloid and Interface Science. 2019; 535: 176−181. doi: 10.1016/j.jcis.2018.09.092
15. Kumar S, Yadav N, Kumar P, et al. Design and Comparative Studies of Z-Scheme and Type II Based Heterostructures of NaNbO3/CuInS2/In2S3 for Efficient Photoelectrochemical Applications. Inorganic Chemistry. 2018; 57(24): 15112−15122. doi: 10.1021/acs.inorgchem.8b02264
16. Mousavi-Kamazani M. A green and simple hydrothermal approach to synthesize needle-like CuInS2 nanostructures for solar cells. Journal of Materials Science: Materials in Electronics. 2018; 29(18): 16050−16056. doi: 10.1007/s10854-018-9693-9
17. Sharma RK, Chouryal YN, Nigam S, et al. Tuning the Crystal Phase and Morphology of the Photoluminescent Indium Sulphide Nanocrystals and Their Adsorption-Based Catalytic and Photocatalytic Applications. ChemistrySelect. 2018; 3(28): 8171-8182. doi: 10.1002/slct.201801006
18. Aydin E, Demirci Sankir N. AZO/metal/AZO transparent conductive oxide thin films for spray pyrolyzed copper indium sulfide based solar cells. Thin Solid Films. 2018; 653: 29-36. doi: 10.1016/j.tsf.2018.03.012
19. Bi K, Sui N, Wang Y, et al. Temperature-dependent charge carrier dynamics investigation of heterostructured Cu2S-In2S3 nanocrystals films using injected charge extraction by linearly increasing voltage. Applied Physics Letters. 2017; 110(8). doi: 10.1063/1.4977000
20. Silambarasan M, Ramesh PS, Geetha D, et al. A report on 1D MgCo2O4 with enhanced structural, morphological and electrochemical properties. Journal of Materials Science: Materials in Electronics. 2017; 28(9): 6880-6888. doi: 10.1007/s10854-017-6388-6
21. Li M, Zhao R, Su Y, et al. Synthesis of CuInS2 nanowire arrays via solution transformation of Cu2S self-template for enhanced photoelectrochemical performance. Applied Catalysis B: Environmental. 2017; 203: 715-724. doi: 10.1016/j.apcatb.2016.10.051
22. Frank A, Wochnik AS, Bein T, et al. A biomolecule-assisted, cost-efficient route for growing tunable CuInS2 films for green energy application. RSC Advances. 2017; 7(33): 20219-20230. doi: 10.1039/c6ra27294k
23. Esmaili P, Kangarlou H, Savaloni H, et al. Structural, optical and electronic properties of indium sulfide compositions under influence of copper impurity produced by chemical method. Results in Physics. 2017; 7: 3380-3389. doi: 10.1016/j.rinp.2017.08.062
24. Zhao Y, Luo F, Zhuang M, et al. Synthesis of nanostructured CuInS2 thin films and their application in dye-sensitized solar cells. Applied Physics A. 2016; 122(3). doi: 10.1007/s00339-016-9718-2
25. Zhao X, Huang Y, Corrigan JF. Facile Preparation of Wurtzite CuInE2 (E = S, Se) Nanoparticles Under Solvothermal Conditions. Inorganic Chemistry. 2016; 55(20): 10810−10817. doi: 10.1021/acs.inorgchem.6b02177
26. Yang W, Oh Y, Kim J, et al. Photoelectrochemical Properties of Vertically Aligned CuInS2 Nanorod Arrays Prepared via Template-Assisted Growth and Transfer. ACS Applied Materials & Interfaces. 2015; 8(1): 425-431. doi: 10.1021/acsami.5b09241
27. Tamil Illakkiya J, Usha Rajalakshmi P, Oommen R. Enhanced optoelectronic and photoelectrochemical characteristics of nebulised spray pyrolysed 'Cu' rich CuInS2 thin film. Materials Science in Semiconductor Processing. 2016; 49: 84-91. doi: 10.1016/j.mssp.2016.03.027
28. Leach ADP, Macdonald JE. Optoelectronic Properties of CuInS2 Nanocrystals and Their Origin. The Journal of Physical Chemistry Letters. 2016; 7(3): 572-583. doi: 10.1021/acs.jpclett.5b02211
29. Dunst S, Rath T, Reichmann A, et al. A comparison of copper indium sulfide-polymer nanocomposite solar cells in inverted and regular device architecture. Synthetic Metals. 2016; 222: 115−123. doi: 10.1016/j.synthmet.2016.04.003
30. Chen Y, Qin Z, Guo X, et al. One-step hydrothermal synthesis of (CuIn)0.2Zn1.6S2 hollow sub-microspheres for efficient visible-light-driven photocatalytic hydrogen generation. International Journal of Hydrogen Energy. 2016; 41(3): 1524−1534. doi: 10.1016/j.ijhydene.2015.11.087

31. Zheng Z, Yu J, Cheng S, et al. Investigation of structural, optical and electrical properties of Cu doped β-In2S3 thin films. Journal of Materials Science: Materials in Electronics. 2016; 27(6): 5810-5817. doi: 10.1007/s10854-016-4496-3
32. Rajendar V, Dayakar T, Satish B, et al. Synthesis and Characterization of Cuins2 Nanoparticles as Potential Candidates for Photocatalyst and Photovoltaic Materials Synthesis and Characterization of CuInS2 Nanoparticles as Potential Candidates for Photocatalyst and Photovoltaic Materials. Chalcogenide Letters. 2016; 13(10).
33. Mahanthappa M, Yellappa S, Kottam N, et al. Sensitive determination of caffeine by copper sulphide nanoparticles modified carbon paste electrode. Sensors and Actuators A: Physical. 2016; 248: 104−113. doi: 10.1016/j.sna.2016.07.013
34. Krishnakanth R, Jayakumar G, Albert Irudayaraj A, et al. Structural and Magnetic Properties of NiO and Fe-doped NiO Nanoparticles Synthesized by Chemical Co-precipitation Method. Materials Today: Proceedings. 2016; 3(6): 1370−1377. doi: 10.1016/j.matpr.2016.04.017
35. Baneto M, Enesca A, Mihoreanu C, et al. Effects of the growth temperature on the properties of spray deposited CuInS2 thin films for photovoltaic applications. Ceramics International. 2015; 41(3): 4742-4749. doi: 10.1016/j.ceramint.2014.12.023
36. Shanmugam N, Suthakaran S, Kannadasan N, et al. Synthesis and Characterization of Te Doped ZnO Nanosheets for Photocatalytic Application. Journal of Heterocyclics. 2015: 15-20. doi: 10.33805/2639-6734.105
37. Jrad A, Ben Nasr T, Turki-Kamoun N. Study of structural, optical and photoluminescence properties of indium-doped zinc sulfide thin films for optoelectronic applications. Optical Materials. 2015; 50: 128−133. doi: 10.1016/j.optmat.2015.10.011
38. Xue B, Xu F, Wang B, et al. Shape-controlled synthesis of β-In2S3nanocrystals and their lithium storage properties. CrystEngComm. 2016; 18(2): 250-256. doi: 10.1039/c5ce01955a
39. Gannouni M, Assaker IB, Chtourou R. Experimental investigation of the effect of indium content on the CuIn5S8 electrodes using electrochemical impedance spectroscopy. Materials Research Bulletin. 2015; 61: 519-527. doi: 10.1016/j.materresbull.2014.10.070
40. Xie BB, Hu BB, Jiang LF, et al. The phase transformation of CuInS2 from chalcopyrite to wurtzite. Nanoscale Research Letters. 2015; 10(1). doi: 10.1186/s11671-015-0800-z
41. Paquin F, Rivnay J, Salleo A, et al. Multi-phase microstructures drive exciton dissociation in neat semicrystalline polymeric semiconductors. Journal of Materials Chemistry C. 2015; 3(41): 10715−10722. doi: 10.1039/c5tc02043c
42. Park JC, Nam YS. Controlling surface defects of non-stoichiometric copper-indium-sulfide quantum dots. Journal of Colloid and Interface Science. 2015; 460: 173−180. doi: 10.1016/j.jcis.2015.08.037
43. Dhanya AC, Preetha KC, Deepa K, et al. Crystalline Indium Sulphide thin film by photo accelerated deposition technique. IOP Conference Series: Materials Science and Engineering. 2015; 73: 012009. doi: 10.1088/1757-899x/73/1/012009
44. Gao W, Liu W, Leng Y, et al. In2S3 nanomaterial as a broadband spectrum photocatalyst to display significant activity. Applied Catalysis B: Environmental. 2015; 176−177: 83-90. doi: 10.1016/j.apcatb.2015.03.048
45. Yin HY, Tang JH, Yan CJ, et al. Facile Preparation of the Single Crystalline In2S3 Nanosheets with Highly Efficient Photocatalytic Activity. Advanced Materials Research. 2013; 834-836: 8−11. doi: 10.4028/www.scientific.net/amr.834-836.8
46. Lugo-Loredo S, Peña-Méndez Y, Calixto-Rodriguez M, et al. Indium sulfide thin films as window layer in chemically deposited solar cells. Thin Solid Films. 2014; 550: 110−113. doi: 10.1016/j.tsf.2013.10.115
47. Aslan F, Adam G, Stadler P, et al. Sol–gel derived In 2 S 3 buffer layers for inverted organic photovoltaic cells. Solar Energy. 2014; 108: 230-237. doi: 10.1016/j.solener.2014.07.011
48. Shang X, Wang Z, Li M, et al. A numerical simulation study of CuInS2 solar cells. Thin Solid Films. 2014; 550: 649-653. doi: 10.1016/j.tsf.2013.10.047
49. Amiri O, Salavati-Niasari M, Sabet M, et al. Sonochemical Method for Preparation of Copper Indium Sulfide Nanoparticles and their Application for Solar Cell. Combinatorial Chemistry & High Throughput Screening. 2014; 17(2): 183−189. doi: 10.2174/1386207311301010001
50. Yan C, Liu F, Song N, et al. Band alignments of different buffer layers (CdS, Zn(O,S), and In2S3) on Cu2ZnSnS4. Applied Physics Letters. 2014; 104(17). doi: 10.1063/1.4873715
51. Sun J, Chen G, Feng Y, et al. Ag/Cu co-doped ZnS–In2S3solid solutions: facile synthesis, theoretical calculations and enhanced photocatalytic activity. RSC Adv. 2014; 4(84): 44466-44471. doi: 10.1039/c4ra05960c

Energy Storage and Conversion 2024, 2(4), 1815.
https://doi.org/10.59400/esc1815

Article

Effect of graphite powder on thermal behavior of phase change material

Makoto Shibahara[1,*], Yuuhi Hatta[1], Qiusheng Liu[1], Sutopo Purwono Fitri[2]

[1] Graduate School of Maritime Sciences, Kobe University, Kobe 658-0022, Japan
[2] Marine Engineering Department, Sepuluh Nopember Institute of Technology, ITS Campus Sukolilo, Surabaya 60111, Indonesia
*** Corresponding author:** Makoto Shibahara, sibahara@maritime.kobe-u.ac.jp

CITATION

Shibahara M, Hatta Y, Liu Q, Fitri SP. Effect of graphite powder on thermal behavior of phase change material. Energy Storage and Conversion. 2024; 2(4): 1815. https://doi.org/10.59400/esc1815

ARTICLE INFO

Received: 2 October 2024
Accepted: 4 November 2024
Available online: 19 November 2024

Abstract: The effect of graphite powder on the thermal behavior of phase change material (PCM) was investigated experimentally. It is well known that the graphite is contributed to enhance the thermal response. However, the effect of graphite on the supercooling of the PCM is not clear when a highly heat conductive material is added. In this study, the specific heat of the PCM based on sugar alcohol such as D-mannitol and inositol was measured with an adiabatic scanning calorimeter. The enthalpy and entropy during the phase-change process were obtained by the measured specific heat of the PCM. Additionally, the exergy analysis was conducted to evaluate the thermal energy storage of PCM. As the experimental results, the specific heat of D-mannitol during the phase change process was higher than that of inositol. Moreover, it was found that the addition of graphite powder at the mass fraction of 9% improves the thermal behavior of D-mannitol with lower supercooling while maintaining latent heat. The suppression of supercooling by the addition of 9% graphite powder was 37.5%.

Keywords: phase change material; latent heat; thermal response; graphite powder; supercooling

1. Introduction

To address the issues of global warming, the utilization of waste heat has been considered in maritime industries. For effectively utilizing waste heat, the organic Rankine cycle (ORC), which generates power by exhaust heat recovery, is highly attractive. There is a need for heat recovery technologies utilizing the ORC with latent-heat storage materials, and it is important to understand the thermal properties (specific heat, latent heat, etc.) of these materials for the efficient operation of heat recovery systems [1].

Bo et al. [2] investigated the thermal properties of tetradecane, hexadecane, and their binary mixtures using differential scanning calorimetry (DSC). They concluded that binary mixtures are promising candidates for use as phase change materials (PCMs) in cooling systems. Hidaka et al. [3] evaluated the fundamental properties of D-threitol, an optical isomer of erythritol. The results showed that threitol has a heat storage density that is nearly equivalent to ice, with a total heat capacity of 313 kJ/kg in the operating temperature range of 353 to 373 K. It was also revealed that threitol exhibits significant supercooling. Kageyama et al. [4] investigated the relationship between the solidification rate of erythritol and the characteristics of the heat transfer tube surface. They revealed that as the numerical value of the average roughness of the heat transfer tube surface increases, the solidification rate of erythritol decreases, indicating a tendency for thermal conductivity to decrease. Shibahara et al. [5] investigated the thermal characteristics of sodium acetate trihydrate and D-mannitol, using thermogravimetry and differential thermal analysis (TG-DTA). The

experimental result of sodium acetate trihydrate showed that the supercooling of D-mannitol was lower than that of sodium acetate trihydrate. Yan et al. [6] suggested that heterogeneous nucleation could suppress supercooling of hydrate salts [7]. They experimentally investigated the effects of several additives on calcium chloride hexahydrate. When mixing graphite, iron oxide III, potassium chloride (KCl), and strontium chloride hexahydrate ($SrCl_26H_2O$) at 1/3/5 wt.% ratio, they found that strontium chloride hexahydrate at 3 wt.% yielded optimal results. While the latent heat capacity decreases linearly and proportionally with the addition ratio, it does not necessarily follow the same trend in terms of supercooling suppression.

The melting process of D-mannitol was clarified by numerical simulation [8]. They also measured the transient heat-transfer coefficient of D-mannitol under natural convection to develop a heat exchanger for latent-heat storage materials [9]. Mojiri et al. [10] developed the macro-scale thermal energy system using D-mannitol. Karthikeyan et al. [11] carried out the commercial computational fluid dynamics (CFD) analysis to observe the transient melting behavior of D-mannitol. They conducted melting simulations by modeling D-mannitol within stainless steel spheres with diameters of 80 mm and 40 mm and applying heat. The simulation results indicated that the unmelted portions tended to fragment into smaller pieces as the melting of mannitol progressed. These latent heat storage materials, especially those operating in the medium-to-low temperature range, have a critical issue of possessing low thermal conductivity, which significantly impacts the efficiency of waste heat recovery cycles.

In order to overcome the low thermal conductivity of the PCMs, high thermal conductive PCMs have been developed by adding the expanded graphite [12]. Bai et al. [13] measured the temperature of composed PCM with the expanded graphite at the different light intensity. They showed that the thermal response of the PCM improved by adding the expanded graphite of 10% at the irradiation intensity of 0.2 W/m^2. Although there are many studies on the thermal properties of latent heat storage materials, the supercooling is also not discussed when a highly heat conductive graphite powder was added to the PCM. Since the supercooling observed in latent heat storage materials, it is crucial to control supercooling of the PCM.

In this study, the latent heat capacities of latent-heat storage materials were investigated using an adiabatic scanning calorimeter, and experiments related to heat-response characteristics were conducted to improve thermal responsiveness and to suppress supercooling with graphite additions.

2. Material and methods

In this experiment, three types of sugar alcohol with high latent heat and excellent corrosion resistance were investigated: D-mannitol (melting point: 439 K), inositol (498 K), and sorbitol (367 K) [14]. **Figure 1** presents a graph comparing major PCMs and their latent heat capacities [5]. Among various substances, including organic materials and hydrated salts, sugar alcohols exhibit a relatively high latent-heat capacity and possess the distinctive feature of having melting points concentrated in the medium temperature range of 373 K to 573 K. Sugar alcohols also have additional

advantages, including consistent heat absorption and release, high heat-storage capacity per unit volume, chemical stability and low corrosivity, and low cost.

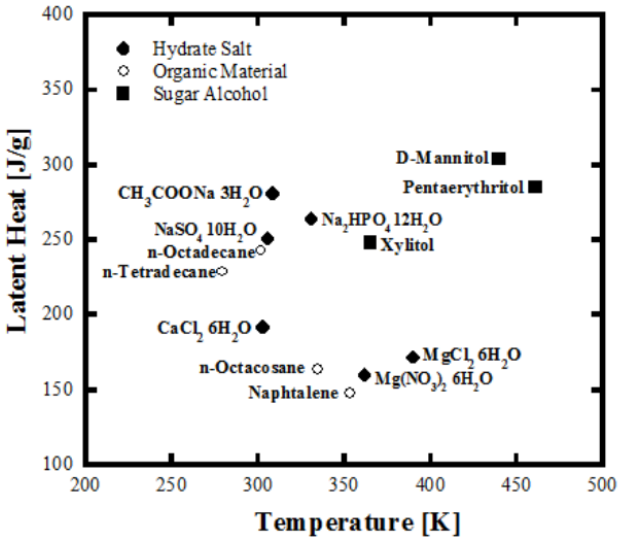

Figure 1. Relationship between the latent heat of PCMs and the melting temperature [5].

Figure 2 shows a schematic representation of the interior of the adiabatic scanning calorimeter (Shinkuuriko, SH-3000-M). The measurement accuracy of specific heat is ±3.0%. Within the chamber, vial containers containing the samples were placed, and the temperature history of the phase transition process was recorded using a data logger while heating, and the temperature increased with an electric furnace. The powdered samples (0.180 g each) were placed in heat-resistant vials. They were then stirred for 30 s using a stirrer. Subsequently, the samples were heated in the furnace of the adiabatic scanning calorimeter at a rate of 0.8 J/s. Heating continued until the samples transitioned from the solid to the liquid phase. The material's temperature was recorded using a data logger. The specific heat of the samples was calculated from the obtained temperature changes and the elapsed time using the following equation:

$$C_p = \frac{Q \cdot \Delta\tau}{M \cdot \Delta T} - \frac{M' C_p'}{M} \quad (1)$$

where, C_p (J/g·K), Q (W), M (g), ΔT (K), $\Delta\tau$ (s), and $M'C_p'$ (J/g·K) represent the specific heat, power, mass, temperature rise, elapsed time, and heat capacity of the vial, respectively.

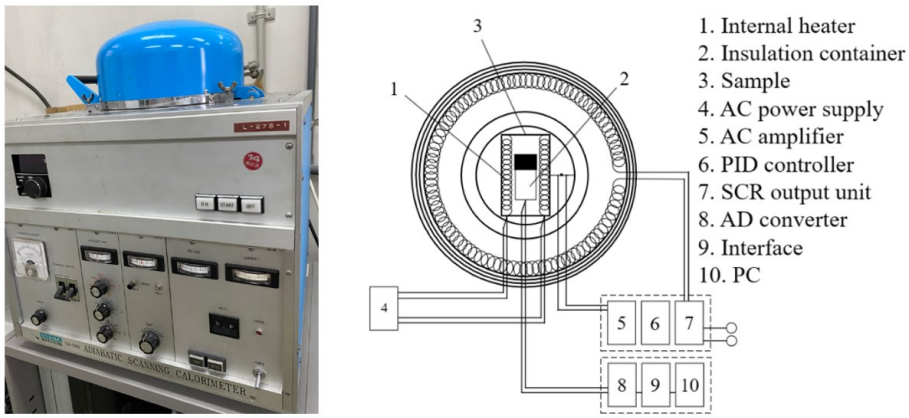

Figure 2. Adiabatic scanning calorimeter.

M'C_p' was determined in advance through a blank test. The latent heat was calculated from the change in enthalpy by using the following equation based on the relationship between the specific heat obtained from Equation (1) and temperature. The difference in enthalpy during the phase transition from solid to liquid was considered as the latent heat:

$$\Delta h = \int_{T_1}^{T_2} C_p \, dT \tag{2}$$

where, Δh (J/g), T_1 (K), and T_2 (K) are the enthalpy change, reference temperature, arbitrary temperature, respectively. Furthermore, the heat stored during the phase transition was determined from Equation (2), and an exergy analysis was conducted using Equation (3) [15].

$$\Delta e = \Delta h - T_0 \Delta s \tag{3}$$

where, Δs was the entropy calculated by Equation (4). T_0 (K) is the ambient temperature, which was set to 293 K in this study.

$$\Delta s = \int_{T_1}^{T_2} \frac{C_p}{T} dT = C_p \ln \frac{T_2}{T_1} \tag{4}$$

where, C_p is the measured specific heat from Equation (1).

In addition to this, we also conducted experiments to improve the thermal responsiveness of latent-heat storage materials. A highly conductive graphite powder was added to mannitol to enhance its thermal responsiveness; this addresses a common challenge in PCMs at moderate to low temperatures. **Figure 3** displays a schematic diagram of the experimental setup. The experimental procedure is as follows:

1) D-mannitol (Fujifilm Wako Pure Chemical Corporation, Osaka, Japan) and graphite powder (AS-One, Osaka, Japan) with average particle sizes ranging from 5 to 11 mm were weighed using a digital scale (A&D HT-120) and mixed for a specified duration using a vortex mixer.

2) A heater was set in a test tube, and the mixture from step (1) was placed inside.

3) The test tube was inserted into a container with rubber stoppers on the top and bottom, sealed, and evacuated to approximately 66 kPa.

4) A thermocouple was inserted to a specified depth.

5) Initial heating was performed once using the heater, and measurements were taken from the second heating cycle after the material had melted and solidified.

The experiments of thermal response were conducted in this sequence. For a total sample mass of 11 g, six samples were prepared by varying the mixing ratio of graphite. The input heating power was adjusted to 50 W, as described in Equation (5).

$$P = VI = V\frac{V_R}{R_s} \tag{5}$$

where, P (W), V (V), I (A), V_R (V), and Rs (Ω) are heat input, voltage of volt slider, electrical current, voltage across the shunt, and shunt resistance, respectively. The temperature of the composite material was measured using a K-type thermocouple inserted into the test tube and recorded by a data logger (GRAPHTEC, GL240). Vacuum insulation was maintained at 66 kPa by a vacuum pump to prevent heat dissipation during measurements.

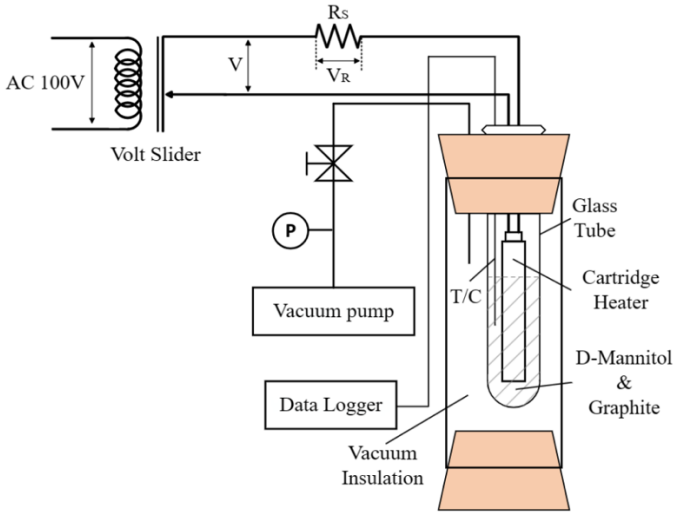

Figure 3. Experimental setup.

The uncertainty of the temperature measured by the thermocouple was estimated as follows [16]:

$$\frac{\Delta T}{T} = \sqrt{\left(\frac{\Delta T_{tc}}{T}\right)^2 + \left(\frac{\Delta T_{cj}}{T}\right)^2} \tag{6}$$

where, the uncertainties of the thermocouple, $\frac{\Delta T_{tc}}{T}$, and the cold junction, $\frac{\Delta T_{cj}}{T}$, respectively. ΔT_{tc} and ΔT_{cj} are ± 0.05% of rdg + 1.0 K and ± 0.5 K, respectively.

3. Results and discussion

3.1. Melting point and specific heat of PCMs

Temperature-time curves for mannitol, inositol, and sorbitol are shown in **Figure 4**. The temperature of all three materials increases with a linear heating process under the solid phase up to 1000 s. Since the melting temperature of sorbitol is about 365.15 K, the temperature gradient of Sorbitol has been changed for the phase change from

solid to liquid state. Similarly, for mannitol and inositol, there is a decrease in the gradient in the temperature—time curve, indicating the onset of the melting point of the material and the start of the phase transition. After the phase transition, the gradient increases again, indicating that the material has completed the phase transition and transitioned into the latent heat (liquid phase) state. **Table 1** compares the melting points obtained in this study with the literature [14]. The measured data are in good agreement with the literature values, indicating a high accuracy of the measurement for each material.

Figures 5–7 show the relationship between the specific heat and temperature for each sample, which were calculated using Equation (1). The specific heat remains constant up to the melting temperature. Subsequently, a significant peak in specific heat appears from the onset of phase transition. It is considered that the increase of specific heat is caused by the latent heat. **Table 2** shows the average specific heat for each sample in phase intervals. It is understood that mannitol is higher average specific heat than that of sorbitol during the phase transition. In the solid phase and liquid phase, the specific heat of mannitol is higher than that of inositol.

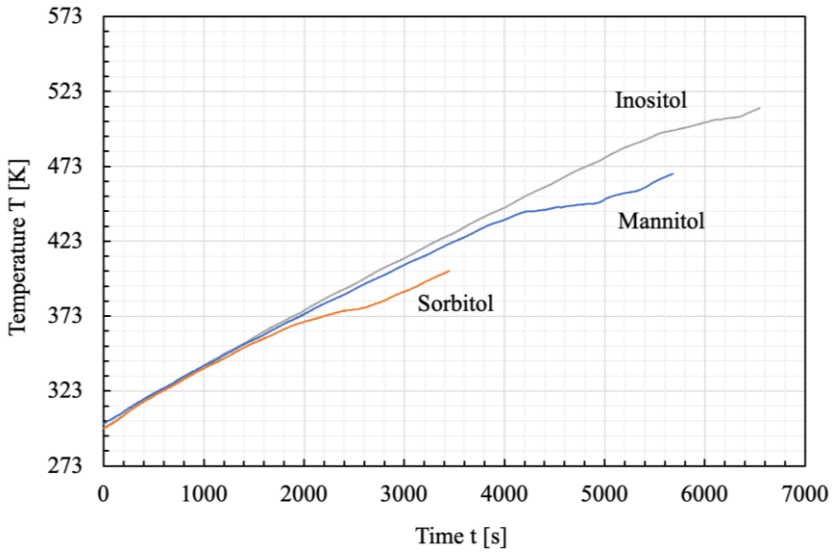

Figure 4. Relationship between the temperature and time at various materials.

Table 1. Comparison of melting temperature with literature values [14].

Materials	**Measured value (K)**	**Literature value (K)** [14]
Mannitol	439.05	439.35
Sorbitol	365.15	366.45
Inositol	496.05	498.65

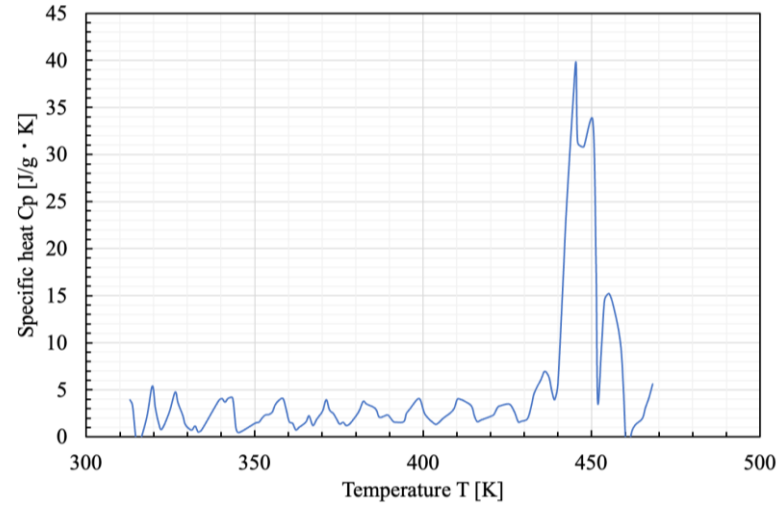

Figure 5. Specific heat of D-mannitol.

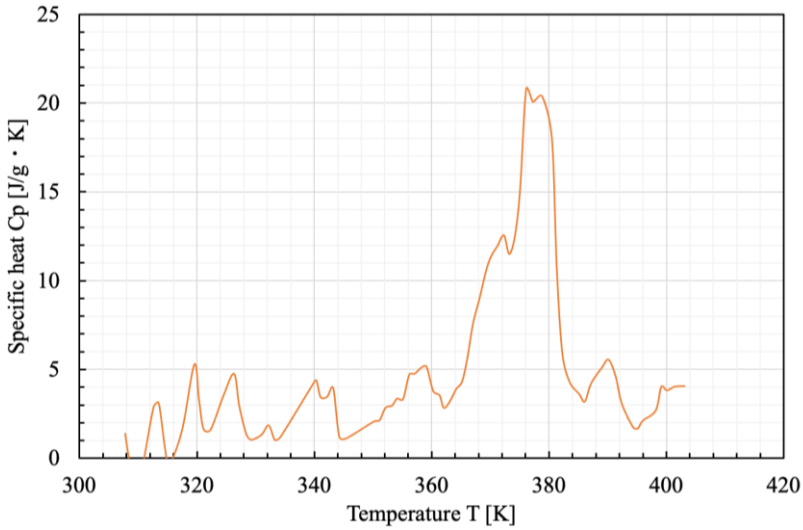

Figure 6. Specific heat of sorbitol.

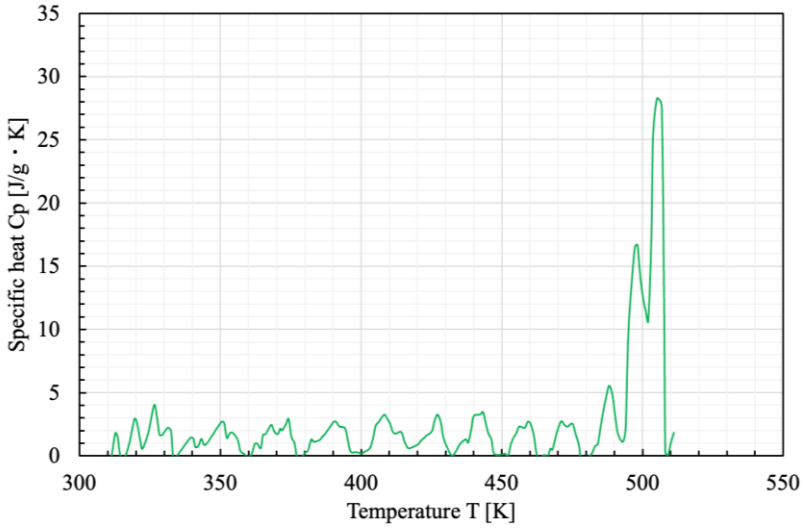

Figure 7. Specific heat of inositol.

Table 2. Average specific heat for each phase.

Material	Specific heat c_p (J/g·K)		
	Solid	Solid-Liquid	Liquid
Mannitol	2.58	18.40	2.17
Sorbitol	2.49	9.93	3.58
Inositol	1.43	14.50	0.99

3.2. Enthalpy and entropy of PCMs

Figure 8 shows the enthalpy stored by each material at various temperatures, which were calculated using Equation (2). As shown in **Figure 8**, the enthalpy of mannitol shows a linear increase from approximately 350 K to 440 K. This represents the sensible heat in the solid phase. After the melting point, the enthalpy increases, indicating the latent heat during the phase transition. The comparison shows that there is a significant difference in the stored thermal energy between the solid state and during the phase change. **Table 3** compares the latent heat for each material. From this table, it is clarified that mannitol stores the largest latent heat during the phase transition, followed by inositol and sorbitol, which have nearly equivalent values.

Table 3. Comparison of latent heat.

Material	Latent heat L (J/g)
Mannitol	394.2
Sorbitol	230.6
Inositol	229.0

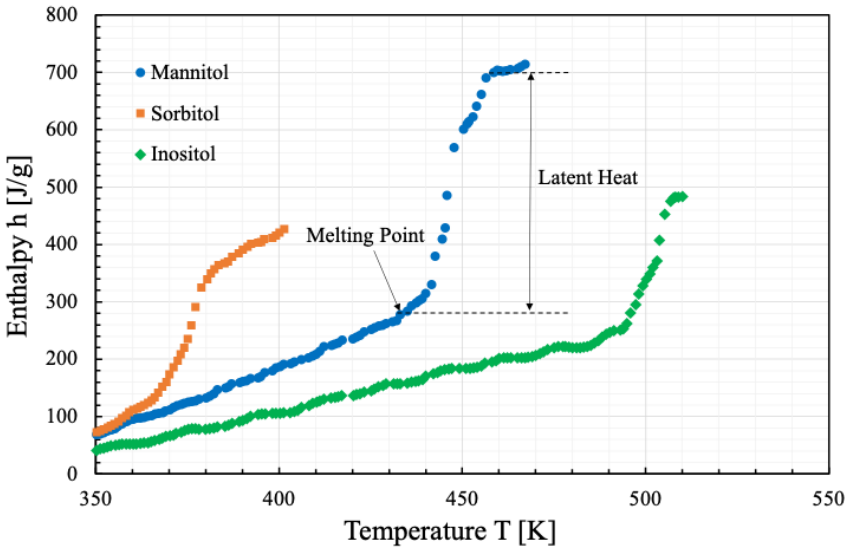

Figure 8. Enthalpy—Temperature curves.

Figures 9–11 show the entropy for each material, which were calculated using Equation (4). As shown in **Figure 9**, the entropy increases between 440 K and 460 K due to the latent heat of mannitol. For sorbitol and inositol, the entropy also increases due to the latent heat as shown in **Figures 10** and **11**. Since the latent heat of sorbitol is lower than that of mannitol, the entropy of sorbitol is also lower than that of mannitol

during the phase change. **Table 4** shows the average entropy values for each sample in the three phases. From this table, it is can be seen that the entropy of inositol has the lowest value in all phases.

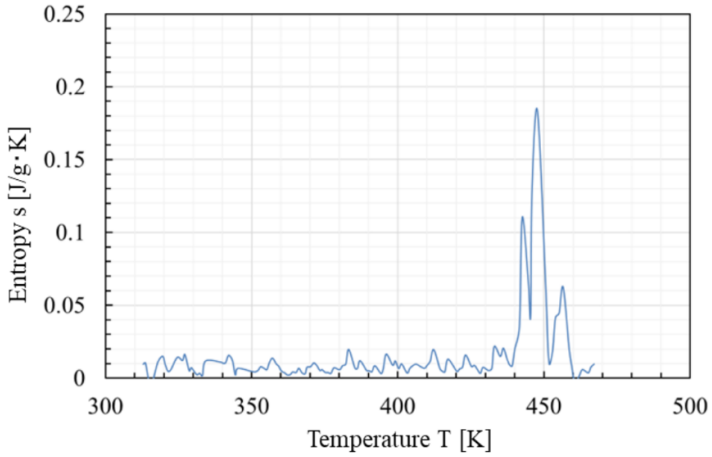

Figure 9. Entropy of mannitol.

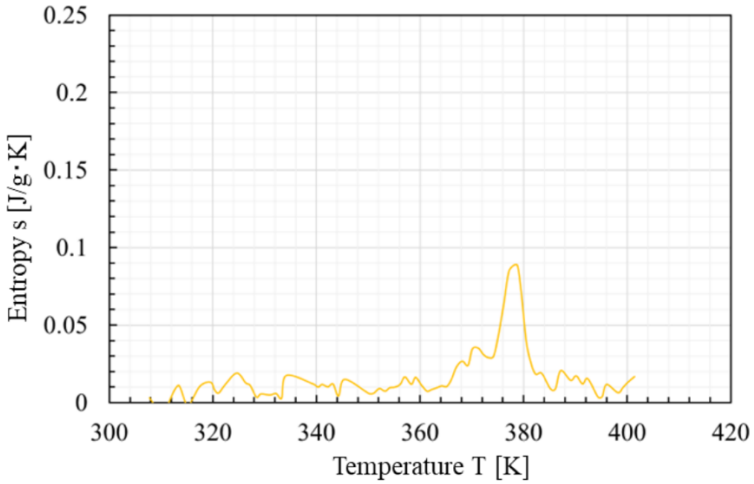

Figure 10. Entropy of sorbitol.

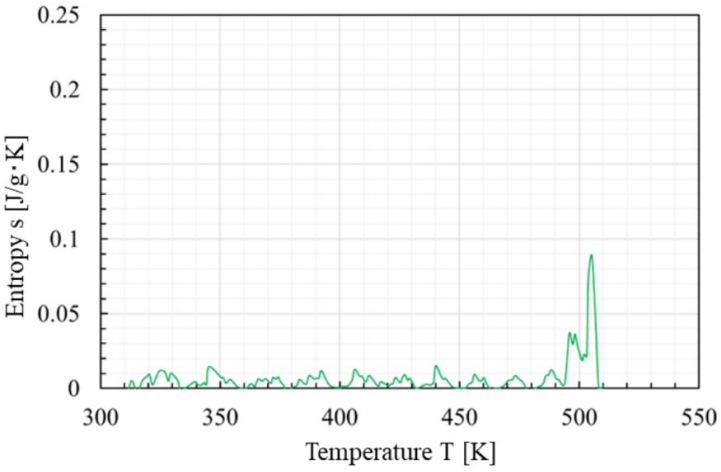

Figure 11. Entropy of inositol.

Table 4. Average entropy for each phase.

Materials	Entropy *e* (J/g·K)		
	Solid	Solid-Liquid	Liquid
Mannitol	0.008	0.049	0.004
Sorbitol	0.008	0.033	0.012
Inositol	0.004	0.029	0.001

3.3. Exergy evaluation of PCMs

Figure 12 shows the latent heat and exergy at an ambient temperature of 293 K for the measured samples. The exergy was obtained in Equation (3), which is the difference between the enthalpy integrated in Equation (2) and the entropy calculated in Equation (4). The latent heat for sorbitol, mannitol, and inositol were 230.6, 394.2, and 229.0 J/g, respectively, with mannitol indicating the highest latent heat value. Conversely, the exergy for sorbitol, mannitol, and inositol were 55.7, 136.5, and 95.5 J/g, respectively. Both the latent heat and exergy parameters substantiate mannitol's superiority as a latent-heat storage material. The values of the exergy during the phase transition and the percentage of the exergy relative to the latent heat are shown in **Table 5**. From this table, it is understood that the amount of heat extractable as work is less than 50% for all materials, and for sorbitol, approximately 75% of the heat cannot be utilized. Among these three materials, mannitol can store and extract more heat, making it an excellent heat-storage material. Therefore, in the next section, we investigate the effect of adding graphite to mannitol on its thermal responsiveness.

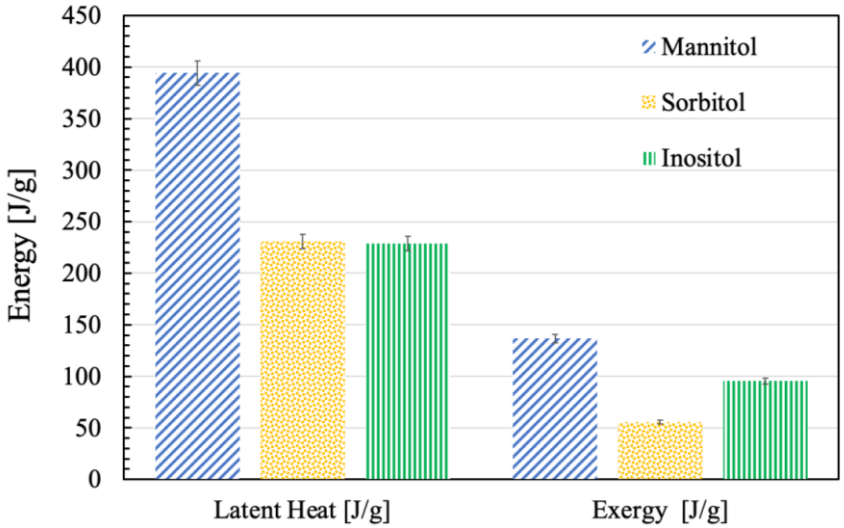

Figure 12. The latent heat and exergy evaluation of thermal storage materials.

Table 5. The exergy during the phase transition and the percentage of exergy relative to the latent heat.

Materials	Latent heat *L* (J/g)	Exergy *e* (J/g)	*e*/*L* (%)
Mannitol	394.2	136.7	34.7
Sorbitol	230.6	55.7	24.2
Inositol	229.0	95.5	41.7

3.4. Thermal responsiveness enhanced by graphite addition

Figure 13 shows the relationship between elapsed time and the temperature for mannitol with varying mass fractions of graphite powder. The temperature of pure mannitol increased with time as mentioned in **Figure 4**. As the graphite was added to the mannitol, the temperature gradient increased with graphite loading at around 500 s.

Thus, the temperature rises within the solid-phase region became faster, resulting in a shorter time to reach the melting point (439.35 K). After the phase transition, the temperature gradually increased and the heating of the heater was stopped. During cooling, the temperature of mannitol decreased rapidly, and supercooling occurs until it reaches around 423.15 K, below the melting point. As heat release due to solidification begins, the temperature rises to the original melting point, and the phase transition continues for about 400 s. Once the mannitol has transitioned to the solid phase, the temperature dropped to ambient.

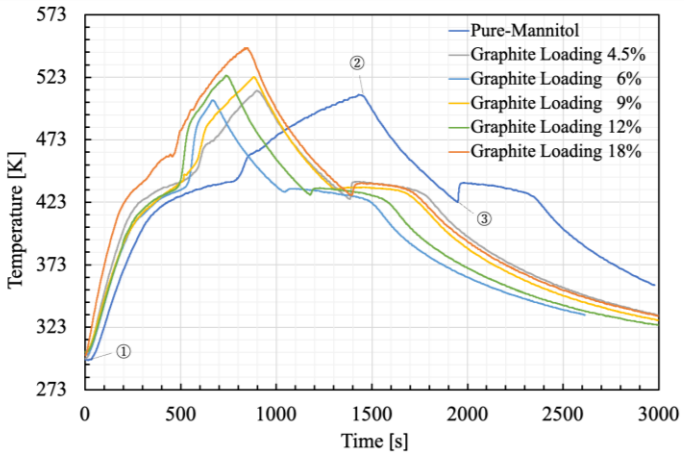

Figure 13. The effect of graphite loading on the thermal response of the PCM.

Figure 14 is an image captured from melting to solidification of pure mannitol. A series of the phase transitions can be observed in the images from left to right. It is considered that the partial melting due to natural convection occurred [8]. As the thermal stratification due to the natural convection has been developed in the PCM, the solid-liquid interface appeared as shown in **Figure 14**.

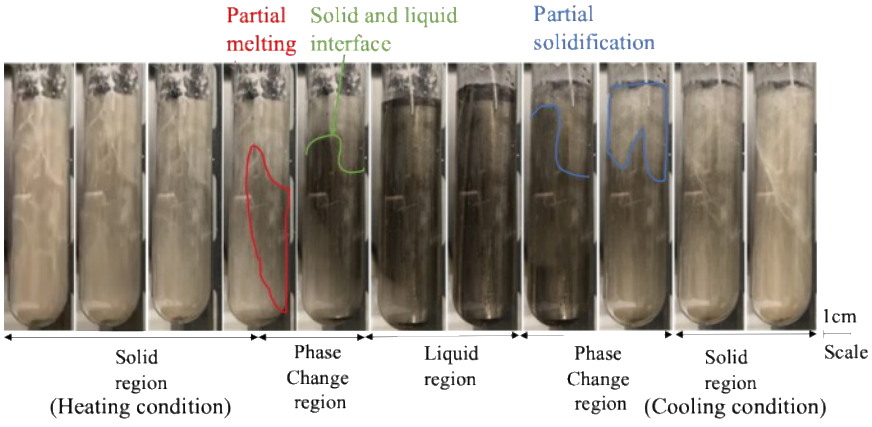

Figure 14. The phase change process of mannitol.

Figure 15 compares the dimensionless time required for pure mannitol to undergo the melting process as a reference. As the addition of graphite increases, the dimensionless time to reach the melting point becomes shorter, indicating improved thermal responsiveness. It seems that the thermal conductivity of the composite material could be enhanced by forming a complete phonon transmission channel by the addition of the graphite powder [17].

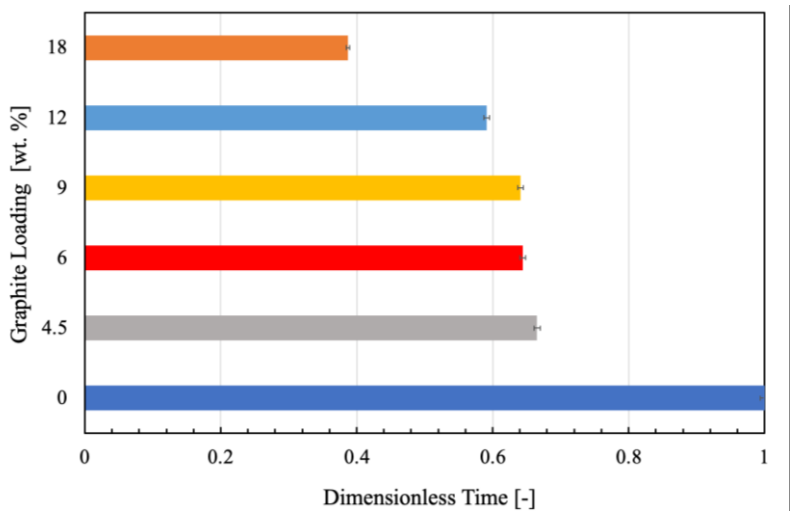

Figure 15. The dimensionless time required for phase transition.

Figure 16 illustrates the relationship between the graphite loading and the thermal energy charging. As the graphite loading increases, the stored energy decreases, indicating that graphite may penetrate between mannitol molecules, weakening the binding forces and causing such a phenomenon. In other words, as mentioned earlier, there is a trade-off between the thermal responsiveness and the thermal energy charging.

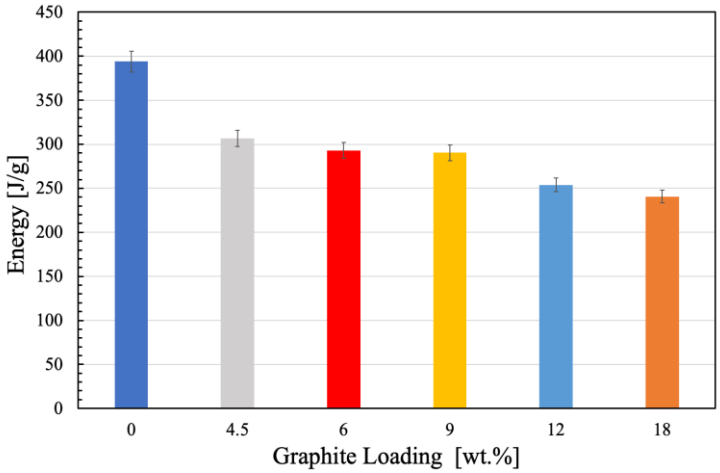

Figure 16. The relationship between the thermal energy charging and the graphite loading.

Figure 17 shows the relationship between supercooling and graphite addition. Supercooling was assessed as the difference between the melting point and the actual solidification temperature. It can be observed from this figure that the addition of

graphite reduces supercooling. The supercooling suppression by adding graphite powder of 9% was 37.5% compared to pure D-mannitol. It seems that the crystallization of D-mannitol was caused by heterogeneous nucleation on graphite surfaces, as the graphite powder was doped as the nucleation sites for crystal seeds [7,18]. Since the interfacial surface area between D-mannitol and the graphite with high thermal conductivity was expanded, it was understood that the heat conduction was improved and the crystal growth was promoted [19].

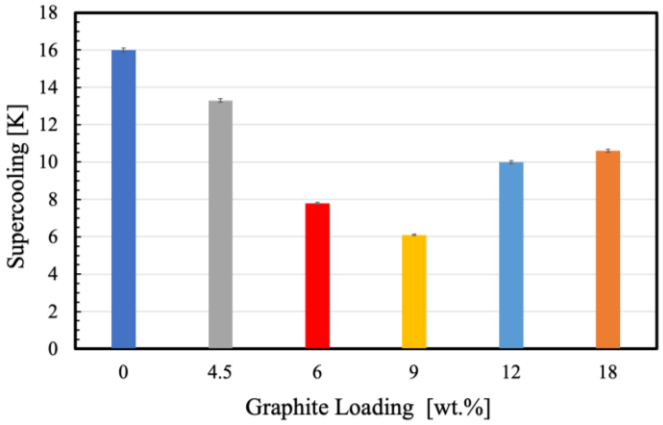

Figure 17. The relationship between supercooling and graphite loading.

4. Conclusion

The effect of adding graphite powder to D-mannitol at various mass percentages was investigated, experimentally. The key findings from this study are as follows.

- The experiments related to heat-response characteristics were conducted to improve the thermal response and to suppress supercooling with graphite additions.
- The enthalpy and entropy during the phase-change process were obtained by the measured specific heat of the PCMs.
- The specific heat of D-mannitol during the phase change process was higher than that of inositol.
- The addition of graphite powder at the mass fraction of 9% improves the thermal behavior of D-mannitol with lower supercooling while maintaining latent heat.
- The suppression of supercooling by the addition of 9% graphite powder was 37.5% compared to pure D-mannitol.

Author contributions: Study conception and design, MS, QL and SPF; data collection, MS and YH; analysis and interpretation of results, MS, YH, QL and SPF; draft manuscript preparation, MS, YH, QL and SPF. All authors have read and agreed to the published version of the manuscript.

Funding: This research was funded by JSPS KAKENHI grant number JP22K04562.

Conflict of interest: The authors declare no conflict of interest.

Nomenclature

Cp	Specific heat, J/g·K
I	Electric current, A
M	Mass, g
P	Heat input, W
Q	Power, W
R_s	Shunt resistance, Ω
T	Temperature, K
T_0	Ambient temperature, K
T_1	Reference temperature, K
T_2	Arbitrary temperature, K
V	Voltage of volt slider, V
V_R	Voltage of shunt resistance, V
$M'Cp'$	heat capacity of the vial, J/g·K
e	Exergy, J/g
h	Enthalpy, J/g
s	Entropy, J/g

Greek symbols

$\Delta\tau$	elapsed time, s

Subscripts

cj	cold junction
dl	data logger
tc	thermocouple

References

1. Alvi JZ, Feng Y, Wang Q, et al. Effect of phase change materials on the performance of direct vapor generation solar organic Rankine cycle system. Energy. 2021; 223. doi: 10.1016/j.energy.2021.120006
2. Bo H, Gustafsson EM, Setterwall F. Tetradecane and hexadecane binary mixtures as phase change materials (PCMs) for cool storage in district cooling systems. Energy. 1999; 24(12): 1015–1028.
3. Hidaka H, Yamazaki M, Yabe M, et al. Evaluation of Fundamental Characteristics of Threitol for Latent Heat Storage for Hot Water Supply. Kagaku Kogaku Ronbunshu. 2004; 30(4): 552–554.
4. Kageyama H, Hidaka H, Kubota M, et al. Study on the Initial Solidification Rate Acceleration of Erythritol Used for Latent Heat Storage. In: Proceedings of the 38th Annual Meeting on the Society of Chemical engineering; 16–18 September 2006; Fukuoka, Japan.
5. Shibahara M, Liu QS, Fukuda K. Thermal characteristics of phase change materials for waste heat recovery system. J Jpn Inst Mar Eng. 2015; 50(6): 63–70.
6. Yan L, Charles J, Romero EC, et al. Optimizing supercooling and phase stability by additives in calcium chloride hexahydrate for cyclical latent heat storage. Int Commun Heat Mass Transfer. 2023; 149. doi: 10.1016/j.icheatmasstransfer.2023.107119
7. Beaupere N, Soupremanien U, Zalewski L. Nucleation triggering methods in supercooled phase change materials (PCM), a review. Thermochim Acta. 2018; 670: 184–201.

8. Shibahara M, Liu QS, Fukuda K. Heat transfer characteristics of D-mannitol as a phase change material for a medium thermal energy system. Heat Mass Transfer. 2016; 52: 1993–2004.
9. Shibahara M, Liu QS, Fukuda K. Transient natural convection heat transfer of liquid D-mannitol on a horizontal cylinder. Renewable energy. 2016; 99: 971–977.
10. Mojiri A, Grbac N, Bourke B, Rosengarten G. D-mannitol for medium temperature thermal energy storage. Sol Energy Mater Sol Cells. 2018; 176: 150–156.
11. Karthikeyan S, Nagasudhan N, Nithin RA, et al. Transient numerical analysis on the melting characteristics of Paraffin and D-mannitol phase change materials for latent thermal energy storage. Mater. Today Proc. 2021; 45(7): 6306–6313.
12. Wang T, Liu Y, Meng R, Zhang M. Thermal performance of galactitol/mannitol eutectic mixture/expanded graphite composite as phase change material for thermal energy harvesting. J Energy Storage. 2021; 34. doi: 10.1016/j.est.2020.101997
13. Bai Y, Qiu W, Wang S. D-mannitol-based eutectic composite phase change materials with high thermal conductivity and solar-thermal conversion. Int J Energy Res. 2022; 46(11): 15722–15732.
14. Solé A, Neumann H, Niedermaier S, et al. Stability of sugar alcohols as PCM for thermal energy storage. Sol Energy Mater Sol Cells. 2014; 126: 125–134.
15. Jegadheeswaran S, Pohekar SD, Kousksou T. Exergy based performance evaluation of latent heat thermal storage system: A review. Renewable and Sustainable Energy Rev. 2010; 14(9): 2580–2595. doi: 10.1016/j.rser.2010.07.051
16. ANSI. Instruments and Apparatus. In: Measurement Uncertainty. American Society of Mechanical Engineers; 1985.
17. Wu S, Yan T, Kuai Z, Pan W. Thermal conductivity enhancement on phase change materials for thermal energy storage: A review. Energy Storage Mater. 2020; 25: 251–295.
18. Lane GA. Phase change materials for energy storage nucleation to prevent supercooling. Sol Energy Mater Sol Cells. 1992; 27: 135–160.
19. Wei C, Li Y, Song J, et al. Supercooling suppression and thermal conductivity enhancement of erythritol using graphite foam with ultrahigh thermal conductivity for thermal energy storage. Int. Commun Heat Mass Tranfer. 2024; 153.

Energy Storage and Conversion 2024, 2(4), 1546.
https://doi.org/10.59400/esc1546

Article

Holistic approach to energy storage management aspects in sustainable community

Grzegorz Augustyn*, Jerzy Mikulik

AGH University of Krakow, 30-059 Kraków, Poland
*** Corresponding author:** Grzegorz Augustyn, augustyngrzegorz@agh.edu.pl

CITATION

Augustyn G, Mikulik J. Holistic approach to energy storage management aspects in sustainable community. Energy Storage and Conversion. 2024; 2(4): 1546. https://doi.org/10.59400/esc1546

ARTICLE INFO

Received: 19 July 2024
Accepted: 15 October 2024
Available online: 28 November 2024

Abstract: Energy management is nowadays key topic for synchronic operation of renewable sources of energy and their recipients. Contemporary national electrical power grid systems more often cannot supply efficiently electrical energy and cannot receive energy produced by renewable sources. The common approach to the problem is to meet energy demands supplying from electrical grid and renewable power sources with energy storage feature. From the other side, off-grid solutions based on the co-generation biogas plants are commonly aimed on small local communities as power supply supported by renewable energy systems like photovoltaic (PV) systems, wind power plants or small water plants with energy storage to support self-consumption of electrical energy. Integration of intermittent renewable power sources, such as solar, wind and biogas plant, increases the difficulty of managing the electricity grid and maintaining the balance of electricity supply and demand, especially in small communities. The holistic approach to the energy storage management takes all above aspects and presents the concept where municipal waste is used to produce energy in biogas plant supported by PV systems and community shared electrical energy storage to provide uninterrupted power supply. The study also presents how energy storage management can be used in whole process to adjust the size and manage energy supply and demand within the community based on energy self-consumption optimization. It is also shown that by utilizing municipal waste produced by the community we can meet the goals of circular economy and sustainable development of local communities as the waste will be used in full without necessity of recycling it outside the community. The novelty of the study is the foundation for energy storage capacity and renewable energy sources size evaluation to balance energy management process without the need of on-grid power supply and with use only municipal biodegradable waste for biogas fuel supply and solar energy for energy production.

Keywords: energy storage; circular economy; energy management; sustainable community; circular economy

1. Introduction

The development of energy and the continuous development of urban areas have caused a real threat of rapid depletion of fossil fuels such as coal, crude oil, natural gas and progressive environmental pollution resulting from their combustion. This resulted in an increase in the content of carbon dioxide and other greenhouse gases and dust in the atmosphere. The increase in them and other greenhouse gases may affect global warming and the related weather anomalies [1]. Therefore, alternative ways of generating electricity from renewable energy sources (RES) have begun to develop [2].

Investing in RES has a more practical dimension and brings financial benefits. In addition to climate change, we experience constantly rising energy prices. Higher bills result from political conflicts and inflation, but mainly from the fact that we heat our homes and generate electricity using resource deficits [3]. RES are sources that use wind, solar, water, geothermal and biomass energy in the processing process. They use natural processes to produce electricity and heat and do not emit substances harmful to the environment. They are therefore clean, safe and planet-friendly energy [4]. There are many benefits to using RES. This is primarily related to ecology, because it does not contribute to the depletion of natural resources and pollution of the natural environment. Generating energy in this way means security and energy independence, as well as economic benefits [5,6].

The global energy industry is moving towards energy storage systems and renewable energy installations located close to end users and small local municipality. Such an approach fosters greater independence from imported energy sources and diversification of energy sources [7,8]. In times of crisis and political conflicts, these activities help to improve energy security and become more independent from countries exporting energy fuels. The research presents an idea for energy management concept which bonds together possible sources of energy and the ways of its production and storage to secure the local community power demands in the off-grid circular energy flow with ability to return the surplus energy to the power grid by using the ecological electrical energy production methods (PV and biogas plant) and utilizing the municipal waste produced by the local community towards self-sufficient energy management system [8].

This process allows to reduce greenhouse gas emissions, which is to improve air quality and stop climate warming [9] as well the use of the municipal waste which helps to minimize the amount of waste required utilization [10,11]. The other important aim is to provide the secure electrical energy supplies and electrical security for its local receivers by using their waste to fulfill power demands as well as commercial and industrial units [12].

As mentioned above biogas plant is the one of the key power sources in our concept of sustainable community energy production and management because for the production of biogas can be used biodegradable municipal waste (kitchen waste and green waste). Such waste is an important substrate. Biogas produced from waste in rural areas around cities has great potential to meet the energy needs of cities [13,14]. It can be also used for smaller communities especially if supported by PV systems which are commonly used in more number of households due to various government supporting programs [15–17].

The other direction is implementation of energy storage systems which increase the auto-consumption of electrical energy however it is very often part of the PV system to store the unused energy surplus for PV system for future use during the PV decreased efficiency during the day or season [18].

All these component systems are usually bonded together to create hybrid or off-grid micro-networks to better use the energy produced by biogas plants, PV and energy storage and to overcome the disadvantages and fluctuations of energy production in case of more or less predictable energy demands by the community of its recipients (householders) [19].

There is also important consideration in the terms of carbon emission policies which affects the urbanization process and from the other side urbanization itself has substantial influence on the carbonization and CO_2 global emission. Smaller community with less urbanization and population density can be also the solution for negative correlation between population density and per capita CO_2 emissions, which we can see especially for developing countries. With exception of China, CO_2 emissions trends are generally larger large cities or higher urbanization areas than the national averages. As the urbanization seems to be playing an increasing role in driving national emissions we can observe the importance of mitigation policies for cities [20]. Smaller communities which are using the hybrid renewable energy systems (HRES) or RES micro-networks as described above can be affected by these policies, however they can play an important role in whole process and strategy showing that smaller communities can provide solutions and contributions to this process. Urbanized areas consist of small communities of various size of population. The same approach in global strategy of decarbonization and lowering CO_2 emissions can be applied to local communities, especially when we consider divided areas around citied and suburban areas. Large urbanized areas consist of smaller areas and all actions taken at the lower level influences the result in more global scale. However, the policy for smaller communities and solutions developed to limit CO_2 emissions, even if appropriate to the national policy, can suffer from the same lack of over-national policies and face the same problems as described and suggested in [21]. We need to then consider that this is one of the ways to comply the general process and provide micro-scale solutions which might work in global-national, over-national or global scale.

2. Renewable energy solutions (RES) in on-grid and off-grid micro networks considerations

The main disadvantage of renewable energy is its unreliability and the inability to work efficiently due to the intermittent and fluctuating nature of the work, which usually leads to system oversizing, thus increasing the investment cost. For this reason, hybrid renewable energy systems (HRES—Hybrid Renewable Energy Systems) are built. Their popularity is due to the effectiveness of eliminating the disadvantages of RES systems based on a single source. A hybrid system consists of at least two power systems of different origins (renewable and fossil fuels), energy storage and electronic devices controlling them. The main advantages of HRES are: greater reliability, better efficiency, increased energy storage capacity, lower energy costs throughout the life cycle, minimization of greenhouse gas production [22]. Hybrid systems for the production of electricity can be a microgrid. It is a locally controlled energy system that uses:

1) different types of renewable energy sources: sun, wind, biomass or water,
2) energy generators (diesel, gasoline, biogas, biodiesel),
3) energy storage systems (batteries, hydrogen, heat),
4) loads (residential, commercial, industrial),
5) control devices (inverters and converters) [23].

There are two types of microgrid, a type of on-grid and off-grid. The former are connected to the national power grid, the latter are autonomous and operate outside the national power grid. The combination of photovoltaic technology and other RES with a biogas generator can be a profitable solution that will power even the most remote and sparsely populated rural areas. Such a hybrid system is optimal and less expensive than traditional. In off-grid networks, energy is generated by photovoltaic panels and a biogas generator, and stored in a battery bank. The batteries should have the capacity to power buildings for a certain number of days without sun, wind or biogas [23,24].

Building microgrids in which renewable energy is used brings environmental benefits such as reducing overall energy consumption, improving energy efficiency, reliability of energy supply, reducing transmission losses, voltage control and security of energy supply. HRES supports the implementation of sustainable development with the use of renewable energy [25]. The climatic risk is the occurrence of long interruptions in the supply of electricity from the national grid, caused by its damage due to weather factors, e.g. strong wind, snowfall or freezing rain [26]. Its occurrence and ailments are reduced by HRES microsystems independent of the national network, which are also an energy reserve for this network [27].

In rural and sparsely populated areas, terrain and economic considerations play an important role in planning the power grid. They make the importance energy produced from renewable sources, which are easy to install, have a higher rate of energy use, lower transmission losses and lower operating costs [24,25]. In addition, the use of environmentally friendly renewable energy sources in rural areas can reduce environmental pollution also in surrounding towns. The use of alternative energy sources makes communication more accessible and reduces dependence on fossil fuels, which reduces the negative impact on the environment [27].

Example of such approach is the designed by Habiba et al., who used kitchen waste from dormitories and hostels located on the university campus for the production of biogas. PV panels were installed on the roofs of these buildings [28]. More broadly, in cities and surrounding areas, a large amount of biodegradable municipal waste is generated from preparing meals (fruit and vegetable leftovers, groats, pasta, egg shells, coffee and tea grounds) and from home gardens (wood, leaves, flowers, small branches) [29]. It is estimated that an average household generates 60–80 kg/person/year of kitchen waste and 1.5–2 kg/m^2/year of green waste. [30]. On the island of Java there was proposed hybrid system consisting of a PV plant and a biogas plant. Electricity is produced by PV panels in the dry season (April–August) with a high intensity of sunlight (123–1075 W/m^2). The energy generated in this way can be stored in batteries, so it can be used by the inhabitants of the island at times when energy is not produced by PV panels. The strategy of the hybrid system work is that the PV panels produce electricity during the day, and the biogas plant generates electricity at night. Due to the climate on the island of Java, during the rainy season, the photovoltaic efficiency drops by 50%–70%. As a result, both RES systems can complement each other, constituting the optimal hybrid power system on this island [31]. The solution is also to create a system of effective distribution of energy generated from renewable energy. It is possible to build hybrid

energy grids parallel to the commercial grid. This solution can make electricity successfully distributed to rural and urban areas, which will solve the electricity problem [23,31]. This example also shows that for the local community we can provide the same strategy and by using the proper energy management inside the system by calculating the energy flow and routing between all its components can increase its efficiency in electrical energy production and consumption and what is more we could consider the prosumer mode when it is connected to the power grid network [32].

Some solutions for large scale storage for on-grid power networks for midsize or large communities shows the direction for electrical storage application based on packaged electrical energy system storage (EESS) [33]. Such applications allow for profile shifting and grid-demand support to better optimize energy consumption and storage balance, where battery balances and optimizes storage between on-grid power supply and PV installation or wind turbines. This direction for energy distribution and storage model does not assume self-sufficiency, however this solution gave the foundation for application storage for hybrid power systems [34] as well as shared community storage, where all participants can share common storage to optimize electrical energy distribution [35,36] by use of lithium-ion batteries or flow batteries. Further study on the optimization of storage, but from the cost point of view for various types of storage is shown in [37,38] where calculation method for energy storage was developed.

3. The concept of holistic approach to energy storage management

Energy systems are more commonly powered by renewable energy sources such as wind, solar and biogas. The main disadvantage of renewable energy is its unreliability and the inability to work efficiently due to the intermittent and fluctuating nature of the work, which usually leads to system oversizing, thus increasing the investment cost. Hybridization of energy sources increases the reliability of the energy system as a combination of two or more sources of electrical energy to provide reliable and uninterrupted power supply according to the local community needs. Implementing community shared electrical energy storage solution to the hybrid energy network solutions can create the opportunity to increase energy self-consumption and better energy management for long term perspective without on-grid power source.

In off-grid networks common approach, electrical energy is generated by photovoltaic panels supported by energy storage and a biogas plant. The batteries should have the capacity to power buildings for a certain number of days without sun, wind or biogas [23,24]. However, when we consider the small community there are still problems with adjusting the size of electrical energy storage and renewable energy sources especially if we consider that biogas energy production is based only on municipal biodegradable waste produced by the local community and we would like to stay with off-grid system to limit green gas emissions and use all municipal waste produced by the community.

The concept of holistic approach to electrical energy storage management combines the biogas plant and renewable energy sources, as well as community

shared electrical energy storage to achieve fully closed-circuit electrical energy flow for the small community. Such micro-network uses biodegradable waste for supply biogas plant electrical power production and use no other fuels or energy sources helps to increase sustainability in the waste management aspect. In this way we can advance process towards self-sufficient solution of electrical energy management with all advantages taken from other types of micro-networks adjusted to the small community scale. We would like to show that this approach allows for design of appropriate size of community shared energy storage size to ensure that energy management process can fully secure power demands, optimize the size of renewable power sources and helps to increase sustainability by municipal waste usage for electrical energy production in biogas plant.

Below on **Figure 1** there is a scheme presenting the concept of the holistic approach to energy storage management. As biogas plant can produce heat and electricity we will take into consideration only electricity production for further energy management consideration.

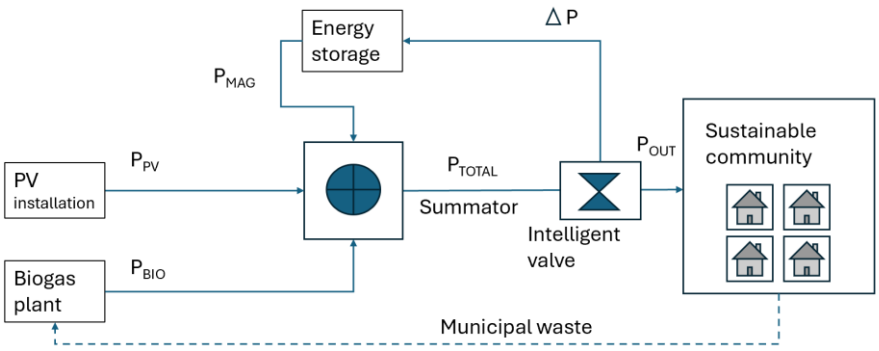

Figure 1. Diagram of energy flow where PPV—photovoltaic energy input, PBIO—biogas energy input, PMAG—energy storage input/output, ΔP—energy difference between demand and supply, POUT—energy demand directed to their recipients.

As the result we should improve energy efficiency, reliability and security of energy supply, eliminate waste utilization cost by using it as the fuel for biogas plant. We are not considering the cost or technical aspects of the set up or power grid details as our goal is to show how we can design he process to achieve uninterruptible power supply for households based on their own waste and renewable electrical energy production.

The resented idea is to connect all components: biogas plant, renewable energy source, electrical energy storage in the common circuit to manage electrical power production and storage in the way which allows for off-grid functionality with system size optimization by energy management algorithms. Main change is that energy storage is not attached to the specific power source, but it is common shared by the community.

It means that electrical energy storage which is not dedicated to PV installations but it is community shared electrical energy storage for all power sources as well as storage for excess electrical energy which is not used in the time instance by recipients (individual households). This should allow for smaller installation size and

better energy management with increased level of self-consumption as well as increased sustainability because biodegradable municipal waste will be used in full to produce electrical energy by biogas plant.

The key role in this concept plays the energy management algorithm which is applied to the distribution valve as the part of automation system, which manages the amount of energy which is routed to the common shared energy storage, which can be biogas plant, PV circuits or energy storage. The valve is responsible for adjusting the excess energy flow or making the decisions about energy storage during its energy production period or discharging the storage when the power demand excess energy production capabilities of the system.

In this model our system moving towards keeping the state of homeostasis where ΔP is the electrical energy balance as the measure of the process and shows the amount of excess electrical power produced by the system or demand for additional power by bonding together three input electrical power values P_{IN}, P_{OUT}, P_{MAG}.

P_{IN} is the summary of power sources like PV and biogas plant which are working with the certain production profile depending on the sun operation and community waste delivery and it is changing over the time period. P_{OUT} is the energy demand from the local recipients which is also expressed by the certain individual energy usage profile of individual household. Only the third variable—P_{MAG} is the variable which can be used as the source or load to the system and can be used to balance all three electrical power inputs with ΔP as the measure of the process. This concept is expressed in below Equation (1).

$$P_{PV}(t) + P_{BIO}(t) + P_{MAG}(t) - P_{OUT}(t) = \Delta P(t) \quad (1)$$

where:

P_{PV}—electrical power produced by the PV installation from all households

P_{BIO}—electrical power produced by the biogas plant by utilization of community municipal waste

P_{MAG}—discharging power of the community shared energy storage

P_{OUT}—power demand of households in the community

ΔP—power balance (excessive power produced or the difference between produced power by the biogas plant, PV installation and power demand of households)

Above equation gives foundation for the valve algorithm (**Figure 2**) which decides if the electrical energy is routed to charge the energy storage or discharge it to support power production from other sources biogas plant and PV installation as presented in [39].

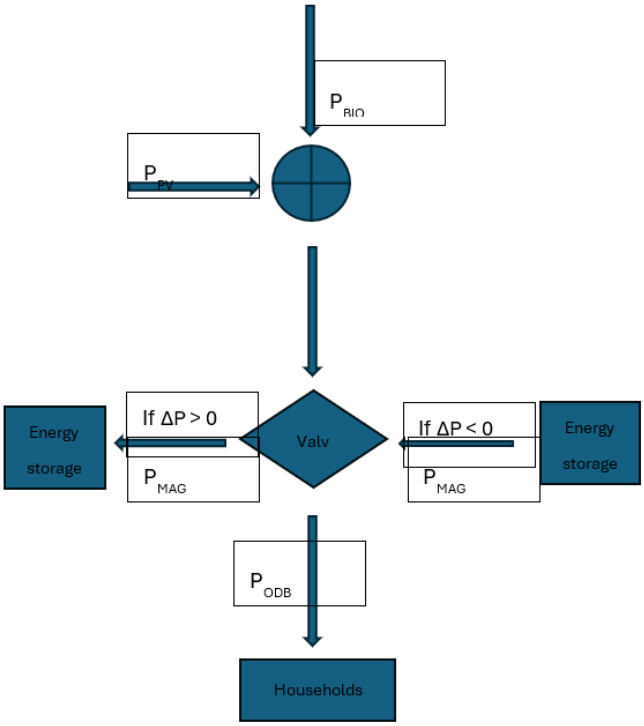

Figure 2. Valve algorithm where: PPV—photovoltaic energy input, PBIO—biogas energy input, PMAG—energy storage input/output, ΔP—energy difference between demand and supply, POUT—energy demand directed to their recipients.

The valve is responsible for routing the energy to the energy storage or supplying it back to the system when it is needed and individual recipients demand is more than PV installation and biogas plant can produce as presented in [39].

Based on Equation (1) when energy production by PV installation and biogas plant exceeds the P_{ODB} the energy surplus is routed to charge the energy storage. In this situation the valve acts as the exceed valve controlled by the proper calculation of C_n coefficient ($C_n > 0$), which is calculated by the measuring the energy demand in reference to the overall energy production by the PV installation and biogas. If the households are demanding more electrical energy than PV installation and biogas plant can produce ΔP is below zero, and C_n coefficient ($C_n < 0$ in this case) is calculated to evaluate the amount electrical energy from storage to be discharged as the additional electrical energy to the circuit to satisfy the current electrical power demand of the community.

Following above can calculate the size of common shared energy storage based on the maximum values of energy consumption for the community and maximum energy production from the power sources like biogas plant and PV installation. The energy storage size is the buffer which allows for balancing between the size of the PV installation having certain biogas electrical productions value and the individual household energy demand. We can also apply this to the predefined size of the community where each household has certain profile and produces adequate amount of municipal waste.

This model also allows for evaluation the power of the PV installation, when we consider biogas plant working on the certain municipal waste production profile and

determined size of the energy storage to keep the system balanced. In this scenario, energy storage should recover to its constant starting value at certain periods and system is able to provide energy to all its recipients.

4. Simulation

Simulations were taken based on following assumptions:

1) Local community with 10 average households (individual buildings)
2) Small biogas plant as one of the sources of electrical energy with municipal waste usage from 10 individual buildings in the same local community (av. 150 m^2, 4 persons),
3) 10 individual buildings in the same local community (av. 150 m^2, 4 persons) as the electrical energy recipients in the energy management process with average monthly energy consumption 3.5 kW,
4) Community shared generic energy storage based on lithium-ion battery system, minimum state of discharge 20%, daily discharge no more than 0.1%, which size will be determined as the result of simulation,
5) photovoltaic installation working at its average profile as the multiplication of 10 KWP standard size installation located at the South of Poland (Wieliczka county) installed at the roof with 27–32 degrees angle of each household,
6) 60 months simulation period, based on 12 months energy usage and production profiles

Based on the above assumption we were able to generate input data to the algorithm which allows to create two simulation scenarios:

(1) how energy storage charging and discharging process works in terms of various electrical energy production scenarios with various size of PV installation in this set up.
(2) What is the optimal size of the PV installation with certain electrical energy storage capacity to keep all energy management process self-sufficient

Following to above we need to define the energy requirement profile for the recipients during 12 months. Our recipients are 10 individual houses as the passive energy recipients and generating municipal waste to produce substrate for biogas plant.

The municipal waste amount produced over the year by the 10 households is shown in the **Table 1**. This data is used to calculate biogas annual electrical power production [39].

Table 1. Biodegradable municipal waste amount produced by 10 individual households and electrical produced by biogas plant over 12 months.

	Months											
	I	**II**	**III**	**IV**	**V**	**VI**	**VII**	**VIII**	**IX**	**X**	**XI**	**XII**
Municipal waste amount [kg]	50.0	52.5	87.5	215.0	390.0	422.5	390.0	372.5	360.0	415.0	450.0	120.0
Electricity [kW]	97.7	102.8	170.8	420	761.6	825.1	761.7	727.5	703.1	810.5	878.9	234.4

Power production profiles and power demands of individual households are taken form the literature [12] and available sources and calculations are based on the

regular average profile during the year. These data series are shown on the **Figure 3** when we can see the separate electrical energy profiles for the biogas plant electrical energy production from municipal waste supplied by 10 individual households, 10 KWP PV installation and average energy consumption of individual household over the year. The community itself and its contribution to the process is expressed by the electrical energy produces by PV installation and amount of municipal waste used for producing substrate to supply biogas plant.

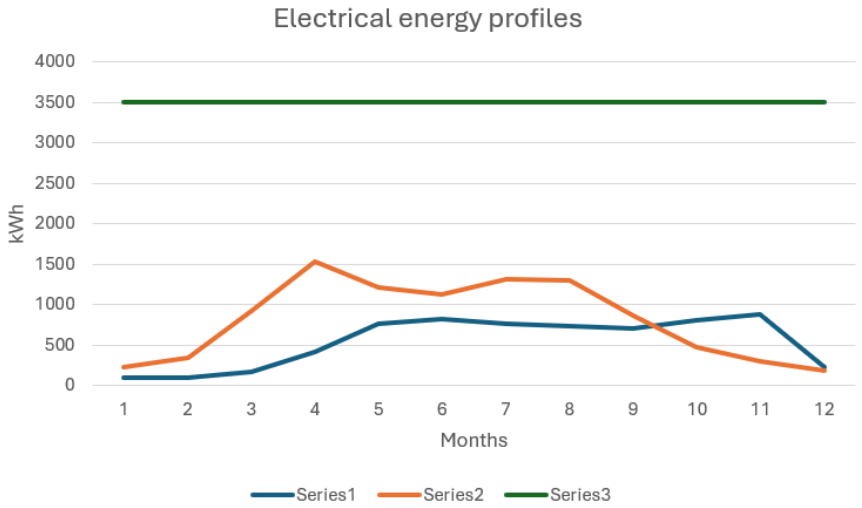

Figure 3. Electrical energy production profiles from installation components during the 12 months period, source [39].

We have defined now all necessary inputs for our simulations to calculate the amount of electrical energy which will be needed to charge the energy storage and which will be needed to cover the energy demands in the moments where its production is not able to fulfill recipients demands [2]. To properly calculate the value of the electrical energy which will be loading or discharging the energy storage we will need to take into account the loading process of the energy storage.

Our simulation assumes that excess electrical energy production from the previous period will be used to charge the energy storage. In this way we will be able to recharge and prepare the storage for the high energy usage when no energy will be produced by biogas plant or photovoltaic installation (e.g., during the night).

This can be expressed in the formula as below:

$$C_n = \frac{P_{MAG_{init}}}{P_{MAG_{init}} + \sum_{n=1}^{60} (P_{MAG_{init}} + \cdots + P_{MAG_{n-1}})} \quad (2)$$

where: $P_{MAG_{init}}$—initial value of electrical energy stored in the energy storage, n—time instance during a year calculated for every month in the 12 months period, where n = {1, 2, …, 12}, C_n—energy storage coefficient for the calculated time instance.

Our simulation for these assumptions and calculations is shown on **Figure 4** below where we present C_n coefficient values for certain biogas plant electrical power production profile and various energy storage initial value. We can see that

charging and discharging profile repeats in every 12 months as it is also reflects annual profiles for power production by the biogas plant and PV installation. We can see that excessive electrical power production is in the months where PV installation works at its best and community waste amount is higher than in the autumn and winter months. During these periods energy storage is mostly discharging to provide extra power to satisfy power demands of households. This shows what capacity should be considered as commune share energy storage to store enough electrical energy for the autumn and winter periods and keep electrical energy supplies uninterruptible for longer periods.

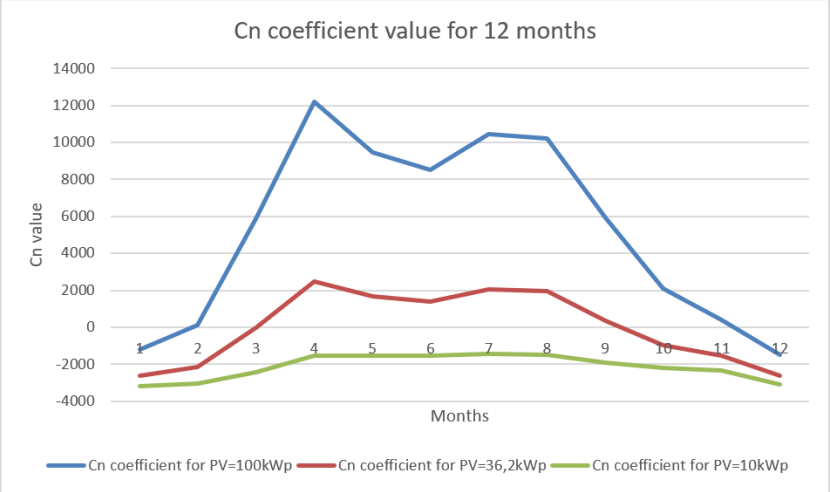

Figure 4. Cn coefficient values simulation for all elements of the circuits including energy storage management for three various sizes of PV installation over 12 months.

Above implicates that all electrical energy from biogas plant and photovoltaic installation is managed by the valve in the way that there is no necessity to connect to the electrical power grid and there is no electrical energy returned to the power grid as well.

We can also determine the size of the common share energy storage needed to sustain the process of the energy management in our micro network. The size can be determined by the analysis of coefficient profile. We cannot allow for constant discharging or charging profile. In the first case (PV = 10 KWP) constant discharging means that C_n is most of the time below zero which means that we need to supply additional power form external sources (such as national power grid). The second case (PV = 100 KWP) shows that we need to store excess energy every year without using it for the community demands. If we do not have connection to the national power grid we cannot consider sales of electrical energy surplus. That is why we need to adjust the size of the PV installation to keep C_n average profile close to zero value over the considered period. This case in our micro network is possible when PV installation is at 36.2 KWP. This is shown on the **Figure 5** where we simulate energy storage capacity for all three above sizes of PV installation.

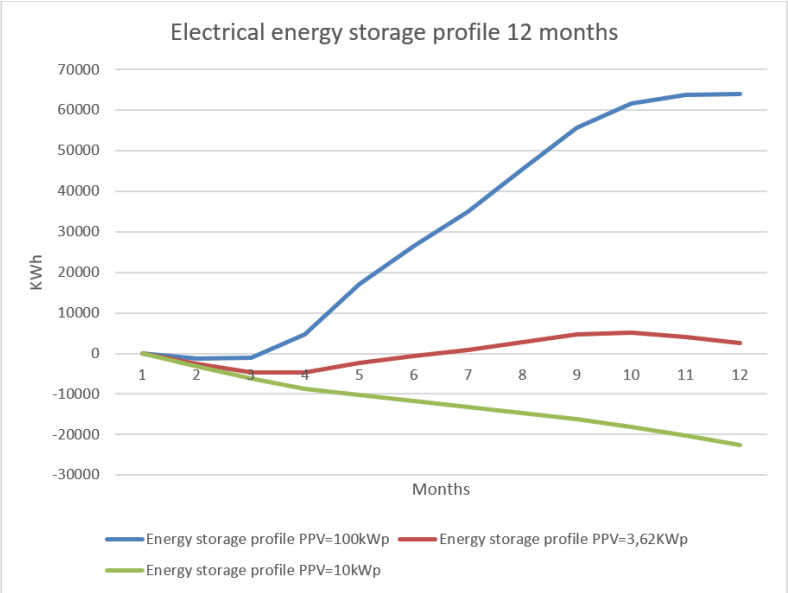

Figure 5. 12 months simulation of energy storage load/charging prediction based on the various scenarios of the PV size installation.

The result as of the simulations depicted on **Figure 5** show that for certain value of PPV installation size 36.2 KWP and energy storage capacity of 5100 kW, community energy demand and biogas plant size system is stable and keeps energy storage restored year by year in terms of charging-discharging profile for. For the other sizes of PPV the system stores too much energy or installation is not able to handle the energy demands of the community.

We can also observe similar patterns on all three cases. In the first quarter of the year electrical energy produced by the biogas and PV installation is not sufficient to supply the community. In this period storage is discharging and diminishing its initial stored energy amount (we can see also on **Figure 4** that C_n coefficient is below 0). Further on during the year community produces more waste (especially green waste) and sun operates longer during the day. Energy storage is recovering as the more excess electrical energy is produced. C_n coefficient is positive and more energy is stored in the battery. In the third and fourth quarter of the year the energy demand of the community raises (we can see it also thorough electrical energy profiles) and stored energy is used to support insufficient electrical energy production by the biogas plant and PV installation by discharging the storage.

We can see patterns as well in the C_n coefficient and energy storage profiles, but they are same shape but stretched or diminished depending on the amount of energy in the system. The coefficient is the base for the energy distribution process in the system, so it reflects in another patterns we can observe with every size of the PV installation, however when the installation is 100 KWP electrical energy produced by the installation is so excessive that at the end of the year we can see its cumulation over the community needs which shown as increasing energy amount over the year. If the PV installation is small (10 KWP) the system cannot cumulate enough energy and energy storage at the end of the year is discharged below its initial value. Only 36.2 KWP installation allows for restoring initial amount energy stored in the battery and provide stable cycle over the year. If we apply this to the

longer time period (more than one year) the process will repeat itself with end-of-year-initial values.

5. Discussion

The aim of this discussion is to evaluate if the concept of electrical energy storage management with common shared energy storage can be applied in sustainable community and under what conditions such approach can be realized.

First of all, we can see from above simulations that common shared electrical energy storage concept where it is dedicated to all power sources, not only for PV installation or biogas plant itself, reflects its bigger size as it has to store excess energy for a longer period of time. This solution is closer to the large scale storage where on-grid power plays significant role for the community.

In our concept small local community produces biodegradable waste to power up the biogas plant, which is one of the goals of the sustainability, despite the fact that biogas itself is considered as the low emission source of power. Biogas plant produces electrical energy, but its amount during 12 months is not enough to provide uninterruptible electrical power supply. From the other side considered community uses renewable energy source like PV installation to generate additional electric power to satisfy community electrical energy demands. This is also not sufficient to provide long term energy management. Both ways of electrical energy generation can use or dedicated storage or individual household storage. It is also worth of mention that individual household cannot produce electrical energy from PV installation even if supported by small individual electrical storage, to meet the energy demand of the single household and thus we need to consider on-grid connection. Introducing common shared electrical energy storage for the community makes possible to consider biogas plant supplied by the substrate from biodegradable community waste. Another source of electrical power is PV installation which usually is installed for each individual household with 10 KWP. Considering community of 10 households we can see certain electrical energy production and average electrical energy consumption profiles which can be balanced by common shared electrical energy storage if the storage will cover summary profile of electrical energy production. This allows for longer time storage of excess electrical energy in the periods where biogas plant and PV installation production exceeds individual households demands.

We can also observe from above simulations that biogas plant is dependent on the waste production amount in the annual period and electrical energy produced by PV installation is dependent on the average solar conditions. Both sources working together are very effective in the middle half of the year, however it exceeds individual households demands, but for the rest of the year they are not able to produce enough electrical energy to satisfy the needs of community. Common shared electrical storage with the proper management of electrical energy flow allows for electrical energy distribution between sources and its recipients allows for the longer period assuring the self-consumption without the need of on-grid connection.

Proposed algorithm for the valve, which is responsible for proper electrical energy routing backed up with common shared energy storage gives the opportunity

to balance all the process and leads to the introduction of global electrical energy management process for the community. The algorithm routes the excess electrical energy in the way as the excess valve works to the battery of common shared storage and discharge it when community demand exceeds the capabilities of current electrical energy production from biogas plant and PV installation. The formula for charging and discharging coefficient allows for estimation of storage size, which keeps the process balanced. It returns substantially large capacity, so it should be also considered further in terms of economical investment.

Energy storage management algorithm allows also for evaluation of the size of storage which is needed to balance all process through the year and provide uninterruptible electrical energy supply throughout considered period. However, we can observe that for the 10 KWP PV installation for the individual household we cannot charge the storage enough to avoid insufficient electrical energy supply. From the other side if we consider 100 KWP PV installation which means that every household has been equipped with 10 KWP installation, the excess energy charges the storage battery infinitely increasing year by year. Simulations shows that for certain parameter of the PV installation (36.2 KWP), at the constant biogas profile which is dependent on community waste production, we can achieve balance between charging and discharging the storage over the year without the need of on-grid connection and without exceed charging of the storage.

This also implicates that through this approach for the management of electrical energy in the community there is also possible to diminish and determine the correct PV installation size, which also can prevent such community against oversizing of the sources and storage. The other advantage in terms of sustainability is also the fact that we use all biodegradable community waste produced by households, so there is no need to external recycling and utilization.

Nevertheless, the results obtained in this research should be interpreted carefully as they are based on a simple case study. We still need to consider that electrical storage size and its evaluation can suffer from real world problems, charging and discharging effectivity, electrical energy losses, battery lifetime capacity loss and changes in annual community waste production and solar energy due to the weather changes. Also, we do not consider in detail technical aspects of electrical network which is needed for energy distribution like inverters, routers etc., however proposed algorithm can be used as the foundation for further, more detailed research for various starting conditions and disturbance which can influence the process. There is also a good starting point for artificial intelligence to evaluate and predict the process in more efficient way and in other scenarios or input conditions.

6. Conclusions

This research presented a novel holistic approach to the electrical storage energy management in the small local sustainable community where municipal waste is used for energy production in the local biogas plant supported by PV installation without on-grid power network connection. Such solution is possible because electrical energy storage is used as the common shared global storage for all power sources and recipients. Community also uses available resources (municipal waste

and solar energy) to produce electrical energy full filing the goals and direction for achieving better sustainability.

This research provides a method to optimally improve electrical energy storage management. The results are meant to demonstrate the capabilities of the electrical energy distribution circuit by using the method for calculating required storage size and renewable energy system. Presented algorithm for energy management and distribution using the valve shows that not only storage size might be determined, but also implicates certain size of PV installation preventing the system against oversizing.

Future research should investigate the impact of different conditions and distortions, changes in energy profiles that are used as the inputs for the energy management algorithm. These potential future investigations could also consider various emerging electrical energy storage technology that were not considered in this research to optimize the size and cost of the investment when considering application to the specific community. The other direction for further research is the possibility to include more advanced formulas or calculations methods for improving parameters calculations and algorithm adjustment for more precise and real-time management or fine tuning of the process, where local conditions vary in smaller periods of time (e.g., daily basis) and the electrical energy production profile have fluctuations or distortions in reference to the assumed electrical energy profiles. This should lead to size adjustment of the PV installation and electrical energy storage parameters selection to better reflects the action of the circuits and more efficient in cost and electrical energy security of the process in the smaller periods of time.

Finally, this approach indicates that common shared electrical energy storage used for energy management could be essential for the transition to a green economy and improve the sustainability and self-sufficiency for the small communities which can better manage their waste and resources.

Author contributions: Conceptualization, GA and JM; methodology, GA and JM; software, GA; validation, GA; formal analysis, GA and JM, investigation, JM; resources, GA; data curation, JM; writing—original draft preparation, GA and JM; writing—review and editing, JM; visualization, GA; supervision, JM; project administration, JM; and funding acquisition, JM. All authors have read and agreed to the published version of the manuscript.

Funding: This research was funded by AGH University of Krakow, Agreement DS No 16.16.200.396 B410 from AGH maintaining and development of research potential programmer.

Data availability statement: Data are contained within the article.

Conflicts of interest: The authors declare no conflict of interest.

References

1. Borowski PF. Biomass as a response to increased energy security and climate change (Polish). Przegląd Organizacji. 2008; 28-32. doi: 10.33141/po.2008.78.07

2. Chmielewski A, Gumiński R, Mączak J, et al. Aspects of balanced development of RES and distributed micro-cogeneration use in Poland: Case study of a μCHP with Stirling engine. Renewable and Sustainable Energy Reviews. 2016; 60: 930-952. doi: 10.1016/j.rser.2016.01.131
3. Cucchiella F, D'Adamo I, Gastaldi M. Financial analysis for investment and policy decisions in the renewable energy sector. Clean Technologies and Environmental Policy. 2014; 17(4): 887-904. doi: 10.1007/s10098-014-0839-z
4. Stanek W, Czarnowska L, Gazda W, et al. Thermo-ecological cost of electricity from renewable energy sources. Renewable Energy. 2018; 115: 87-96. doi: 10.1016/j.renene.2017.07.074
5. Ortega-Izquierdo M, del Río P. Benefits and costs of renewable electricity in Europe. Renewable and Sustainable Energy Reviews. 2016; 61: 372-383. doi: 10.1016/j.rser.2016.03.044
6. Burgos-Payán M, Roldán-Fernández JM, Trigo-García ÁL, et al. Costs and benefits of the renewable production of electricity in Spain. Energy Policy. 2013; 56: 259-270. doi: 10.1016/j.enpol.2012.12.047
7. Igliński B, Piechota G, Iwański P, et al. 15 Years of the Polish agricultural biogas plants: their history, current status, biogas potential and perspectives. Clean Technologies and Environmental Policy. 2020; 22(2): 281-307. doi: 10.1007/s10098-020-01812-3
8. Theuerl S, Kohrs F, Benndorf D, et al. Community shifts in a well-operating agricultural biogas plant: how process variations are handled by the microbiome. Applied Microbiology and Biotechnology. 2015; 99(18): 7791-7803. doi: 10.1007/s00253-015-6627-9
9. Bischoff A. Insights to the internal sphere of influence of peasant family farms in using biogas plants as part of sustainable development in rural areas of Germany. Energy, Sustainability and Society. 2012; 2(1). doi: 10.1186/2192-0567-2-9
10. Piskowska-Wasiak J. Obtaining and processing biogas from controlled fermentation of biodegradable fractions of municipal waste (Polish). Nafta-Gaz. 2015; 71(7): 510-519.
11. Kłos L. Municipal waste management a challenge of the 21st century (Polish). Studia i Prace Wydziału Nauk Ekonomicznych i Zarządzania. 2012; 28: 131-143.
12. Szyba M, Mikulik J. Analysis of Feasibility of Producing and Using Biogas in Large Cities, Based on the Example of Krakow and Its Surrounding Municipalities. Energies. 2023; 16(22): 7588. doi: 10.3390/en16227588
13. Tagne RFT, Dong X, Anagho SG, et al. Technologies, challenges and perspectives of biogas production within an agricultural context. The case of China and Africa. Environment, Development and Sustainability. 2021; 23(10): 14799-14826. doi: 10.1007/s10668-021-01272-9
14. Pathak H, Jain N, Bhatia A, et al. Global warming mitigation potential of biogas plants in India. Environmental Monitoring and Assessment. 2008; 157(1-4): 407-418. doi: 10.1007/s10661-008-0545-6
15. Szyba M. Spatial planning and the development of renewable energy sources in Poland. Acta Innovations. 2021; (39): 5-14. doi: 10.32933/actainnovations.39.1
16. Certificates of origin of electricity. Available online: https://www.biznes.gov.pl/pl/opisy-procedur/-/proc/207 (accessed on 3 April 2024).
17. Reference prices, Energy Regulatory Office. Available online: https://www.ure.gov.pl/pl/oze/aukcje-oze/ceny-referencyjne/6539,Ceny-referencyjne.html (accessed on 3 April 2024).
18. Yang Y, Bremner S, Menictas C, et al. Battery energy storage system size determination in renewable energy systems: A review. Renewable and Sustainable Energy Reviews. 2018; 91: 109-125. doi: 10.1016/j.rser.2018.03.047
19. Popczyk J. What does intelligent infrastructure mean in the civilization transformation of energy and where is its place (Polish). Warszawa, Poland; 2018. pp. 6-27.
20. Labzovskii LD, Mak HWL, Takele Kenea S, et al. What can we learn about effectiveness of carbon reduction policies from interannual variability of fossil fuel CO_2 emissions in East Asia? Environmental Science & Policy. 2019; 96: 132-140. doi: 10.1016/j.envsci.2019.03.011
21. Luqman M, Rayner PJ, Gurney KR. On the impact of urbanization on CO_2 emissions. npj Urban Sustainability. 2023; 3(1). doi: 10.1038/s42949-023-00084-2
22. Document of the Council of Ministers, Directions of development of agricultural biogas plants in Poland in 2010-2020 (Polish). Available online: https://www.pigeor.pl/media/js/kcfinder/upload/files/Kierunki-Rozwoju-Biogazowni-Rolniczych-w-Polsce-na-lata-2010--2020.pdf (accessed on 21 March 2024).

23. Yimen N, Hamandjoda O, Meva'a L, et al. Analyzing of a Photovoltaic/Wind/Biogas/Pumped-Hydro Off-Grid Hybrid System for Rural Electrification in Sub-Saharan Africa—Case Study of Djoundé in Northern Cameroon. Energies. 2018; 11(10): 2644. doi: 10.3390/en11102644
24. Chowdhury N, Akram Hossain C, Longo M, et al. Feasibility and Cost Analysis of Photovoltaic-Biomass Hybrid Energy System in Off-Grid Areas of Bangladesh. Sustainability. 2020; 12(4): 1568. doi: 10.3390/su12041568
25. Tiwari Y, Prashansa P, Chaudhary SK. A study of solar and biogas hybrid power generation system with max power tracking by solar panel. Int. J. Electr. Electron. Eng. 2015; 7: 257-266.
26. Juhola S, Laurila A, Groundstroem F, et al. Climate risks to the renewable energy sector: Assessment and adaptation within energy companies. Business Strategy and the Environment. 2023; 33(3): 1906-1919. doi: 10.1002/bse.3580
27. Jumare IA, Bhandari R, Zerga A. Assessment of a decentralized grid-connected photovoltaic (PV) / wind / biogas hybrid power system in northern Nigeria. Energy, Sustainability and Society. 2020; 10(1). doi: 10.1186/s13705-020-00260-7
28. Habiba U, Talukdar SK, & Islam MR. Designing Solar and Biogas based Renewable Energy System on University Campus and its Impacts on Energy Cost after Renewable Energy Interconnection to the University Grid Network. Global Journal of Research in Engineering. 2013; 13(13): 1-11.
29. MPO Krakow. Available online: https://mpo.krakow.pl/pl/mieszkancy/selekcja/zasady (accessed on 14 May 2024).
30. Estimation of the composting level of bio-waste (Polish). Available online: https://odpady.net.pl/wp-content/uploads/2021/05/Zalacznik-3-18.5-1.pdf (accessed on 19 May 2024).
31. Mudgal V, Reddy KS, Mallick TK. Techno-Economic Analysis of Standalone Solar Photovoltaic-Wind-Biogas Hybrid Renewable Energy System for Community Energy Requirement. Future Cities and Environment. 2019; 5(1). doi: 10.5334/fce.72
32. The Polish Chamber of Commerce for Renewable and Distributed Energy (PIGEOR). Biogas. Available online: https://www.pigeor.pl/biogaz (accessed on 28 March 2024).
33. Sepulveda NA, Jenkins JD, Edington A, et al. The design space for long-duration energy storage in decarbonized power systems. Nature Energy. 2021; 6(5): 506-516. doi: 10.1038/s41560-021-00796-8
34. Wang X, Shen Y, Su C. Exploring the willingness and evolutionary process of public participation in community shared energy storage projects: Evidence from four first-tier cities in China. Journal of Cleaner Production. 2024; 472: 143462. doi: 10.1016/j.jclepro.2024.143462
35. Farah S, Andresen GB. Investment-based optimisation of energy storage design parameters in a grid-connected hybrid renewable energy system. Applied Energy. 2024; 355: 122384. doi: 10.1016/j.apenergy.2023.122384
36. Kenyon G. Electrical Energy Storage: An introduction, The Institution of Engineering and Technology. London, United Kingdom The Institution of Engineering and Technology; 2016
37. Shekhar R, Kumar P. Hybrid Energy Storage System using Wind power system, Journal of Power Technologies. 2024; 104(3): 181-188
38. Stenclik D, Denholm P, Chalamala B. Maintaining Balance: The Increasing Role of Energy Storage for Renewable Integration. IEEE Power and Energy Magazine. 2017; 15(6): 31-39. doi: 10.1109/mpe.2017.2729098
39. Augustyn G, Mikulik J, Rumin R, et al. Energy Self-Sufficient Livestock Farm as the Example of Agricultural Hybrid Off-Grid System. Energies. 2021; 14(21): 7041. doi: 10.3390/en14217041

Energy Storage and Conversion 2024, 2(4), 2074.
https://doi.org/10.59400/esc2074

Article

Effective Nano-manufacturing of T-Nb_2O_5 for supercapacitor applications

Surjit Sahoo[1,2,*], Anand Kumar Gandham[1], Vijay Kumar Pal[1,*]

[1] Mechanical Engineering Department, Indian Institute of Technology, Jammu 181221, India
[2] Department of Industrial and Manufacturing Systems Engineering, Kansas State University, KS 66506, USA
*** Corresponding authors:** Surjit Sahoo, surjit488@gmail.com; Vijay Kumar Pal, vijay.pal@iitjammu.ac.in

CITATION

Sahoo S, Gandham AK, Pal VK. Effective Nano-manufacturing of T-Nb2O5 for supercapacitor applications. Energy Storage and Conversion. 2024; 2(3): 2074. https://doi.org/10.59400/esc2074

ARTICLE INFO

Received: 18 October 2024
Accepted: 20 November 2024
Available online: 28 November 2024

Abstract: Characterized by unique physical and chemical properties, metal oxide materials have garnered significant attention for research and development in energy storage device applications. In the current work, we present a simple and low-cost synthesis protocol for orthorhombic-phase niobium oxide (T-Nb_2O_5) electrodes, aimed at supercapacitor applications. The as-prepared T-Nb_2O_5 was characterized utilizing field emission scanning electron microscopy, X-ray diffraction, and energy-dispersive X-ray spectroscopy, confirming the formation of orthorhombic-phase T-Nb_2O_5 nanoparticles. Detailed electrochemical analyses were conducted on T-Nb_2O_5, utilizing 1 M LiOH as the electrolyte. The unique nanoparticle architecture of T-Nb_2O_5 offers abundant electro-active sites and enhances reaction kinetics, leading to high specific capacitance. Notably, the T-Nb_2O_5 electrode achieved a gravimetric capacitance of approximately 23 F g^{-1} at the lowest sweep rate (5 mV s^{-1}). These findings highlight the potential of T-Nb_2O_5 as an effective electroactive material for supercapacitors.

Keywords: hydrothermal; T-Nb_2O_5; nanoparticles; specific capacitance; supercapacitors

1. Introduction

In the present age, electrochemical energy storage devices are key for tackling non-renewable energy source depletion and reducing the impact of global warming. Amid these devices, lithium-ion batteries (LiBs) and supercapacitors have attracted significant attention due to their widespread industrial and daily applications, owing to their high-specific power, rapid charge-discharge rates, and prolonged cyclic stability [1–3]. Supercapacitors, comprising electrochemical double-layer capacitors (EDLCs) and pseudocapacitors, provide the benefit of rapid energy release via fast surface or near-surface electrochemical reactions, including physical adsorption/desorption or Faradaic processes [4]. In both EDLCs and pseudo capacitors, carbon-based materials, transition metal oxides, and transition metal hydroxides are widely used as electroactive materials in academic research and industrial applications. Transition metal oxides are considered an aspiring candidate for use as electrodes in energy storage devices due to their abundant availability, eco-friendliness, and ease of accessibility [5]. These materials also possess a variety of attractive features, including diverse compositions and morphologies, large surface areas, and high theoretical gravimetric specific capacitance. Moreover, transition metal oxides are crucial in the electrodes of electrochemical supercapacitors, as they significantly enhance capacitance by enabling precise adjustment and control of defects and surface/interfaces at the nanoscale [6].

Metal oxides, including cobalt oxide, iron oxide, nickel oxide, and manganese oxide, serve as advantageous electrodes for supercapacitors due to their unique chemical and physical properties, as well as their high specific capacity and

capacitance, which substantially surpass those of carbon-based electrodes. Among various metal oxides, Nb_2O_5 exhibits various stoichiometries and crystal structures that depend on the synthesis method and has been extensively studied as a high-capacity material for energy storage applications [7–11]. In the last few years, T-Nb_2O_5 has emerged as a promising anode material for Na^+ and Li^+ storage due to its large interplanar lattice spacing along the (001) plane and its characteristic pseudocapacitive behavior [12–19]. However, there are limited reports on the use of T-Nb_2O_5 as an electrode material for supercapacitors. At first, Kong et al. [20] reported free- standing T-Nb_2O_5/graphene composite papers for Li-intercalating pseudocapacitive electrodes. The T-Nb_2O_5/graphene composite paper obtained a gravimetric and volumetric capacitance of 620.5 F g^{-1} and 961.8 F cm^{-3} at 1 mV s^{-1}.

Later on, Jiang et al. [21] synthesized T-Nb_2O_5/N-doped carbon nanosheets for use in lithium-ion capacitors. These lithium-ion capacitors, based on T-Nb_2O_5/N-doped carbon nanosheets, achieved an energy density of approximately 70.3 Wh kg^{-1} and a power density of 16,014 W kg^{-1}. Furthermore, Zhang and their colleagues [22] prepared T-Nb_2O_5 nanoparticles confined within a porous carbon shell for use in a Hybrid supercapacitor, achieving a maximum specific capacity of 410 Fg^{-1} at a Current density of $1Ag^{-1}$. These electrochemical studies suggest that additional research is needed to further study the electrochemical behavior of bare T-Nb_2O_5 as an electroactive material for energy storage systems.

Therefore, in the current work, we synthesized bare T-Nb_2O_5 utilizing the hydrothermal method and conducted electrochemical evaluations as supercapacitor electrodes, using both half-cell and symmetric supercapacitor devices.

2. Experimental methods

2.1. Materials

Niobium(V) chloride [$NbCl_5$], Ethanol [C_2H_5OH], and Lithium hydroxide [LiOH] were purchased from Sigma Aldrich, India. Polyvinylidene fluoride (PVDF) and Carbon black were obtained from Sigma Aldrich, India.

2.2. Growth of T-Nb_2O_5 nanostructure

All chemical reagents were directly used as purchased without further purification. A highly reproducible hydrothermal method was used to prepare a uniform amorphous precursor. In a typical method, 2 mmol of $NbCl_5$ was dissolved in 50 mL of ethanol, resulting in a yellow solution, which was stirred for 30 min until it became a colorless solution. After adding 20 mL of deionized water and stirring for 2 h, the opaque sol was transferred to a Teflon autoclave and sealed within a steel container. The autoclave was then heated to 200 °C for 12 h and subsequently cooled naturally. Once the reaction was complete, the precipitates were extracted from the autoclave and washed several times with water and ethanol to remove any residues. The collected powder was then dried overnight at 60 °C. Finally, the dried sample was annealed at 600 °C for 2 h.

2.3. Physical characterization

X-ray diffraction (XRD) analysis of the as-prepared T-Nb_2O_5 was conducted utilizing an XRD instrument bought from Malvern Panalytical equipped with Cu-Kα radiation (λ = 1.54184 Å), operating at a high voltage of 30 kV and a current of 30 mA. The surface morphology of the prepared T-Nb_2O_5 nanostructure was examined utilizing FESEM (JEOL JSM 7900F) at various magnifications.

2.4. Electrochemical characterization

The electrode material was prepared utilizing the slurry coating technique. In brief, the electroactive material (T-Nb_2O_5), PVDF and carbon black were mixed in a weight ratio of 80:5:15 with N-methyl pyrrolidone (NMP) as the dispersant. The mixture was ground for a few hours in an agate mortar to make a uniform slurry. The slurry was applied onto a stainless-steel substrate and dried at 55 °C for 8 h.

The electrochemical characterization of T-Nb_2O_5 was carried out utilizing a three-electrode system in a 1.0 M LiOH electrolyte, where Ag/AgCl was used as the reference electrode, platinum foil as the counter electrode, and T-Nb_2O_5-coated stainless steel as the working electrode.

A T-Nb_2O_5//T-Nb_2O_5 symmetric supercapacitor device (SSD) was constructed by inserting a polypropylene separator between two stainless steel electrodes coated with T-Nb_2O_5. The electrochemical performance of both the T-Nb_2O_5 electrode and the T-Nb_2O_5//T-Nb_2O_5 SSD was evaluated through charge-discharge (CD), cyclic voltammetry (CV), and electrochemical impedance spectroscopy (EIS) utilizing an electrochemical workstation. The specific capacitance of the T-Nb_2O_5 electrodes was calculated using the following Equations (1) and (2):

$$Specific\ capacitance = (\int IdV)/(s \times \Delta V \times m) \quad (1)$$

$$Specific\ capacitance = (I \times \Delta t)/(\Delta V \times m) \quad (2)$$

here, "I" is the current (A), "ΔV" is the potential window, specific capacitance in F g^{-1}, "s" is the scan rate (mV s^{-1}), "Δt" is the discharge time (s), and "m" is the mass of the electroactive material coated on the substrate.

3. Results and discussion

The T-Nb_2O_5 was synthesized using a hydrothermal method, followed by post-annealing. The XRD pattern of T-Nb_2O_5 is illustrated in **Figure 1a**, which indicates that the crystal structure of pure Nb_2O_5 aligns closely with the standard peaks for T-Nb_2O_5 (JCPDS No. 30–0873) [23]. The peaks at 22.79°, 28.50°, 36.83°, 42.88°, 45.31°, 46.47°, 50.06°, 51.04°, 55.43°, 56.57°, 59.02°, 63.93°, 71.26°, and 77.95° correspond the (001), (100), (181), (130), (110), (002), (301), (331), (182), (381), (160), (161), (382) and (122). To examine the microstructure and morphology of the as-synthesized sample, scanning electron microscope (SEM) analysis was conducted, as presented in **Figure 1b** and **Figure 1c**. The SEM micrograph discloses the growth of Nb_2O_5 nanoparticles with an average size of around 30–40 nm. Additionally, EDS analysis (as presented in **Figure 1d**) was performed to confirm the presence of niobium and oxygen elements in the sample. The overlay elemental mapping of

Nb_2O_5 nanoparticles, shown in **Figure 1e** and **Figure 1f**, demonstrates the uniform distribution of niobium and oxygen elements throughout the sample [24].

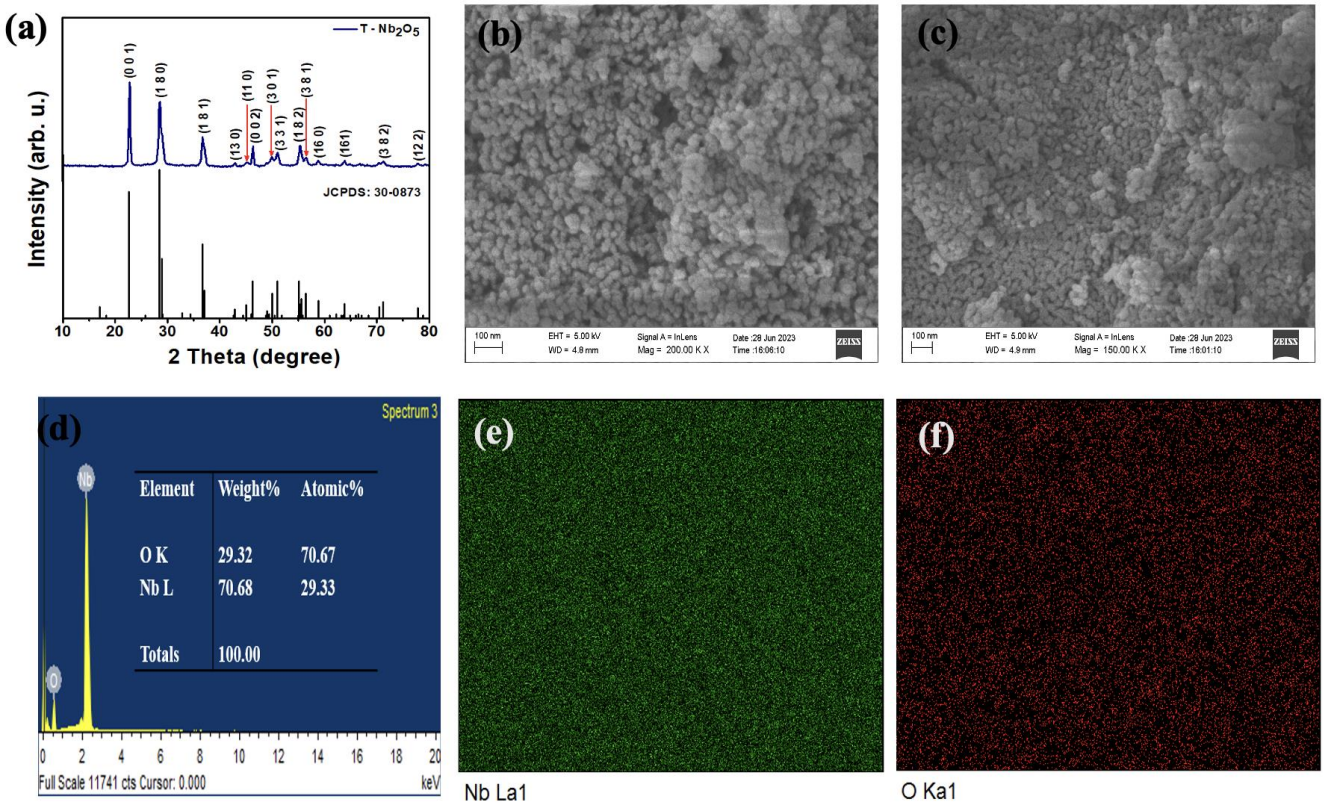

Figure 1. (a) XRD pattern of as-prepared T-Nb_2O_5. FE-SEM micrographs of T-Nb_2O_5; **(b–c)** at various magnifications (200.0 kx, and 150.0 kx); **(d)** the EDS spectrum of as-prepared T-Nb_2O_5. The elemental mapping of T-Nb_2O_5; **(e)** niobium; **(f)** oxygen element.

To evaluate the supercapacitive performance of the T-Nb_2O_5 nanoparticles, cyclic voltammetry (CV) tests and galvanostatic charge-discharge (CD) cycling were conducted in a three-electrode system. The CV profile of T-Nb_2O_5 was conducted (as presented in **Figure 2a**) in the potential range of −1.0 to 0.2 V at various scan rates of 5 to 100 mV s^{-1}. The CV profile illustrates that it is different from EDLC-based material. It can be perceived that strong redox peaks are noticeable in each CV profile, signifying that the measured electrochemical performance is mostly founded on the redox mechanism or pseudocapacitive behavior of Nb_2O_5 [25]. The anodic and cathodic peaks in the CV profile appear at 0.35 V and 0.50 V, respectively.

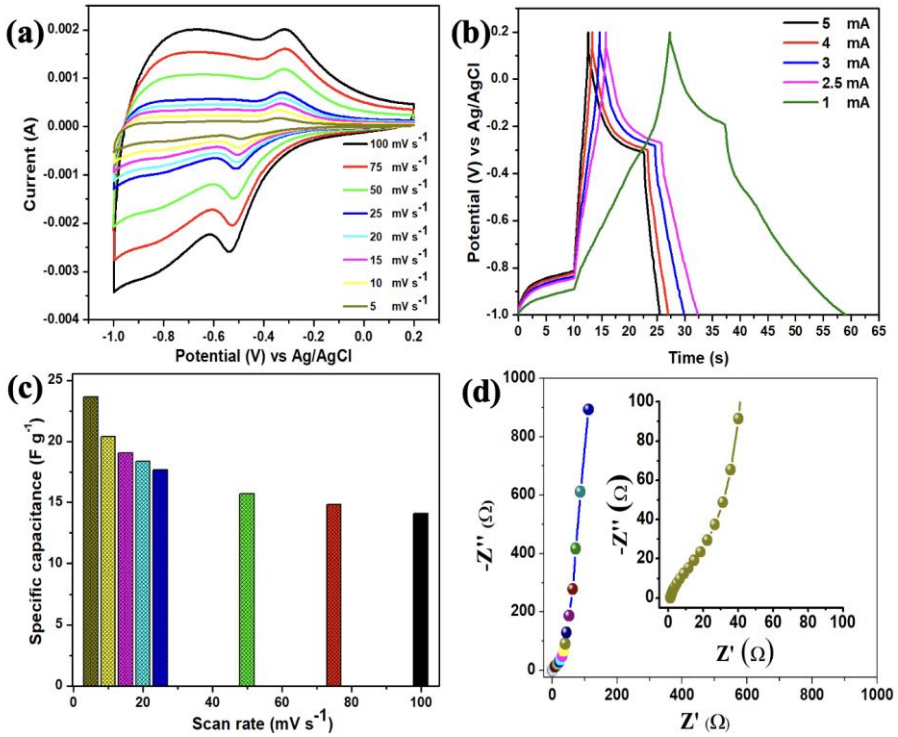

Figure 2. Electrochemical characterization of T-Nb_2O_5 electrode in a three-electrode system. **(a)** CV curves of T-Nb_2O_5 electrode at various scan rates (5–100 mV s^{-1}); **(b)** CD profile of T-Nb_2O_5 electrode at various applied currents (1–5 mA); **(c)** effect of scan rates on specific capacitance of T-Nb_2O_5 electrode; and **(d)** the Nyquist plot T-Nb_2O_5 electrode with inset shows the enlarged view.

These peaks are attributed to the intercalation and deintercalation of lithium ions at the surface of the T-Nb_2O_5 electrode, indicating its pseudocapacitive behavior. The Charge storage mechanism, involving lithium-ion intercalation T-Nb_2O_5, can be represented by the following reaction [26]:

$$Nb_2O_5 + xLi^+ + xe^- \leftrightarrow Li_xNb_2O_5$$

The increase in current with corresponding increases in scan rates in the CV profiles suggests the capacitive nature of the T-Nb_2O_5 electrode. Furthermore, the CD profile of the T-Nb_2O_5 electrode at various applied currents (1 to 5 mA) is provided in **Figure 2b**. The CD profiles indicate the distinct plateau regions in the discharge curves, which again demonstrate the pseudocapacitive nature of the T-Nb_2O_5 electrode [27]. In the CD profile, the intermediate resistance (IR) drop arises primarily from the Internal resistance within the active electrode material, along with contact resistance at the electrode-electrolyte interface. Notably, the observed IR drop gradually decreases as the current is reduced [28,29]. As shown in **Figure 2b**, the measured IR drop for the T-Nb_2O_5-based electrode at a constant current of 3 mA is approximately 0.08 V. The scan rate versus the specific capacitance curve of the T-Nb_2O_5 electrode is provided in **Figure 2c**. It showed that the specific capacitance of the T-Nb_2O_5 electrode is increased from 14 to 23 F g^{-1} with a decrease in scan rate from 100 to 5 mV s^{-1}. The Electrochemical impedance spectroscopy (EIS) measurements were conducted for the T-Nb_2O_5 electrode over a frequency range of

0.1 Hz to 100 kHz to investigate its charge transfer behavior, as illustrated in **Figure 2d**. The enlarged view of the Nyquist plot reveals an equivalent series resistance (ESR) of approximately 0.5 Ω, with no noticeable charge transfer resistance, indicating the excellent electrical conductivity of the T-Nb_2O_5 electrode.

To further evaluate the electrode composed of T-Nb_2O_5 nanoparticles, a symmetric supercapacitor device (SSD) was fabricated, employing T-Nb_2O_5 electrodes as both the positive and negative electrodes. **Figure 3a** presents the CV profile of the T-Nb_2O_5-based SSD, demonstrating its operation within a potential range of 0.0 to 1.0 V. Furthermore, in the CV profile, no noticeable distortion is observed as the scan rates increase, indicating the rapid intercalation reaction of the T-Nb_2O_5 electrode. The CD tests for the T-Nb_2O_5-based SSD, conducted at various applied currents, are displayed in **Figure 3b**. The CD profile of T-Nb_2O_5-based SSD exhibits a quasi-rectangular behaviour, which aligns well with the CV results.

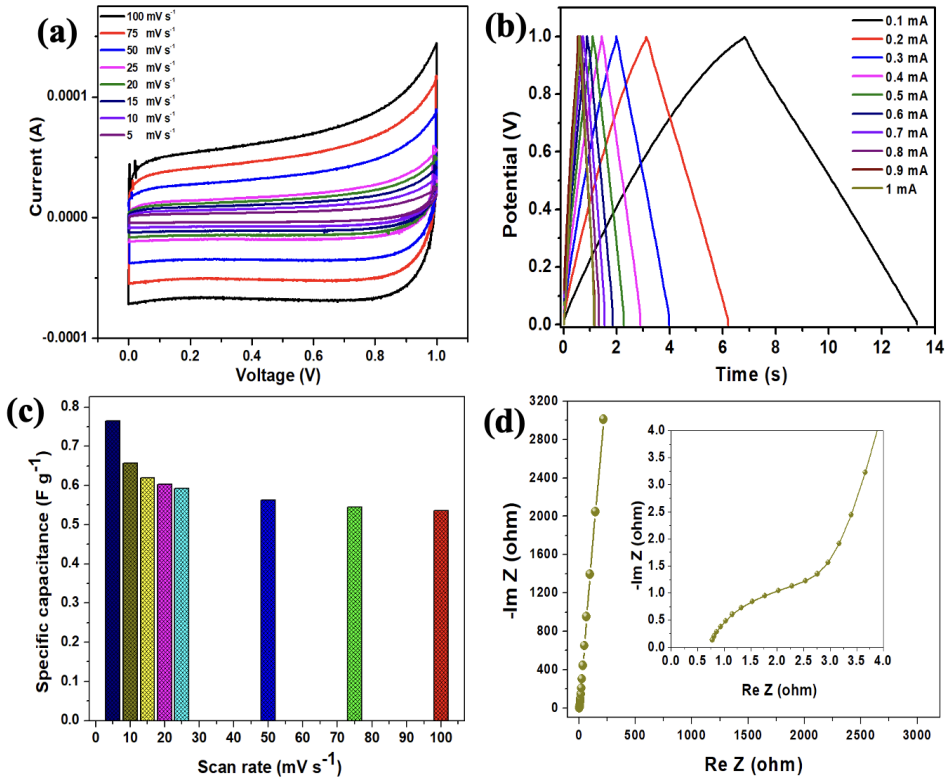

Figure 3. Electrochemical characterization of T-Nb_2O_5 in an SSD system. **(a)** CV profile of T-Nb_2O_5-based SSD at various scan rates (5–100 mV s^{-1}); **(b)** charge-discharge-profile of T-Nb_2O_5 based SSD at various applied currents (0.1–1 mA); **(c)** effect of scan rates on specific Capacitance of T-Nb_2O_5 based SSD; and **(d)** the Nyquist plot T-Nb_2O_5 based SSD with inset shows the enlarged view.

Figure 3c illustrates the relationship between specific capacitance and scan rate for the T-Nb_2O_5-based SSD, which achieved a specific capacitance of approximately 0.76 F g^{-1} at a scan rate of 5 mV s^{-1}. The cyclic stability test of the fabricated T-Nb_2O_5-based SSD over 3000 cycles at an applied constant current of 0.5 mA, as illustrated in **Figure S1** (in supporting information). The T-Nb_2O_5-based SSD demonstrated a capacitance retention of approximately 84.23%, with a calculated

coulombic efficiency of around 91% over continuous 3000 cycles. The Nyquist plot for T-Nb_2O_5-based SSD is represented in **Figure 3d**. The Nyquist plots for T-Nb_2O_5-based SSD displayed three distinguishing regions: (i) low-frequency, (ii) intermediate-frequency, and (iii) high-frequency. These regions allowed for determining key parameters such as the knee frequency, Warburg line, an equivalent series resistance (ESR) of the devices [30]. The T-Nb_2O_5-based SSD obtained a solution resistance (Rs) of about 0.7 Ω and charge transfer resistance (Rct) of about 2.3 Ω.The fitted Randles circuit of the Nyquist plot is provided in **Figure S2** (in supporting information). Further, the EIS measurements of the T-Nb_2O_5-based SSD before and after the cyclic stability test, are illustrated in **Figure S3** (in Supporting information). The Nyquist plots indicate a change in solution resistance (Rs) from 0.7 Ω to 0.9 Ω and an increase in charge transfer resistance (Rct) from 2.3 Ω to 3 Ω after the cyclic stability test over 3000 cycles.

4. Conclusions

In summary, a simple and efficient technique was employed to synthesize orthorhombic-phase niobium oxide (T-Nb_2O_5).

The synthesized T-Nb_2O_5 was then characterized utilizing a range of physical techniques, including XRD, SEM, and EDS.

Additionally, the supercapacitive performance of the T-Nb_2O_5 electrode was evaluated using both a half-cell system and a symmetric supercapacitor device.

The T-Nb_2O_5 electrode demonstrated a gravimetric capacitance of approximately 23 F g^{-1} at a scan rate of 5 mV s^{-1}, along with excellent rate capability.

These findings highlight the potential of T-Nb_2O_5 nanoparticles for future generation energy storage systems.

Supplementary materials: The supplementary material includes the cyclic stability test, the fitted Randles circuit, and Nyquist plots (both before and after the cyclic stability test) for T-Nb_2O_5-based SSD**.**

Author contributions: Conceptualization, SS; methodology, SS; writing the original draft, SS; analysis of results, AKG; funding acquisition, VKP; project administration, VKP. All authors have read and agreed to the published version of the manuscript.

Acknowledgments: The authors would like to extend their gratitude to the Central Instrumentation Facility (CIF) and the Multiscale Manufacturing and Engineering (MSME) Lab at the Indian Institute of Technology Jammu for providing access to experimental and characterization facilities. Surjit Sahoo acknowledges the Department of Science and Technology (DST), New Delhi, India, for the DST-INSPIRE Faculty Award [DST/INSPIRE/04/2023/000200].

Conflict of interest: The authors declare no conflict of interest.

References

1. Sahoo S, Natraj V, Swaminathan R, et al. High-Performance Piezoelectric Nanogenerator and Self-Charging Photo Power Cell Using Hexagonal Boron Nitride Nanoflakes and PVDF Composite. Advanced Engineering Materials; 2024.

2. Sahoo S, Chatterjee D, Majumder SB, et al. Comparative study of pure and mixed phase sulfurized-carbon black in battery cathodes for lithium sulfur batteries. Applied Research; 2024.
3. Raihan KMA, Sahoo S, Nagaraja T, et al. Transforming scalable synthesis of graphene aerosol gel material toward highly flexible and wide-temperature tolerant printed micro-supercapacitors. APL Energy. 2024; 2(1). doi: 10.1063/5.0186302
4. Wu Y, Holze R. Battery and/or supercapacitor?—On the merger of two electrochemical storage system families. Energy Storage and Conversion. 2024; 2(1): 491. doi: 10.59400/esc.v2i1.491
5. Xu Z, Meng Z. Research progress on hydroxide fluoride-based electrode materials for supercapacitors. Energy Storage and Conversion. 2023; 1(1): 275. doi: 10.59400/esc.v1i1.275
6. An C, Zhang Y, Guo H, et al. Metal oxide-based supercapacitors: progress and prospectives. Nanoscale Advances. 2019; 1(12): 4644-4658. doi: 10.1039/c9na00543a
7. Wang Q, Jiang X, Tong Q, et al. Continuously Interconnected N-Doped Porous Carbon for High-Performance Lithium-Ion Capacitors. Nanoenergy Advances. 2022; 2(4): 303-315. doi: 10.3390/nanoenergyadv2040016
8. Li Y, Wang H, Wang L, et al. Mesopore-Induced Ultrafast Na+-Storage in T-Nb_2O_5/Carbon Nanofiber Films toward Flexible High-Power Na-Ion Capacitors. Small. 2019; 15(9). doi: 10.1002/smll.201804539
9. Mohammadifar M, Massoudi A, Naderi N, et al. Pseudocapacitive Behavior of Nb_2O_5-TNTs Nanocomposite for Lithium-ion Micro-batteries. ACERP; 2021.
10. Arico C, Ouendi S, Taberna PL, et al. Fast Electrochemical Storage Process in Sputtered Nb_2O_5 Porous Thin Films. ACS Nano. 2019; 13(5): 5826-5832. doi: 10.1021/acsnano.9b01457
11. Abdulkadir BA, Dennis JO, Adam AA, et al. Novel electrospun separator-electrolyte based on PVA-K_2CO_3-SiO_2-cellulose nanofiber for application in flexible energy storage devices. Journal of Applied Polymer Science. 2022; 139(23). doi: 10.1002/app.52308
12. Amate RU, Morankar PJ, Chavan GT, et al. Bi-functional electrochromic supercapacitor based on hydrothermal-grown 3D Nb_2O_5 nanospheres. Electrochimica Acta. 2023; 459: 142522. doi: 10.1016/j.electacta.2023.142522
13. Lim E, Jo C, Kim H, et al. Facile Synthesis of Nb2O5@Carbon Core–Shell Nanocrystals with Controlled Crystalline Structure for High-Power Anodes in Hybrid Supercapacitors. ACS Nano. 2015; 9(7): 7497-7505. doi: 10.1021/acsnano.5b02601
14. Lian Y, Wang D, Hou S, et al. Construction of T-Nb_2O_5 nanoparticles on/in N-doped carbon hollow tubes for Li-ion hybrid supercapacitors. Electrochimica Acta. 2020; 330: 135204. doi: 10.1016/j.electacta.2019.135204
15. Theodore AM. Promising cathode materials for rechargeable lithium-ion batteries: a review. International Journal of Sustainable Energy and Environmental Research. 2023; 14(1): 51-58. doi: 10.0909/JSE.2023660090
16. Nagaraju P, Vasudevan R, Alsalme A, et al. Surfactant-Free Synthesis of Nb_2O_5 Nanoparticles Anchored Graphene Nanocomposites with Enhanced Electrochemical Performance for Supercapacitor Electrodes. Nanomaterials. 2020; 10(1): 160. doi: 10.3390/nano10010160
17. Li Y, Wang R, Zheng W, et al. Design of Nb_2O_5/graphene hybrid aerogel as polymer binder-free electrodes for lithium-ion capacitors. Materials Technology. 2020; 35(9-10): 625-634. doi: 10.1080/10667857.2020.1734720
18. Kamaraj P, Vennila R, Sridharan M, Vivekanand PA. Super Capacitance of Metal Oxide Nanoparticles. Cham: Springer International Publishing; 2021. pp. 1759-1771.
19. Vicentini R, Soares DM, Nunes W, et al. Core-niobium pentoxide carbon-shell nanoparticles decorating multiwalled carbon nanotubes as electrode for electrochemical capacitors. Journal of Power Sources. 2019; 434: 226737. doi: 10.1016/j.jpowsour.2019.226737
20. Kong L, Zhang C, Wang J, et al. Free-Standing T-Nb_2O_5/Graphene Composite Papers with Ultrahigh Gravimetric/Volumetric Capacitance for Li-Ion Intercalation Pseudocapacitor. ACS Nano. 2015; 9(11): 11200-11208. doi: 10.1021/acsnano.5b04737
21. Jiang S, Dong S, Wu L, et al. Pseudocapacitive T-Nb_2O_5/N-doped carbon nanosheets anode enable high performance lithium-ion capacitors. Journal of Electroanalytical Chemistry. 2019; 842: 82-88. doi: 10.1016/j.jelechem.2019.04.042
22. Zhang S, Wu J, Wang J, et al. Constructing T-Nb_2O_5@Carbon hollow core-shell nanostructures for high-rate hybrid supercapacitor. Journal of Power Sources. 2018; 396: 88-94. doi: 10.1016/j.jpowsour.2018.06.007

23. Meng X, Guan Z, Zhao J, et al. Lithium-pre-intercalated T-Nb_2O_5/graphene composite promoting pseudocapacitive performance for ultralong lifespan capacitors. Chemical Engineering Journal. 2022; 438: 135492. doi: 10.1016/j.cej.2022.135492
24. Yang H, Xu H, Wang L, et al. Microwave-Assisted Rapid Synthesis of Self-Assembled T-Nb_2O_5 Nanowires for High-Energy Hybrid Supercapacitors. Chemistry – A European Journal. 2017; 23(17): 4203-4209. doi: 10.1002/chem.201700010
25. Jiao X, Hao Q, Liu P, et al. Facile synthesis of T-Nb_2O_5 nanosheets/nitrogen and sulfur co-doped graphene for high performance lithium-ion hybrid supercapacitors. Science China Materials. 2017; 61(2): 273-284. doi: 10.1007/s40843-017-9064-6
26. Augustyn V, Come J, Lowe MA, et al. High-rate electrochemical energy storage through Li^+ intercalation pseudocapacitance. Nature Materials. 2013; 12(6): 518-522. doi: 10.1038/nmat3601
27. Yu Y, Jin Y, Hasan N, et al. Tuning the interface interaction between Nb2O5 nanosheets/graphene for high current rate and long cyclic lithium-ion batteries. Electrochimica Acta. 2022; 435: 141397. doi: 10.1016/j.electacta.2022.141397
28. Wang K, Wu H, Meng Y, et al. Integrated energy storage and electrochromic function in one flexible device: an energy storage smart window. Energy & Environmental Science. 2012; 5(8): 8384. doi: 10.1039/c2ee21643d
29. Sahoo S, Pazhamalai P, Krishnamoorthy K, et al. Hydrothermally prepared α-MnSe nanoparticles as a new pseudocapacitive electrode material for supercapacitor. Electrochimica Acta. 2018; 268: 403-410. doi: 10.1016/j.electacta.2018.02.116
30. Deshmukh AD, Urade AR, Nanwani AP, et al. Two-Dimensional Double Hydroxide Nanoarchitecture with High Areal and Volumetric Capacitance. ACS Omega. 2018; 3(7): 7204-7213. doi: 10.1021/acsomega.8b00596

Energy Storage and Conversion 2024, 2(4), 1631.
https://doi.org/10.59400/esc1631

Review

Constructing polyolefin-based lithium-ion battery separators membrane for energy storage and conversion

Lei Li[1,2], Fanmin Kong[1], Ang Xiao[1], Hao Su[1], Xiaolian Wu[1], Ziling Zhang[1], Haoqi Wang[1], Yutian Duan[1,3,*]

[1] SINOPEC Nanjing Research Institute of Chemical Industry Co., Ltd., Nanjing 210048, China
[2] Hefei National Laboratory for Physical Sciences at the Microscale, Department of Polymer Science and Engineering, School of Chemistry and Materials Science, University of Science and Technology of China, Hefei 230026, China
[3] College of Material Science and Engineering, Donghua University, Shanghai 201620, China
*** Corresponding author:** Yutian Duan, duanyt9402.nhgs@sinopec.com

CITATION

Li L. Kong F, Xiao A, et al. Constructing polyolefin-based lithium-ion battery separators membrane for energy storage and conversion. Energy Storage and Conversion. 2024; 2(4): 1631. https://doi.org/10.59400/esc1631

ARTICLE INFO

Received: 20 August 2024
Accepted: 13 September 2024
Available online: 13 November 2024

Abstract: Owing to the escalating demand for environmentally friendly commodities, lithium-ion batteries (LIBs) are gaining extensive recognition as a viable means of energy storage and conversion. LIBs comprise cathode and anode electrodes, electrolytes, and separators. Notably, the separator, a crucial and indispensable element in LIBs that mainly comprises a porous membrane material, necessitates substantial research focus. Scholars have consequently strived to devise novel systems that augment separator efficiency, bolster safety measures, and surmount existing constraints. This review endeavors to equip researchers with comprehensive information on polyolefin-based separator membranes, encompassing performance prerequisites, functional attributes, scientific advancements, and so on. Specifically, it scrutinizes the latest innovations in porous membrane configuration, fabrication, and enhancement that utilize the most prevalent polyolefin materials today. Consequently, robust and enduring membranes fabricated have demonstrated superior effectiveness across diverse applications, facilitating a circular economy that curbs waste materials, reduces operational expenses, and mitigates environmental impact.

Keywords: lithium-ion battery; separator membrane; energy storage and conversion; polyethylene; polypropylene

1. Introduction

LIBs are recognized globally as being among the most viable and potent energy storage and conversion technologies currently accessible, featuring prominently across sectors including mobile devices, electric vehicles (EVs), and energy storage systems [1,2]. In light of the escalating global demand for renewable energy and sustainable progression, the societal and economic importance of LIBs is progressively gaining traction [3–6]. Owing to their exceptional energy density, extended life span, broad operating temperature range, and superior battery voltage, LIBs have ascended as the preeminent candidate in the domain of energy storage cells, offering significant benefits across various sectors like aerospace, artificial satellites, reliable power supply for military and civilian electronic equipment [7]. Consequently, the potential applications of LIBs indicate considerable promise, calling for an enhanced focus on LIB performance, specifically addressing measures related to electrochemical efficiency (such as energy density) and security [3,8].

LIBs primarily comprise positive (cathode) and negative (anode) electrodes [9,10], electrolytes and separators [11]. Within this assembly, the separator, principally comprising a porous membrane material, holds an essential and pivotal

role within LIBs. This permeable membrane accommodates electrolytes and is incorporated between the battery's cathode and anode electrodes, serving as a significant component within LIB separators [12,13]. During the operation of LIBs, lithium ions (Li^+) navigate between cathode and anode electrodes via the separator, facilitating electrical conductivity [14]. Taking the typical lithium iron phosphate ($LiFePO_4$) battery as an example, during charging, the positive electrode (cathode) material releases Li^+, which transport towards the negative electrode (anode) through the separator membrane. Meanwhile, electrons will flow from the positive electrode to the negative electrode via an external circuit, and the opposite will occur during discharging (**Figure 1**). Significantly, the fundamental performance attributes of the membrane encompass thickness, mechanical resilience, porosity, wettability, thermal contraction, electrochemical stability, among others [15–17]. Hence, judicious material choice and meticulous structural design of separators dictate these performance characteristics and play a pivotal role in guaranteeing the secure operation and enduring charge/discharge cycles of LIBs.

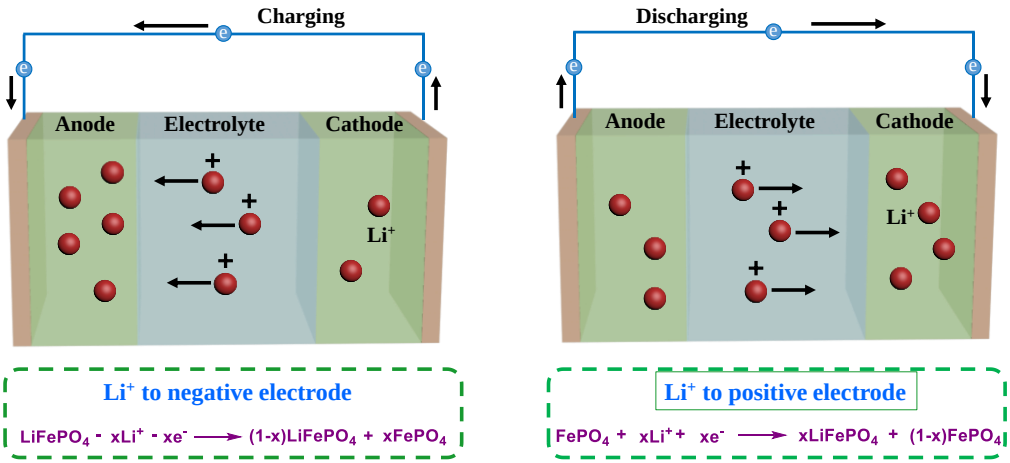

Figure 1. Schematic illustration of the fundamental operating mechanism of a typical LIB and equations of Li^+ transport for negative and positive electrodes of a typical $LiFePO_4$ battery.

Polyolefin microporous membranes, predominantly fabricated from polyethylene (PE), polypropylene (PP), and their blends, have become the predominant separator in the secondary rechargeable battery sector. Notably, ultra-high molecular weight polyethylene (UHMWPE) has gained substantial market share, polymerized with Ziegler–Natta catalysts at low pressure via a procedure described in research [18]. Such affordable membranes, suitable for mass commercialization, are, however, restricted by inherent poor thermal stability (low Tm) and flammability, along with potentially subpar electrolyte wetting properties [7,19]. Compared to other materials, polyolefin is often utilized for its exceptional features in commercial LIBs, albeit its inherent thermal shrinkage issue and inadequate electrolyte wettability, etc. Consequently, the exploration of enhanced polyolefin membranes remains a fervent area of research, with noteworthy advancements being achieved at an accelerated pace.

Significantly, the application of sustainable electrochemical energy storage and conversion apparatuses exhibits extensive advantages in fostering a circular and eco-friendly economic system [1,10,13,20,21]. Positioned as an economically viable

strategy for clean power, the primary goal of LIB separators is to devise and fabricate novel membranes for superior battery performance [22]. This review underscores the importance of polyolefin-based porous membranes for separators in LIBs, encompassing the essential prerequisites and performance metrics for optimal separators, incorporating the chemical, mechanical, electrical, and electrochemical attributes of porous separator membranes for batteries. Furthermore, this review scrutinizes contemporary breakthroughs in the fabrication, configuration, alteration, and enhancement of porous membranes, utilizing polyolefin materials. Collectively, the advancement of robust, proficient, and pioneering LIB separators serves a critical function in actualizing the principles of a circular economy, along with the overarching goals of resource optimization and environmental sustainability [23].

2. Performance parameters and characteristic of LIB separators membranes

Arranged between the cathode and the anode, the LIB separator is pivotal in thwarting potential shorts circuits due to direct interaction between the cathode and the anode active components, concurrently facilitating swift Li^+ transportation during charging and discharging procedures [24–28]. The separator serves as a pivotal component within LIBs, crucial in optimizing battery functionality and safety across diverse application environments. A multitude of technologies and methodologies are thus enlisted to evaluate membrane performance, encompassing parameters such as membrane thickness [29,30], tensile strength [31,32], puncture resistance [33], thermal stability, porosity [7], pore size [34], electrolyte wettability, chemical stability, electrolyte absorption and retention rate, dimensional stability [35], air permeability [36], electrochemical performance [37] and so on (**Figure 2**). Given their deployment in extensive equipment platforms like EVs or energy storage facilities, LIBs separator membranes necessitate superior mechanical strength, capacity, thermal stability, rate capability, excellent electrochemical performance and prolonged cycle performance [38]. Consequently, an ideal separator must satisfy specific critical physical and chemical attributes (**Figure 3**).

Given that the separator material is a non-conductive agent tasked with safeguarding electrodes indispensable for establishing ion transfer channels amid intricate electrochemical mechanisms, its intrinsic physical and chemical traits significantly influence battery functionality. Typically, the employment of a thinner and more permeable separator leads to diminished internal resistance, which subsequently increases discharge capacity [39,40]. Yet, elevated porosity and reduced thickness may compromise the separator's structural resilience, underscoring the necessity for materials that strike an equilibrium between electrochemical and mechanical properties for enhancing overall battery efficiency [36,41].

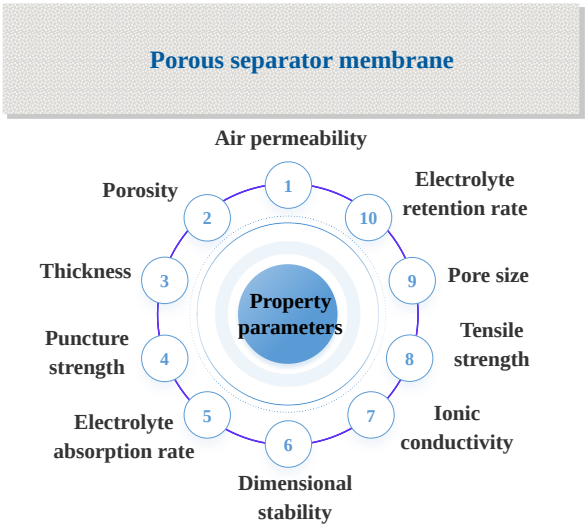

Figure 2. Illustration demonstrating the property parameters to be taken into account when devising suitable separator membranes for rechargeable LIBs.

Significantly, lithium dendrites can develop during extended charging/discharging cycles, representing the predominant and potentially catastrophic sources of internal shorts within LIBs [42]. A thicker separator offers enhanced mechanical resilience, diminishing the likelihood of short circuits during assembly. Typically, separators utilized for LIBs possess a thickness of less than 25 μm [43]. Herein, attaining a specific degree of mechanical robustness with adequate puncture and tensile strength is crucial, and this can be achieved through the utilization of a thinner separator with elevated porosity, thereby decreasing the internal impedance of the battery and enhancing high-speed discharge capabilities [32].

In addition, LIBs inevitably generate considerable heat during charging/discharging, particularly under short circuit or excessive charging. The role of the separator is paramount for maintaining exceptional dimensional stability and robust mechanical resilience across the temperature spectrum spanning from −20 °C to 90 °C [29]. Presently, there exist two predominant coating methodologies employed to enhance LIBs thermal endurance, namely inorganic coatings and organic coatings [44–46]. Specifically, the inorganic ceramic layers comprise inorganic particles and binders, encompassing but not confined to aluminum oxide (Al_2O_3), boehmite, zirconium dioxide (ZrO_2), etc. Conversely, organic coating, also referred to as organic composite modification, involves the application of an organic compound (such as polyvinylidene fluoride (PVDF), polyacrylonitrile (PAN), polymethyl methacrylate (PMMA), polydopamine (PDA), aramid, polyimide (PI) and their blends) onto the surface of the separator membrane, demonstrating outstanding liquid absorption and retention capacities, coupled with superior adhesion characteristics [7].

Besides, thermal shutdown constitutes an integral role in the separator's effectiveness, culminating in the sealing of the micropores when the battery encounters a short circuit and the temperature deviates outside its specified operational limits, thereby preventing uninterrupted ion passage and averting thermal runaway [30]. This shutdown mechanism ensues from a blend of two materials possessing varying melting temperatures (T_m). The safety window temperature denotes the difference in T_m

between these constituents [47]. Furthermore, the inclusion of a less thermally resilient material confers higher sensitivity to temperature fluctuations, wider safety windows, and enhanced overall security functionality on the membrane [29].

Moreover, membrane materials are required to optimize ion transport, establish unimpeded and spacious channels for Li^+ passage, and operate as an electron insulator to ensure insulation between the anode and cathode. The permeation property of the separator is an essential trait that can be numerically analyzed by the MacMullin number and Gurley value [48]. Furthermore, uniform permeation is vital for attaining extended cycle longevity, promoting efficient Li^+ transportation throughout charging and discharging processes, implying the necessity for sufficient porosity [49], with commercially prevalent separator pores typically measuring less than 1 μm. Concurrently, to augment safety during operation, it is often advisable that porosity remains below approximately 50%.

Notably, the chemical durability of a separator denotes its capacity to withstand chemical reactions with electrolytes and electrodes [50]. In order to meet the requirements of various LIBs exposed to organic solvents, polyolefin-based separators with increased strength are frequently used [51,52]. Incorporating inorganic nanomaterials such as Al_2O_3, SiO_2, TiO_2, ZrO_2, among others, into these separators can further enrich their stability and robustness [30]. The Li||$LiFePO_4$ cell using UHMWPE separator membrane complexed with SiO_2 displayed significant discharge capacities of 165 mAh g^{-1} at 0.1 C-rate and 123 mAh g^{-1} at 5 C-rate, coupled with excellent cycling performance exceeding 100 cycles [51]. Meanwhile, a TiO_2-grafted PE separator not only demonstrated significantly enhanced stability even at 150 ℃, but also superior electrochemical performance compared to bare PE separators [52]. Similarly, a ZrO_2-modified PE separator showed outstanding cyclic performance, retaining 96.2% of initial capacity after 50 cycles, and enhanced stability even under 200 ℃ conditions [53]. Notably, modified LIB separators mainly include inorganic coating, organic coating, and mixed/composite coating, depending on the coating material. In the contemporary industry, modified LIB separators with inorganic coatings are the prevailing coating separator materials, such as boehmite and Al_2O_3, which are the predominant inorganic coating materials. Inorganic coating materials can enhance the thermal stability of membranes, diminish thermal shrinkage, bolster puncture resistance, and enhance self-discharge. Nevertheless, it is pertinent to note that the application of inorganic coating modified LIBs separators may induce pore blockage, thereby impacting the ion conductivity and the lifespan of the battery.

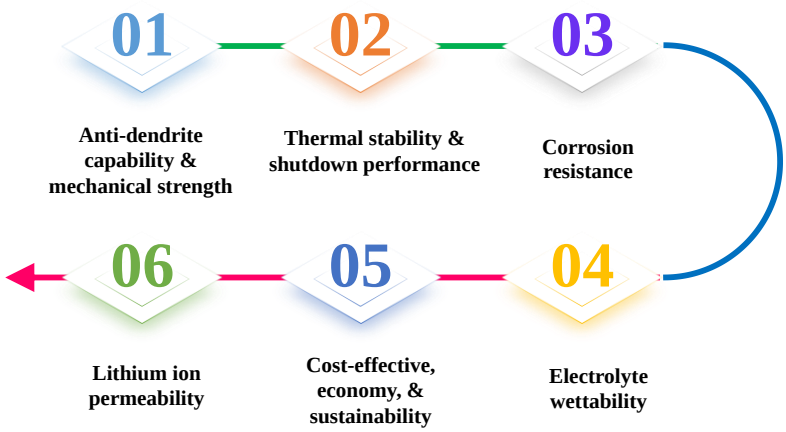

Figure 3. Detailed representation of separator performance prerequisites to contemplate when design the suitable separator for rechargeable LIBs.

Additionally, if the electrolyte can rapidly and comprehensively permeate the separator, the intrinsic impedance of LIBs can be significantly reduced, thereby enhancing ionic conductivity and charge and discharge capability [54]. Inadequate wettability increases separator resistance, affecting cycling performance and charging/discharging proficiency [55,56]. Therefore, it becomes imperative to alter the surface of the membranes to render them more hydrophilic. It should be underscored that hydrophilic functionalities can be grafted onto membrane surfaces through thermal spraying by judicious selection of suitable gases, culminating in enhanced durability, encompassing carbonyl, hydroxyl, carboxyl, sulfonyl and amino groups [57].

3. Recent advances in polyolefin-based porous separator membranes

Presently, LIB separators available on the market are predominantly microporous polyolefin membranes represented by PE, PP, and others. Research progress related to LIB separators has been extensively reported, yet primarily concentrated on the modification of polyolefin separators. This article aims to provide a comprehensive overview of recent breakthroughs in polyolefin-based porous separator membranes in the LIB field (**Table 1**).

Table 1. Summary of polyolefin-based separator membranes discussed in this review.

Substrate Material	Additives	Preparation methods	Thickness (μm)	Porosity (%)	Thermal Shrinkage (%)	Electrolyte Uptake (%)	Ionic Conductivity (mS cm^{-1})	Battery Performance	Ref.
PP	ZIF-67–CH_3OH	wet method	30	52.53	3.33% at 120 ℃ for 0.5 h	142	0.78	86.9%·after 100 cycles at 1 C under 25 ℃; 61.5%·after 100 cycles at 1 C under 55 ℃	[58]

Table 1. (*Continued*).

Substrate Material	Additives	Preparation methods	Thickness (μm)	Porosity (%)	Thermal Shrinkage (%)	Electrolyte Uptake (%)	Ionic Conductivity (mS cm^{-1})	Battery Performance	Ref.
PP	SiO_2–TEOS	wet method	25.6		4.6% at 150 ℃ for 0.5 h		0.16	140 mAh g^{-1} at 0.2 C; 96.14%·after 65 cycles at 0.2 C	[59]
PP	SiO_2	wet method	18	42		113.7	0.80 (PP-5); 0.82 (PP-12)	67.2 mAh g^{-1} at 7 C; 87% after 200 cycles at 0.5C	[60]
PP	PAAB–Li	wet method	24	61.8		195.8	0.96	119.4 mAh g^{-1} at 1 C; 78.0% after 250·cycles at 1 C	[61]
PP	PI	wet method	24	54.78	0% at 150 ℃ for 0.5 h	207.62	0.35	144.3 mAh g^{-1} at 5 C; 80.1%·after 200 cycles at 1 C	[62]
PP	BTCEAD	wet method		38.2 ± 1.30 (8% GD); 32.7 ± 2.24 (18% GD); 24.3 ± 1.49 (31% GD)		144 ± 5.9 (8% GD); 212 ± 4.5 (18% GD); 292 ± 9.4 (31% GD)	0.56 (8% GD); 0.51 (18% GD) 0.37 (31% GD)	84.59%·after 175 cycles at 0.5 C (8% GD); 97.97%·after 175 cycles at 0.5 C (18% GD)	[63]
PP	sepiolite/PVDF	wet method	32	62%	0% at 140 ℃ for 0.5 h	653	0.98 mS·cm^{-1}	115.3 mAh·g^{-1} at 10C rate; 97.06% after 200 cycles at 1C rate	[64]
PP/PAN/cotton		wet method		63	<4% at 160 ℃ for 1 h	269	1.99	166.7 mAh g^{-1} at 1 C; 93.8%·after 100 cycles at 1 C	[65]
PP/PE		dry method	25	54.6	0% at 160 ℃ for 0.5 h	157	1.46	98% (coulombic efficiency) after 30 cycles at 0.2 C	[66]
PE	γ-AlOOH	wet method	26	55.63	0% at 170 ℃ for 0.5 h	187	1.00	75.1% (95.1 mAh g^{-1}) after 200 cycles at 1 C	[67]
PE	SiO_2–PZS	wet method	20.4 ± 1.2			155.2 ± 14.3	1.04	115 mAh g^{-1} at 8 C;	[68]
PE	alumina or boehmite	wet method	12			308 (W-PE-A); 335 (W-PE-B)	1.04 (W-PE-A); 1.81 (W-PE-B)	higher than 80 mAh/g after 200 cycles at 4C	[69]
PE	poly-aromatic solid electrolyte	wet method	12–13	47.2	4.09% at 115 ℃ for 1 h; 42.54% at 145 ℃ for 1 h	126.4	0.36	84.01% (151.25 mAh g^{-1}) after 200 cycles at 2 C	[70]

Table 1. (*Continued*).

Substrate Material	Additives	Preparation methods	Thickness (μm)	Porosity (%)	Thermal Shrinkage (%)	Electrolyte Uptake (%)	Ionic Conductivity (mS cm^{-1})	Battery Performance	Ref.
PE	PAI	wet method	14.5–15.0	35–55	1.7% (MD) and 1.1% (TD) at 130 ℃ for 0.5 h			98.8–99.5% after 10 cycles at 0 ℃	[71]
PE	hydroxyapatite	wet method	23.4	30–50	2456.4 ± 280.5% at 180 ℃		0.03	100% (150 mAh g^{-1}) after 200 cycles at 1 C	[72]
PE	BPO	wet method				85	0.89	98.1% after 70 cycles	[73]
PE	MA	wet method	16				0.306	>135 cycles at 1.5 mA cm^{-2} (1 C)	[74]
PE	PVDF	wet method	20	64	0% at 500 ℃		1.77	73% after 250 cycles	[75]
PE	HDPE wax/γ-AlOOH	wet method	10	44.0					[76]
PE	Al_2O_3, LDPE	wet method	18		1% at 185 ℃	407.23	0.39	98.9% (144.5 mAh g^{-1}) after 900 cycles	[77]
PE	CA–PEO–LPSQ	wet method	26 ± 1.5		9% at 120 ℃ for 1 h	185	5.79	82% after 300 cycles at 0.5 C	[78]
UHMWPE	PMP	wet method		65.4 ± 1.1	0.7% (MD) and 1.6% (TD) at 120 ℃ for 1 h	259.7%	1.17	172.8 mAh g^{-1} at 0.1 C; 99.89% after 100·cycles at 1 C	[79]
UHMWPE		wet method	2	78.3.					[80]
UHMWPE	liquid paraffin	wet and dry method	5; 12	30; 94					[81]
UHMWPE	nano-Al_2O_3	wet method	15.3	44.2	14.3% at 120 ℃ and 34.5% at 130 ℃ for 0.5 h	129.8	0.94	139.4 mAh g^{-1} at 0.2 C; 89.4% after 200·cycles at 1 C	[82]

3.1. PP Separator membranes

PP is often used as a LIB separator due to its robust chemical stability, thickness, and strength. Nevertheless, excessive thermal shrinkage at elevated temperatures could potentially trigger internal short circuits, escalating safety risks like fire or explosion [35]. Given the potential hazards of short circuits leading to combustion/detonation, researchers concentrated on mitigating the detrimental effects of thermal shrinkage on commercial PP separators through membrane surface alteration. Notably, inorganic coating is crucial for improving the overall performance of LIB separators, and is currently an important method in the battery separator manufacturing industry. Chen et al. [58] innovatively designed an organic-inorganic separator by directly adhering zeolitic imidazolate framework (ZIF)-67 particles onto PP separator surfaces. Two distinct ZIF-67 variants were synthesized: ZIF-67–hydrogen oxide (H_2O) and ZIF-67–methanol (CH3OH) using H_2O and CH_3OH as solvents, respectively. Notably, ZIF-67–CH_3OH demonstrated superior cell capacity

retention (61.5%) post 100 cycles at elevated 55 ℃, outperforming the uncoated PP separator (0.0%). Similarly, Zhao et al. [59] enhanced Celgard-2300 separators via surface chemical treatment with SiO_2-tetraethylorthosilicate (TEOS). Remarkably, the untreated separator displayed 38.6% shrinkage in the MD direction at 150 ℃ for 30 min compared to merely 4.6% contraction after modifications. Ding et al. [60] engineered a fumed SiO_2/*β*-iPP blend with PP, silica, and *β*-nucleating agent (*β*-iPP) coupled with complex bi-directional stretching methods to shape the pores' structure, achieving in-situ SiO_2 coating. This membrane revealed a precise microporous pattern with a 5% SiO_2 content, delivering enhanced discharge capacity at elevated current densities (67.2 mAh g−1 at 7 C). Remarkably, it ensured 87% capacity preservation beyond 200 cycles, outperforming non-SiO_2 PP membranes (i.e., 70.2% retention post 200 cycles). Additionally, Yan et al. [61] utilized PP as the structural framework to produce a novel multifunctional copolymer, i.e., poly (acrylonitrile-co-lithium acrylate-co-butyl acrylate) (PAAB–Li), via soap-free emulsion polymerization. Subsequently, the copolymer was employed to fabricate uniformly coated separators (PAAB–Li-aided PP separators) on PP substrates via a simple dip-annealing process. Cells incorporating these modified separators exhibited stable cycling performance for over 800 h, indicating the functional layer capability to suppress lithium dendrite growth. Notably, Romano et al. [83] pioneered in developing novel ultra-high molecular weight isotactic polypropylene (UHMWiPP) with reduced chain entanglement (disentangled-UHMWiPP), demonstrated its potential as a LIB separator due to its exceptional mechanical strength and thermal stability compared to isotactic PP. This innovative material can be processed via solid-state methods without solvents, resulting in a uni-axial orientation below its Tm. Recently, Hasanpoor et al. [84] refined methods for applying finely ground high purity alumina (HPA) to PP battery mesh. Suspending alumina particles in acetone solvent, along with poly (vinylidene fluoride-co-hexafluoropropylene) (PVDF-HFP), provided sufficient binding strength (**Figure 4**). The influence of alumina particle size, distribution, and calendaring on coating attributes and cell performance was studied using three HPA sources. The doctor blade method yielded an even monolayer with superior mechanical stability and heat stability.

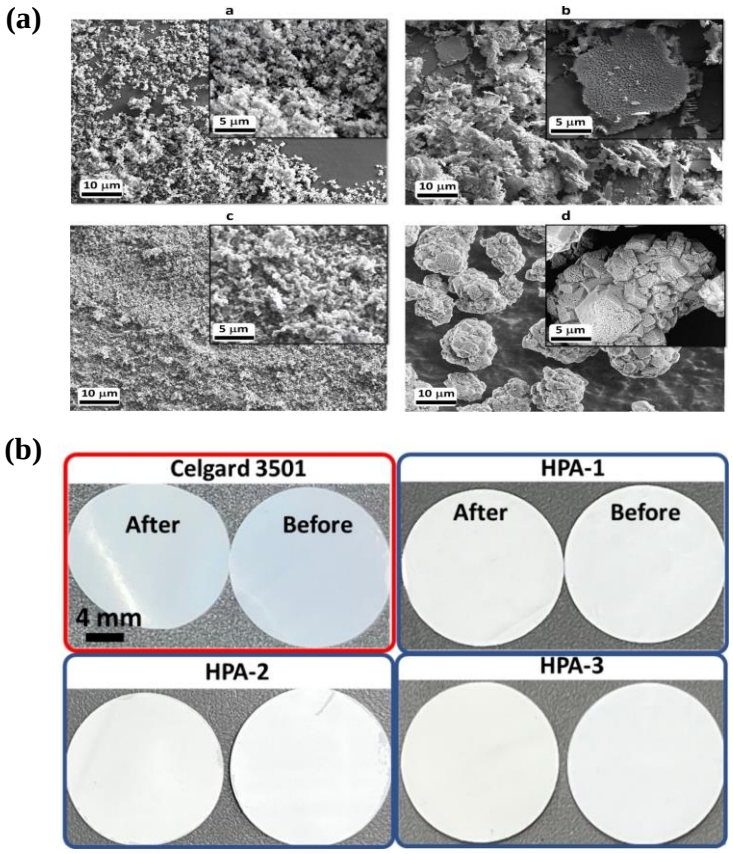

Figure 4. Characterization of HPA and HPA coated Celgard 3501 separator membrane. **(a)** SEM images illustrating the particle size and morphology of a) HPA-1, b) HPA-2, c) HPA-2 milled and d) HPA-3 samples; **(b)** procedure used as a comparative reference for aged Celgard 3501 with no coating, subjected to a temperature of 120 ℃ for an extended duration of 18 h, and in addition, the HPA coated Celgard 3501 adopting multiple particle sizes and morphologies.
Source: Reproduced with permission from [84], copyright John Wiley and Sons, 2024.

Similarly, organic coating or composite is crucial for improving the overall performance of LIB separators, which is currently another popular method for manufacturing battery separators. For instance, Yu et al. [62] showcased an efficacious PP@PI hybrid separator created using a highly porous, thermally stable PI microsphere barrier. The separator demonstrated superior performances like excellent thermal stability (minimal 150 ℃ shrinkage), fire resistance, water absorption, and electrolyte wetting behavior (contact angles of 7° and 5°, respectively). Notably, its ionic conductivity was boosted from 0.26 mS cm^{-1} to 0.35 mS cm^{-1}. Considering the substantial polarity gap between the PP-derived separator and the electrolyte hinder optimization of electrolyte wettability [56], to address this, Chen et al. [63] produced PP(s)-g-poly (ethylene glycol methacrylate) (PPEGMA) membrane, with varied grafting density (GD). Augmentations in PP(s)-g-PPEGMA ionic conductivity observed at 8% and 18% GD reached 0.56 mS cm^{-1} and 0.51 mS cm^{-1}, respectively. Notably, the 18% GD variant exhibited stable cycling for over 180 cycles. Besides, addressing LIBs thermal runaway necessitates novel safety enhancements. Here, Jiang et al. [85] proposed utilizing a thermo-responsive membrane fabricated by grafting poly (N-isopropylacrylamide) (PNIPAM) onto a PDA-modified PP membrane via the

Michael addition reaction. The smart membrane operates based on PNIPAM's upper critical solution temperature (UCST), which serves as the gating temperature, varying determinedly with the ratio of [EMIM][BF_4]. Below this, the gate molecule, grafted on the PP membrane, remains shrunken, facilitating the seamless transport of ions. If, however, due to mishandling, overheating occurs, the gate molecule becomes elongated beyond the gating temperature, effectively sealing off ion passage.

Besides, to promote the mass-production of separators in the LIBs industry, Lee et al. [86] developed a pore-connected PP-cellulose acetate (CA) membrane by coating CA onto a PP membrane. A new method was proposed to attach a CA/glycerin coating layer to a porous PP support without a separate binder. The pores of CA and PP were interconnected using a vacuum filtration device. By adding glycerin to the CA chains, the membrane region became more flexible due to glycerin plasticization. Water passes through the membrane under different pressures, resulting in the formation of interconnected pores between cellulose acetate and PP. The pore size and quantity could be adjusted by varying the molar ratio of glycerin. This simple and cost-effective manufacturing process holds potential for mass-produced separators in the LIBs industry. Sun et al. [64] developed a dual-functionalization of a PP separator utilizing electrospinning coated with a PVDF/sepiolite layer. Post functionalization, the synthesized xMS-PVDF@PP composite separator demonstrated superior porosity, electrolyte absorption, thermo-stability and Li^+ transport kinetics compared to the original PP. Notably, a Li||$LiFePO_4$ cell employing 20MS-PVDF@PP exhibited optimal rate and cycle performance, delivering a specific discharge capacity of 115.3 mAh g^{-1} at 10C and a capacity retention of 97.06% post 200 cycles at 1C. The immobilized sepiolite in the electrospun layer aids in uniform Li^+ distribution, suppresses lithium dendrite formation, and absorbs hydrogen fluoride (HF) to mitigate Fe^{2+} dissolution from the $LiFePO_4$ cathode, thus enhancing the overall electrochemical performance.

Notably, multilayer separator membranes are predominantly utilized in LIBs for their exceptional mechanical robustness and electrochemical sturdiness. For instance, Liu et al. [65] employed a wet-lay technique to incorporate cotton fibers and PAN into PP, yielding a PP/PAN/cotton fiber composite membrane. Given the abundance of polar hydroxyl (−OH) groups on cotton fibers and hydrophilic cyano groups (−CN) on PAN, this enhancement of hydrophilicity was significant. Empirical evidence suggests optimal performance at a cotton fiber content of 50 wt.% with reinforcement of ideal tensile strength (i.e., 1.644 kN m^{-1}), reasonable porosity (i.e., 63%), suitable wettability (aspiration height of 39 mm) and enhanced liquid absorbency (269%). Li et al. [66] successfully integrated multilayer coextrusion (MC) and TIPS methodologies to fabricate PP/PE multilayer separators (termed MC–TIPS PP/PE). Notably, the shrinkage of MC–TIPS PP/PE remained insignificant even at elevated temperatures up to 160 °C. Moreover, these separators exhibited superior porosity (54.6%) and electrolyte wettability (i.e., electrolyte uptake; 157%, electrolyte retention: 141%), leading to increased ionic conductivity (1.46 mS cm^{-1}) and thus superior battery operation. This cost-effective, eco-friendly and efficient methodology offers tremendous potential for the industry alike.

3.2. PE separator membranes

The microporous PE membrane commonly employed as LIB separator, notably exhibits thermal shrinkage and Li dendrite penetration, resulting in critical safety issues like short circuits, thermal runaway, and potential explosions. The researchers' efforts predominantly focus on enhancing PE membrane characteristics via surface modification, i.e., introducing both inorganic and organic layers, to enhance properties including wettability, strength, and thermal and dimensional stability [38]. Noteworthy, incorporating inorganic reinforcements like ZrO_2, Al_2O_3, TiO_2, SiO_2, etc., into the PE matrix mitigates membrane distortion at high temperatures, thereby bolstering LIB safety [33]. For instance, Wang et al. [67] integrated Al_2O_3 and boehmite (γ-AlOOH) as ceramic coating particles with water assistance to produce PE–Al_2O_3 and PE–AlOOH separators. The PE–AlOOH separator's –OH group enhanced its interaction with the coating layer, resulting in improved electrolyte absorption (187%), wettability (5.7° contact angle), and ionic conductivity (1.0 mS cm^{-1}). Additionally, for further optimizing, applying the core–shell design could also enhance PE-based separators' performance, Fu et al. [68] integrated SiO_2 nanoparticles into poly (cyclotriphosphazene-co-4,4'-sulfonyldiphenol) (PZS) to form SiO_2–PZS core–shell particles, subsequently coating these onto both sides of the PE microporous membrane yielding the PE–SiO_2@PZS separator. Hydroxyl and −NO functionalities on PZS nanoparticles synergize with Li^+, enhancing the dissociation of lithium salt ($LiPF_6$), thereby boosting LIBs ionic conductivity and discharge capacity. Qian et al. [69] compared commercial PE separators and alumina/boehmite-fortified versions. When compared against 50 cycles compaction at room temperature, compression at 60 ℃ caused severe damage to PE pore structure, impairing oxidation potential to 3.6 V, with nearly 50% capacity decline in 200 charge-discharge cycles. Vacated by coating, the decorated separator retained its original microstructure, maintaining an oxidation potential exceeding 4.2 V. Yet, despite its insulation, the deposited particles introduced decreased porosity, affecting discharge capacity, particularly at 4C rate. Comparatively, boehmite-covered separators' interface resistance was scarcely impacted, demonstrating superior capability during 60 ℃ cyclic texting, showcasing enhanced practicality.

Incorporation of organic compounds significantly enhances LIB separator performance and functionality. Currently, the utilization of organic layers or composites is an innovative approach to separator fabrication. For example, Ding et al. [70] prepared superior PE separators by applying a polyaromatic solid electrolyte (SPAEK, 60% sulfonated) coating. This layer of SPAEK presents significant enhancements to thermal stability and solvent wettability due to its retarding effect on phase separation. The subsequent polyelectrolyte coating enhanced the composite's electrolyte affinity and electrolyte absorption. Furthermore, this modified separator exhibited enhanced overall properties such as thermal stability and ionic conductivity. Consequently, the battery containing a $LiNi_{0.83}Co_{0.11}Mn_{0.06}O_2$ cathode and PE separator modified by SPAEK exhibited a remarkable capacity retention rate of 84.01%, with a specific capacity of 151.25 mAh g^{-1}, even after 200 cycles at 2 C. Thus, this modified separator holds promise for enhanced LIB performance and safety. For uniform coating, Wang et al. utilized gravure printing to apply pore-regulated

polyamide–imide (PAI) to PE substrates [71]. Heat treatment caused the PE layer to contract, sealing micropores, increasing electrical resistance, and creating an effective electrode barrier. Findings suggested that for pores between 0.17 and 0.85 μm, the electrochemical performance of PAI–PE-2 and PAI–PE-3 remained comparable to that of pure PE membranes.

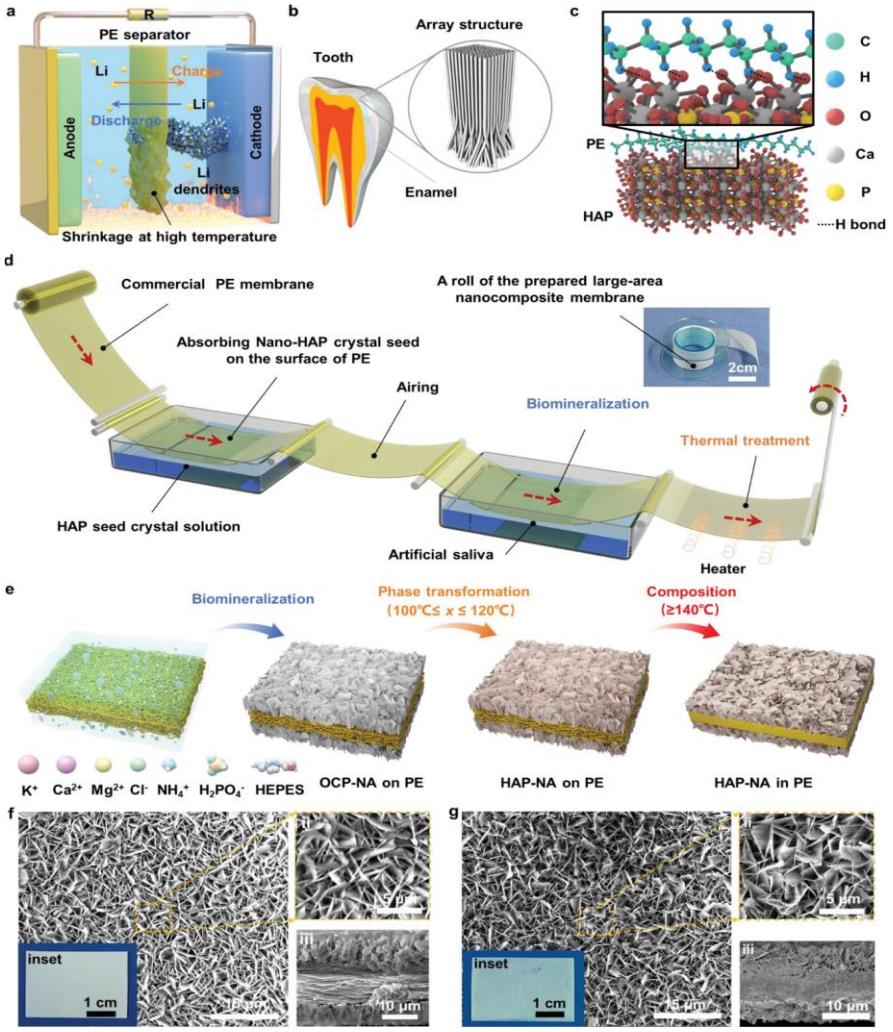

Figure 5. Schematic illustration of the design, fabrication, and microstructural SEM characterization of the enamel-inspired HAP-NA/PE nanocomposite separator membrane.

Source: Reproduced with permission from [72], copyright John Wiley and Sons, 2024.

Additionally, the introduction of organic polar groups through chemical modifications can boost the PE separator's hydrophilicity. Kim et al. [73] treated the PE separator of LIBs with benzoyl peroxide (BPO), introducing carbonyl functional groups to both surfaces. This resulted in a BPO–PE separator exhibiting exceptional rate capacity (86.7% at 3.0 C) and capacity retention over 70 cycles (98.1%), surpassing the pure PE separator's performance under the identical conditions (rate: 78.6%, retention: 91.7%). Moreover, light irradiation has also been harnessed to modify PE-based membranes, Sheng et al. [74] used low-dose γ radiation to activate the PE separator and UV light to graft MA onto it, yielding the PE-g-MA separator with a higher Li^+ transference number (0.49 vs. 0.29) and lower activation energy

(52.1 kJ mol^{-1} vs. 56.5 kJ mol^{-1}). Considering that lithium dendrites at the separator/electrode interface pose a deterrent to advances in LIBs. Here, Chen et. al. [75] enhanced PE separator's interfacial compatibility by coating it with PVDF gel via a facile phase transformation technique. They fabricate a composite separator integrating PE and PVDF. Enhanced interface compatibility emerged after gelation, with polarization onset as minimal as 0.14 V after 250 h of cycling. Interestingly, the addition of F groups in PVDF gel boosted the ionic conductivity of the composite separator (to 1.77 mS cm^{-1}), facilitating Li^+ transport due to F-Li^+ interactions. Post gelation, the battery's discharge capacity after 250 cycles stands at ~1.28 mAh, exhibiting only a 27% capacity loss. This study introduced a novel composite separator design strategy for LIBs.

Moreover, the technique of integrating organic/inorganic components in traditional battery separator coatings is becoming increasingly prevalent, enhancing the safety and exceptional charging/discharging capacity of LIB via a synergistic blend of organic and inorganic substances. For example, Xiao et al. [76] innovated a novel core–shell composite separator using synergistic incorporation of PE wax and boehmite, where the meltable high-density polyethylene (HDPE) wax fused and masked pores, obstructing Li^+ ion paths above 130 °C due to its suitable T_m (130 ℃). Consequently, this modification exhibited robust cycling durability with a capacity retention rate of 81% after 200 cycles, contrasting the unaltered PE separator's capacity retention rate of 71%. Recently, Jiang et al. [77] introduced a multilayer separator (ASPESA) separator structure via casting layers of low-density polyethylene (LDPE) and Al_2O_3 on each side of PE membrane, applying an eco-friendly approach. This separator manifested shutdown capability at 120 ℃, offering superior thermal stability up to 185 ℃ with minimal shrinkage (1%). Concurrently, the added LDPE and Al_2O_3 layers enhanced electrolyte wetting and intake (407.23%). In Li||$LiFePO_4$ cells, this multilayer ASPESA separator exhibited outstanding cycle performance, retaining 98.9% of initial discharge capacity (vs. 5th cycle) at 144.5 mAh g^{-1} after 900 cycles. Consequently, this multilayer separator holds a significant promise as a high-security separator in LIBs. Notably, the coating's microstructure significantly impacts ion migration, electrolyte storage, and the separator's resistance to deformation and thermal damage under diverse conditions [87]. Shin et al. synthesized a novel organic-inorganic complex (CA–PEO–LPSQ) utilizing PEO functionalized ladder-like polysilsesquioxanes (LPSQs) and 4-(chloroacetyl) catechol (CA) [78]. The protonated PE-M-9 separator demonstrated superior wettability to both aqueous fluids and battery electrolytes. Also, it displayed limited thermal shrinkage at 120 ℃ (9%), outperforming PE-M-8 (13%), PE-M-10 (11%), and uncoated PE (26%) separators. Capacity retention was excellent at 0.5 C, retaining 98% of initial capacity post-first cycle and 82% after 300 cycles. Recently, Yue et al. [72] proposed a novel approach involving in situ enamel mineralization engineering coupled with thermal treatment for crafting a large-area, three-dimensional hydroxyapatite (HAP) nanosheet array-enhanced PE nanocomposite separator, demonstrating enhanced mechanical strength and excellent resistances to shrinking (**Figure 5**). At 120 ℃, the nanocomposite exhibited outstanding breaking stress of 3.7 MPa, remarkable toughness of 434.4 .4 MJ m^{-3}, and boosted friction coefficient of 0.69, outperforming both commercial PE separators and previously reported ceramic/PE composites. The elongation retention

achieved by the product at 180 °C reaches an exceptional value of 2456.4%, indicating superior thermo-mechanical stability.

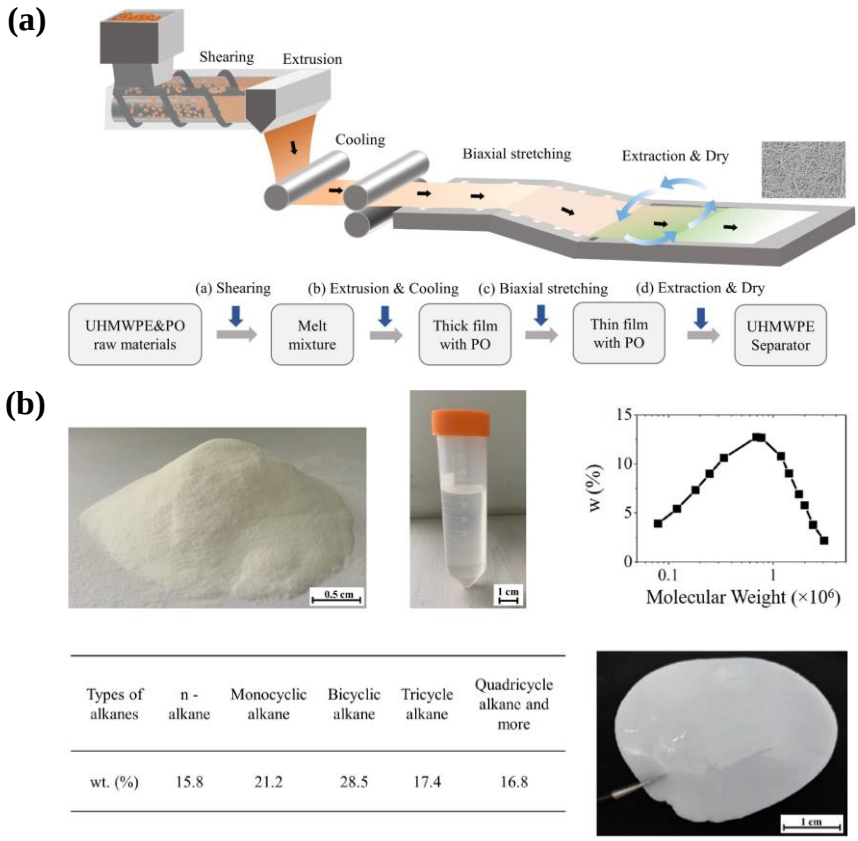

Figure 6. Schematics of the process and raw materials for separator membrane preparation in the study. **(a)** Illustration of the separator manufacture using wet biaxial-stretching processing; **(b)** characterization of UHMWPE and paraffin oil (PO).

Source: Reproduced with permission from [88], copyright John Wiley and Sons, 2023.

Significantly, UHMWPE holds a significant market share in commercial LIB separators due to its extreme puncture resistance, resilience against chemicals, exceptional microporosity, robust mechanical fortitude, high thermal stability, cost-efficient nature, etc. [89]. Babiker et al. [51] industrially synthesized UHMWPE/SiO_2 nanocomposites with minimal post-processing actions through biaxial stretching. Thermal shrinkage decreased notably, i.e., MD (1.7%) and TD (1%), as compared to pure UHMWPE (MD, 30.5%; TD, 27.6%). In addition, the composite demonstrated an extraordinary discharge capacity of 165 mAh g^{-1} at 0.1 C and 123 mAh g^{-1} at 5 C, along with excellent cycling performance (CE of 99.93% over 100 cycles; C-rate capability of 146.2 mAh g^{-1} at 1 C). Besides, organic additives like poly(4-methyl-1-pentene) (PMP) can further boost the performance of UHMWPE-based membranes. Habumugisha et al. [79] fabricated a UHMWPE/PMP blend membrane through sequential biaxial stretching, exhibiting low shrinkage after heat treatment (MD, 0.7%; TD, 1.6%). The rate capability test yielded a peak discharge capacity of 172.8 mAh g^{-1} at 0.1 C, exceeding the theoretical capacity of the $LiFePO_4$ cathode (170 mAh g^{-1}). Considering that any punctures produced on the membrane may potentially result in a

catastrophic failure of LIBs, Li et al. [80] designed a self-reinforced composite UHMWPE membrane with uniformly distributed nanopores (~200 nm) within interpenetrating nanofibrillar "shish-kebab" networks. This design resulted in a significant enhancement in tensile strength (550 MPa) and puncture resistance (1.5 N μm^{-1}) by preserving molecular orientation during pore closure. Furthermore, processing techniques can significantly influence the performance of UHMWPE-based membranes, Wu et al. [81] studied the impact of wet and dry methods on UHMWPE/liquid paraffin (LP) gel membranes. Results indicated that while dry method-derived separators showed improved electrochemical performance, they had inferior mechanical properties compared to those made via the wet method. Lastly, Ding et al. [82] successfully developed a separator with a uniform microporous structure and porous Al_2O_3 nanoparticles, prepared using a wet method and TIPS technique involving paraffin, nano-Al_2O_3, and UHMWPE The membrane exhibits superior electrochemical stability, ionic conductivity, and Li^+ transfer coefficients due to synergistic effects of uniform microporosity and Al_2O_3 nanospheres in the porous structure, facilitating efficient Li^+ transport and imparting exceptional performance. Recently, Wang et al. [88] developed commercial LIBs separators employing UHMWPE-PO blends. Using a dissipative particle dynamics model, they analyzed the influence of extrinsic (shear rate, cooling rate) and intrinsic (chain length) factors on blend microstructure (**Figure 6**). High shear induced minimal porosity (~28%) and small pores in UHMWPE with uniform chain length, while slow shear produced high porosity (~40%) and large pores. However, varying chain lengths did not alter porosity (~30%) but reduced pore size by ~35%. Post-shearing cooling rate proved crucial, rapidly increasing porosity by ~33% without altering pore size, while slowly cooling augmented porosity by ~74% and pore size by ~105%. This research provides a significant understanding of pore structure development during separator processing

4. Conclusions

LIBs are emerging as key solutions for energy storage and conversion, fulfilling the demand for environmentally friendly goods. With the global emphasis on sustainable energy, their considerable socio-economic and ecological importance is becoming evident. Intense studies in LIB separator membranes have spurred numerous advances in improving performance, boosting security measures, and overcoming intrinsic limitations. This review aims to provide an extensive database on LIBs separator membranes, covering performance requirements, functional elements, manufacturing techniques, applications, and effectiveness. It further explores recent developments in porous membranes made from polyolefins like PE, PP, UHMWPE, etc., including their synthesis, configuration, alteration, and sophistication. The advanced, robust membrane created through these initiatives has demonstrated superior efficacy across diverse applications, leading to a circular economy promoting waste minimization, cost reductions, and footprint confinement.

To conclude, the growing necessity for green products has elevated LIBs as primary energy storage and conversion options. The critical role of separator membranes requires extensive research targeting performance enhancement and resolution of related issues. In summary, this review's comprehensive content serves

as a valuable tool, facilitating a deep understanding of separator membranes and steering towards optimal performance, thereby advancing sustainable energy solutions

Funding: This research was funded by the Sinopec Technology Project (444180, 23118, and 223176). The authors gratefully acknowledge the financial support.

Conflict of interest: The authors declare no conflict of interest.

References

1. Di Lecce D, Verrelli R, Hassoun J. Lithium-ion batteries for sustainable energy storage: recent advances towards new cell configurations. Green Chemistry. 2017; 19(15): 3442-3467. doi: 10.1039/c7gc01328k
2. Chae BG, Park SY, Song JH, et al. Evolution and expansion of Li concentration gradient during charge–discharge cycling. Nature Communications. 2021; 12(1). doi: 10.1038/s41467-021-24120-w
3. Goodenough JB, Park KS. The Li-Ion Rechargeable Battery: A Perspective. Journal of the American Chemical Society. 2013; 135(4): 1167-1176. doi: 10.1021/ja3091438
4. Reddy MV, Mauger A, Julien CM, et al. Brief History of Early Lithium-Battery Development. Materials. 2020; 13(8): 1884. doi: 10.3390/ma13081884
5. Nishi Y. The development of lithium ion secondary batteries. The Chemical Record. 2001; 1(5): 406-413. doi: 10.1002/tcr.1024
6. Lin L, Ning H, Song S, et al. Flexible electrochemical energy storage: The role of composite materials. Composites Science and Technology. 2020; 192: 108102. doi: 10.1016/j.compscitech.2020.108102
7. Babiker DMD, Usha ZR, Wan C, et al. Recent progress of composite polyethylene separators for lithium/sodium batteries. Journal of Power Sources. 2023; 564: 232853. doi: 10.1016/j.jpowsour.2023.232853
8. Qi Z, Wang H. Advanced Thin Film Cathodes for Lithium Ion Batteries. Research. 2020; 2020. doi: 10.34133/2020/2969510
9. Yang Y, Chen Z, Lv T, et al. Ultrafast self-assembly of supramolecular hydrogels toward novel flame-retardant separator for safe lithium ion battery. Journal of Colloid and Interface Science. 2023; 649: 591-600. doi: 10.1016/j.jcis.2023.06.058
10. Liu F, Chuan X. Recent developments in natural mineral-based separators for lithium-ion batteries. RSC Advances. 2021; 11(27): 16633-16644. doi: 10.1039/d1ra02845f
11. Bicy K, Gueye AB, Rouxel D, et al. Lithium-ion battery separators based on electrospun PVDF: A review. Surfaces and Interfaces. 2022; 31: 101977. doi: 10.1016/j.surfin.2022.101977
12. Langner T, Sieber T, Rietig A, et al. A phenomenological and quantitative view on the degradation of positive electrodes from spent lithium-ion batteries in humid atmosphere. Scientific Reports. 2023; 13(1). doi: 10.1038/s41598-023-32688-0
13. Manjakkal L, Jain A, Nandy S, et al. Sustainable electrochemical energy storage devices using natural bast fibres. Chemical Engineering Journal. 2023; 465: 142845. doi: 10.1016/j.cej.2023.142845
14. Tajik M, Makui A, Tosarkani BM. Sustainable cathode material selection in lithium-ion batteries using a novel hybrid multi-criteria decision-making. Journal of Energy Storage. 2023; 66: 107089. doi: 10.1016/j.est.2023.107089
15. Cheng N, Ren L, Xu X, et al. Application of organic-inorganic hybrids in lithium batteries. Materials Today Physics. 2020; 15: 100289. doi: 10.1016/j.mtphys.2020.100289
16. Wu Y, Lei D, Wang C. The formation of LiAl5O8 nanowires from bulk Li-Al alloy enables dendrite-free Li metal batteries. Materials Today Physics. 2021; 18: 100395. doi: 10.1016/j.mtphys.2021.100395
17. Luo W, Cheng S, Wu M, et al. A review of advanced separators for rechargeable batteries. Journal of Power Sources. 2021; 509: 230372. doi: 10.1016/j.jpowsour.2021.230372
18. Wu SL, Qiao J, Guan J, et al. Nascent disentangled UHMWPE: Origin, synthesis, processing, performances and applications. European Polymer Journal. 2023; 184: 111799. doi: 10.1016/j.eurpolymj.2022.111799
19. Duan Y, Li L, Shen Z, et al. Engineering Metal-Organic-Framework (MOF)-Based Membranes for Gas and Liquid Separation. Membranes. 2023; 13(5): 480. doi: 10.3390/membranes13050480
20. Weidenkaff A, Wagner-Wenz R, Veziridis A. A world without electronic waste. Nature Reviews Materials. 2021; 6(6): 462-463. doi: 10.1038/s41578-021-00330-y
21. Wang W, Zhang Z, Ma L, et al. Explorations of complex thermally induced phase separation (C-TIPS) method for manufacturing novel diphenyl ether polysulfate flat microporous membranes. Journal of Membrane Science. 2022; 659:

120739. doi: 10.1016/j.memsci.2022.120739
22. Lagadec MF, Zahn R, Wood V. Characterization and performance evaluation of lithium-ion battery separators. Nature Energy. 2018; 4(1): 16-25. doi: 10.1038/s41560-018-0295-9
23. Serra JP, Fidalgo-Marijuan A, Martins PM, et al. Porous Composite Bifunctional Membranes for Lithium-Ion Battery Separator and Photocatalytic Degradation Applications: Toward Multifunctionality for Circular Economy. Advanced Energy and Sustainability Research. 2021; 2(7). doi: 10.1002/aesr.202100046
24. Akhmetova K, Tatykayev B, Kalybekkyzy S, et al. One-step fabrication of all-in-one flexible nanofibrous lithium-ion battery. Journal of Energy Storage. 2023; 65: 107237. doi: 10.1016/j.est.2023.107237
25. Ding L, Li D, Liu L, et al. Dependence of lithium metal battery performances on inherent separator porous structure regulation. Journal of Energy Chemistry. 2023; 84: 436-447. doi: 10.1016/j.jechem.2023.06.002
26. Serra JP, Uranga J, Gonçalves R, et al. Sustainable lithium-ion battery separators based on cellulose and soy protein membranes. Electrochimica Acta. 2023; 462: 142746. doi: 10.1016/j.electacta.2023.142746
27. Wang C, Zhu G, Hu Y, et al. Ionic conductivity and cycling stability-enhanced composite separator using hollow halloysite nanotubes constructed on PP nonwoven through polydopamine-induced water-based coating method. Colloids and Surfaces A: Physicochemical and Engineering Aspects. 2023; 667: 131403. doi: 10.1016/j.colsurfa.2023.131403
28. Zhu X, Roy JC, Li X, et al. Toward improved sustainability in lithium ion batteries using bio-based materials. Trends in Chemistry. 2023; 5(5): 393-403. doi: 10.1016/j.trechm.2023.03.004
29. Li Y, Yu L, Hu W, et al. Thermotolerant separators for safe lithium-ion batteries under extreme conditions. Journal of Materials Chemistry A. 2020; 8(39): 20294-20317. doi: 10.1039/d0ta07511f
30. Waqas M, Ali S, Feng C, et al. Recent Development in Separators for High-Temperature Lithium-Ion Batteries. Small. 2019; 15(33). doi: 10.1002/smll.201901689
31. Deng K, Qin J, Wang S, et al. Effective Suppression of Lithium Dendrite Growth Using a Flexible Single-Ion Conducting Polymer Electrolyte. Small. 2018; 14(31). doi: 10.1002/smll.201801420
32. Costa CM, Rodrigues HM, Gören A, et al. Preparation of Poly(vinylidene fluoride) Lithium-Ion Battery Separators and Their Compatibilization with Ionic Liquid - A Green Solvent Approach. ChemistrySelect. 2017; 2(19): 5394-5402. doi: 10.1002/slct.201701028
33. Lingappan N, Lee W, Passerini S, et al. A comprehensive review of separator membranes in lithium-ion batteries. Renewable and Sustainable Energy Reviews. 2023; 187: 113726. doi: 10.1016/j.rser.2023.113726
34. Gigova A. Investigation of the porous structure of battery separators using various porometric methods. Journal of Power Sources. 2006; 158(2): 1054-1061. doi: 10.1016/j.jpowsour.2005.11.006
35. Li L, Duan Y. Engineering Polymer-Based Porous Membrane for Sustainable Lithium-Ion Battery Separators. Polymers. 2023; 15(18): 3690. doi: 10.3390/polym15183690
36. Zhang L, Li X, Yang M, et al. High-safety separators for lithium-ion batteries and sodium-ion batteries: advances and perspective. Energy Storage Materials. 2021; 41: 522-545. doi: 10.1016/j.ensm.2021.06.033
37. Cronau M, Szabo M, König C, et al. How to Measure a Reliable Ionic Conductivity? The Stack Pressure Dilemma of Microcrystalline Sulfide-Based Solid Electrolytes. ACS Energy Letters. 2021; 6(9): 3072-3077. doi: 10.1021/acsenergylett.1c01299
38. Ding Y, Jiang Y, Zeng C, et al. Recent progress of advanced separators for Li-ion batteries. Journal of Materials Science. 2024; 59(27): 12154-12176. doi: 10.1007/s10853-024-09895-9
39. Lee Y, Park J, Jeon H, et al. In-depth correlation of separator pore structure and electrochemical performance in lithium-ion batteries. Journal of Power Sources. 2016; 325: 732-738. doi: 10.1016/j.jpowsour.2016.06.094
40. Rajagopalan Kannan DR, Terala PK, Moss PL, et al. Analysis of the Separator Thickness and Porosity on the Performance of Lithium-Ion Batteries. International Journal of Electrochemistry. 2018; 2018: 1-7. doi: 10.1155/2018/1925708
41. Zhong S, Yuan B, Guang Z, et al. Recent progress in thin separators for upgraded lithium ion batteries. Energy Storage Materials. 2021; 41: 805-841. doi: 10.1016/j.ensm.2021.07.028
42. Cannarella J, Liu X, Leng CZ, et al. Mechanical Properties of a Battery Separator under Compression and Tension. Journal of The Electrochemical Society. 2014; 161(11): F3117-F3122. doi: 10.1149/2.0191411jes
43. Wu J, Yuan L, Zhang W, et al. Reducing the thickness of solid-state electrolyte membranes for high-energy lithium batteries. Energy & Environmental Science. 2021; 14(1): 12-36. doi: 10.1039/d0ee02241a
44. Jin Y, Ai Z, Song Y, et al. Enhanced lithium storage performance of Si/C composite nanofiber membrane with carbon

coating as binder-free and self-supporting anode for lithium-ion battery. Materials Research Bulletin. 2023; 167: 112429. doi: 10.1016/j.materresbull.2023.112429

45. Yan J, Zhu J, Zhang L, et al. Na3V2(PO4)3-decorated separator as an improved catalysis ceramic layer for high-performance lithium sulfur batteries. Ionics. 2023; 29(6): 2271-2285. doi: 10.1007/s11581-023-04981-5
46. Murali DRL, Banihashemi F, Lin JYS. Zeolite membrane separators for fire-safe Li-ion batteries—Effects of crystal shape and membrane pore structure. Journal of Membrane Science. 2023; 680: 121743. doi: 10.1016/j.memsci.2023.121743
47. Lin W, Wang F, Wang H, et al. Thermal-Stable Separators: Design Principles and Strategies Towards Safe Lithium-Ion Battery Operations. ChemSusChem. 2022; 15(24). doi: 10.1002/cssc.202201464
48. Abraham KM. Directions in secondary lithium battery research and development. Electrochimica Acta. 1993; 38(9): 1233-1248. doi: 10.1016/0013-4686(93)80054-4.
49. Lee H, Yanilmaz M, Toprakci O, et al. A review of recent developments in membrane separators for rechargeable lithium-ion batteries. Energy Environ Sci. 2014; 7(12): 3857-3886. doi: 10.1039/c4ee01432d
50. Lin F, Markus IM, Doeff MM, et al. Chemical and Structural Stability of Lithium-Ion Battery Electrode Materials under Electron Beam. Scientific Reports. 2014; 4(1). doi: 10.1038/srep05694
51. Babiker DMD, Wan C, Mansoor B, et al. Superior lithium battery separator with extraordinary electrochemical performance and thermal stability based on hybrid UHMWPE/SiO_2 nanocomposites via the scalable biaxial stretching process. Composites Part B: Engineering. 2021; 211: 108658. doi: 10.1016/j.compositesb.2021.108658
52. Zhu X, Jiang X, Ai X, et al. TiO_2 ceramic-grafted polyethylene separators for enhanced thermostability and electrochemical performance of lithium-ion batteries. Journal of Membrane Science. 2016; 504: 97-103. doi: 10.1016/j.memsci.2015.12.059
53. Suharto Y, Lee Y, Yu JS, et al. Microporous ceramic coated separators with superior wettability for enhancing the electrochemical performance of sodium-ion batteries. Journal of Power Sources. 2018; 376: 184-190. doi: 10.1016/j.jpowsour.2017.11.083
54. Huang X. Separator technologies for lithium-ion batteries. Journal of Solid State Electrochemistry. 2010; 15(4): 649-662. doi: 10.1007/s10008-010-1264-9
55. Li D, Shi D, Xia Y, et al. Superior Thermally Stable and Nonflammable Porous Polybenzimidazole Membrane with High Wettability for High-Power Lithium-Ion Batteries. ACS Applied Materials & Interfaces. 2017; 9(10): 8742-8750. doi: 10.1021/acsami.6b16316
56. Jeon DH. Wettability in electrodes and its impact on the performance of lithium-ion batteries. Energy Storage Materials. 2019; 18: 139-147. doi: 10.1016/j.ensm.2019.01.002
57. Zhai P, Liu K, Wang Z, et al. Multifunctional separators for high-performance lithium ion batteries. Journal of Power Sources. 2021; 499: 229973. doi: 10.1016/j.jpowsour.2021.229973
58. Chen P, Ren H, Yan L, et al. Metal–Organic Frameworks Enabled High-Performance Separators for Safety-Reinforced Lithium Ion Battery. ACS Sustainable Chemistry & Engineering. 2019; 7(19): 16612-16619. doi: 10.1021/acssuschemeng.9b03854
59. Zhao P, Yang JP, Shang YM, et al. Surface modification of polyolefin separators for lithium ion batteries to reduce thermal shrinkage without thickness increase. Journal of Energy Chemistry. 2015; 24(2): 138-144. doi: 10.1016/S2095-4956(15)60294-7.
60. Ding L, Yan N, Zhang S, et al. Facile manufacture technique for lithium-ion batteries composite separator via online construction of fumed SiO_2 coating. Materials & Design. 2022; 215: 110476. doi: 10.1016/j.matdes.2022.110476
61. Yan Y, Kong QR, Sun CC, et al. Copolymer-assisted Polypropylene Separator for Fast and Uniform Lithium Ion Transport in Lithium-ion Batteries. Chinese Journal of Polymer Science. 2020; 38(12): 1313-1324. doi: 10.1007/s10118-020-2455-1
62. Yu J, Dong N, Liu B, et al. A newly-developed heat-resistance polyimide microsphere coating to enhance the thermal stability of commercial polyolefin separators for advanced lithium-ion battery. Chemical Engineering Journal. 2022; 442: 136314. doi: 10.1016/j.cej.2022.136314
63. Chen L, Yue FS, Zhao YM, et al. Surface tailoring of polypropylene separators for lithium-ion batteries via N-hydroxyphthalimide catalysis. European Polymer Journal. 2021; 152: 110487. doi: 10.1016/j.eurpolymj.2021.110487
64. Sun X, Xu J, Zhi X, et al. Electrospun organically modified sepiolite/PVDF coating on polypropylene separator to improve electrochemical performance of lithium-ion battery. Express Polymer Letters. 2024; 18(6): 575-591. doi: 10.3144/expresspolymlett.2024.43
65. Liu P, Zhang X, Ma C, et al. Preparation and Properties of PP/PAN/Cotton Fibers Composite Membrane as Lithium-Ion

Battery Separator with Thermal Shut-Off Function. Batteries. 2023; 9(2): 113. doi: 10.3390/batteries9020113
66. Li Y, Pu H. Facile fabrication of multilayer separators for lithium-ion battery via multilayer coextrusion and thermal induced phase separation. Journal of Power Sources. 2018; 384: 408-416. doi: 10.1016/j.jpowsour.2018.02.086
67. Wang Y, Wang Q, Lan Y, et al. Aqueous aluminide ceramic coating polyethylene separators for lithium-ion batteries. Solid State Ionics. 2020; 345: 115188. doi: 10.1016/j.ssi.2019.115188
68. Fu W, Xu R, Zhang X, et al. Enhanced wettability and electrochemical performance of separators for lithium-ion batteries by coating core-shell structured silica-poly(cyclotriphosphazene-co-4,4′-sulfonyldiphenol) particles. Journal of Power Sources. 2019; 436: 226839. doi: 10.1016/j.jpowsour.2019.226839
69. Qian W, Wu S, Lei C, et al. Aging Behavior of Polyethylene and Ceramics-Coated Separators under the Simulated Lithium-Ion Battery Service Compression and Temperature Field. Coatings. 2024; 14(4): 419. doi: 10.3390/coatings14040419
70. Ding H, Ge J, Zhang T, et al. Thermally stable poly-aromatic solid electrolyte coated polyethylene membrane as high-performance lithium-ion battery separator. Journal of Power Sources. 2024; 602: 234355. doi: 10.1016/j.jpowsour.2024.234355
71. Wang Z, Chen J, Ye B, et al. A pore-controllable polyamine (PAI) layer-coated polyolefin (PE) separator for pouch lithium-ion batteries with enhanced safety. Journal of Solid State Electrochemistry. 2020; 24(4): 843-853. doi: 10.1007/s10008-019-04488-y
72. Yue H, Yao Y, Li Y, et al. Thermally Resistant, Mechanically Robust, Enamel-Inspired Hydroxyapatite/Polyethylene Nanocomposite Battery Separator. Advanced Functional Materials. 2023; 34(7). doi: 10.1002/adfm.202308039
73. Kim KJ, Kwon YK, Yim T, et al. Functional separator with lower resistance toward lithium ion transport for enhancing the electrochemical performance of lithium ion batteries. Journal of Industrial and Engineering Chemistry. 2019; 71: 228-233. doi: 10.1016/j.jiec.2018.11.029
74. Sheng L, Song L, Gong H, et al. Polyethylene separator grafting with polar monomer for enhancing the lithium-ion transport property. Journal of Power Sources. 2020; 479: 228812. doi: 10.1016/j.jpowsour.2020.228812
75. Chen Q, Yang L, Gao X, et al. Polyvinylidene fluoride gel-polyethylene composite separator optimizing the interface compatibility between the separator and the electrode. Journal of Applied Polymer Science. 2024; 141(40). doi: 10.1002/app.56037
76. Xiao Y, Fu A, Zou Y, et al. High safety lithium-ion battery enabled by a thermal-induced shutdown separator. Chemical Engineering Journal. 2022; 438: 135550. doi: 10.1016/j.cej.2022.135550
77. Jiang Y, Sun C, Dong F, et al. Multilayer polyethylene separator with enhanced thermal properties for safe lithium-ion batteries. Particuology. 2024; 91: 29-37. doi: 10.1016/j.partic.2023.12.017
78. Shin SC, Kim J, Modigunta JKR, et al. Bio-mimicking organic-inorganic hybrid ladder-like polysilsesquioxanes as a surface modifier for polyethylene separator in lithium-ion batteries. Journal of Membrane Science. 2021; 620: 118886. doi: 10.1016/j.memsci.2020.118886
79. Habumugisha JC, Usha ZR, Yu R, et al. Thermally stable and high electrochemical performance ultra-high molecular weight polyethylene/poly(4-methyl-1-pentene) blend film used as Li-ion battery separator. Applied Materials Today. 2021; 24: 101136. doi: 10.1016/j.apmt.2021.101136
80. Li R, Gao P. Nanoporous UHMWPE Membrane Separators for Safer and High-Power-Density Rechargeable Batteries. Global Challenges. 2017; 1(4). doi: 10.1002/gch2.201700020
81. Wu Y, Yang F, Cao Y, et al. Investigation on cavitation behavior of ultrahigh molecular weight polyethylene during stretching in wet process and dry process. Polymer. 2021; 230: 124081. doi: 10.1016/j.polymer.2021.124081
82. Ding L, Li D, Du F, et al. Novel preparation of lithium-ion battery wet-processed separator based on the synergistic effect of porous skeleton nano-Al2O3in situ blending and synchro-draw. Polymer International. 2022; 72(1): 61-70. doi: 10.1002/pi.6447
83. Romano D, Marroquin-Garcia R, Gupta V, et al. An Unconventional Route for Synthesis and Solid-State Processing of Low-Entangled Ultra-High Molecular Weight Isotactic Polypropylene. Macromolecular Rapid Communications. 2023; 44(10). doi: 10.1002/marc.202300039
84. Hasanpoor M, Kerr R, Forsyth M, et al. Enhancing Lithium-Ion Battery Performance with Alumina-Coated Separators: Exploring the Potential of Different Alumina Particle Sizes, Coating Techniques, and Calendering. Batteries & Supercaps. 2024; 7(8). doi: 10.1002/batt.202400229
85. Jiang LL, Deng YZ, Luo T, et al. A smart membrane with negative thermo-responsiveness in battery electrolyte solution.

Journal of Membrane Science. 2024; 692: 122266. doi: 10.1016/j.memsci.2023.122266

86. Lee S, Byun S, Kang SW. Mass transport to generate the channels in cellulose polymers by vacuum-assisted process. International Journal of Biological Macromolecules. 2024; 259: 128337. doi: 10.1016/j.ijbiomac.2023.128337
87. Boateng B, Zhang X, Zhen C, et al. Recent advances in separator engineering for effective dendrite suppression of Li-metal anodes. Nano Select. 2021; 2(6): 993-1010. doi: 10.1002/nano.202000004
88. Wang H, Wu Z, Lu Y, et al. Understanding the pore structure evolution of polyethylene separator with dissipative particle dynamics simulation. Polymer Engineering & Science. 2023; 64(2): 518-533. doi: 10.1002/pen.26563
89. Babiker DMD, Yu R, Usha ZR, et al. High performance ultra-high molecular weight polyethylene nanocomposite separators with excellent rate capabilities designed for next-generation lithium-ion batteries. Materials Today Physics. 2022; 23: 100626. doi: 10.1016/j.mtphys.2022.100626

Energy Storage and Conversion 2024, 2(4), 1613.
https://doi.org/10.59400/esc1613

Review

MXene: A new revolution in the world of 2-D materials

Ruby Garg, Mohit Agarwal*

Department of Electronics and Communication Engineering, Thapar Institute of Engineering & Technology, Patiala, Punjab 147004, India
*** Corresponding author:** Mohit Agarwal, mohit.agarwal@thapar.edu

CITATION

Garg R, Agarwal M. MXene: A new revolution in the world of 2-D materials. Energy Storage and Conversion. 2024; 2(4): 1613. https://doi.org/10.59400/esc1613

ARTICLE INFO

Received: 13 August 2024
Accepted: 5 November 2024
Available online: 18 November 2024

Abstract: MXenes have imposed a profound effect on materials science and nanotechnology fields after their discovery in 2011. Theoretical models have predicted more than 100 potential compositions of MXene whereas laboratory-scale synthesis reflects their success of over 40 distinct structures till date. The distinctive properties of MXenes have led to their use for a diverse range of applications, such as energy storage, environmental remediation, electronics, communications, gas and liquid separation and adsorption, biomedical fields, and optoelectronics. The increased interest of researchers in MXenes has led to a wide rise in research publications, showing their growing importance in different scientific domains. In 2024, MXenes had shown wide potential in various areas, including energy storage devices, electromagnetic interference shielding, nanocomposites, and hybrid materials. However, the variations in the choice of precursors, reactor design, cost, synthesis parameters pose several challenges in ensuring the production of high-quality MXenes. The applicability of MXenes continues to broaden as its compositions are continuously accelerating. This review aims is to provide a comprehensive overview of MXene history, its properties, challenges, latest trends, and different applications to highlight its potential and gather new audiences towards this family of two-dimensional materials.

Keywords: supercapacitor; MXene; MAX; synthesis

1. Introduction

MXenes belongs to a novel class of two-dimensional (2D) materials comprising early transition metal carbides and nitrides, discovered first in 2011 [1]. This family of 2D materials is labeled the formula $M_{n+1}X_nT_x$, where M signifies early transition metals, X describes carbon or nitrogen and Tx refers to surface terminations such as fluorine (F), oxygen (O), hydroxyl (OH) [2,3].

The MXene structure is typically comprised of various n + 1 layers of M and intercalated with n layers of X, with numerous surface terminations. The selective etching method is used for the synthesis of MXenes that begins with taking a precursor material which is referred to as MAX phase [4]. The hexagonal packed structure of carbides and nitrides describes the layered MAX phase where A group in the periodic table represents the A elements in the MAX phase such as aluminum, gallium or silicon [5]. With the process of etching, delamination and exfoliation, the A-layer atoms in the MAX phase are selectively removed which provides 2D MXene flakes [6]. There are two main forms of MXene out of which is multilayered (ML) powder and the other is a single-flake colloidal solution. In ML-MXenes, the loosely attached MXene flakes are stacked, whereas the colloidal MXenes are prepared by exfoliating ML-MXenes into single-flake dispersions as shown in **Figure 1** [7,8].

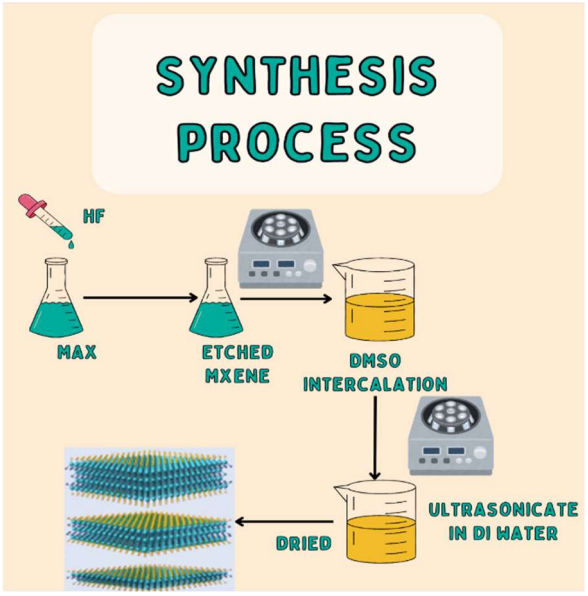

Figure 1. Schematic showing the synthesis of single layer and multilayered MXene.

Till date, four distinct compositional MXenes that are synthesized including M_2XT_x, $M_3X_2T_x$, $M_4X_3T_x$, and $M_5X_4T_x$ as shown in **Figure 2**. It demonstrates schematic representations of both old and newly discovered MXene structures.

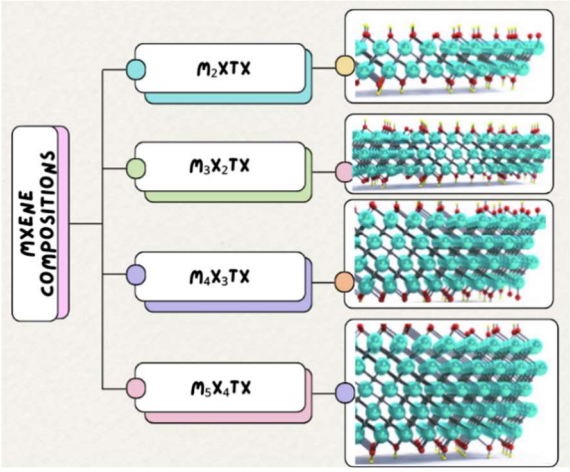

Figure 2. Schematic representation of successful synthesized MXenes.

Among these, $Ti_3C_2T_x$, which belongs to $M_3X_2T_x$ structure, was the first ever MXene reported in 2011 and it is one of the most widely studied out of all others [1,9,10]. The representation of the $M_3X_2T_x$ structure is shown in **Figure 3**. Thereafter, in 2012, MXenes was structured as defined by M_2XT_x and $M_4X_3T_x$ were identified [11]. In the general formula of $M_{n+1}X_nT_x$, precursor material determines its number of layers [5]. This dependency on MAX phases governs the achievement of thicker MXenes ($M_{n+1}X_nT_x$ with larger n) or to finding of new chemistries for M and X elements. In 2019, the discovery of the first-ever $M_5X_4T_x$ ($(Mo_4V)C_4T_x$) MXene happened from a new MAX phase with five layers of M (M_5AlC_4) after the selective etching of aluminum layers [12]. More than 100 successful compositions of MXene are found from the theoretical calculations on MAX phases and MXenes [13]. Researchers have created a wide spectrum of MXene array by varying elements in the

MAX phases by incorporating solid solutions at the M and X sites which allow them to fabricate a diverse array of MXene compositions. In 2012, the synthesis of the first solid-solution MXenes such as $(Ti,Nb)_2CT_x$, Ti_3CNT_x, and $(Cr,V)_3C_2T_x$, are carried out [11]. Afterward, a lot of studies on other MXene solid solutions are reported later in 2020 [14,15]. Despite random solid solutions, it has been seen that precise stoichiometric ratios of specific combinations of transition metals give birth to double-transition metal MXenes. This involved in-plane and out-of-plane ordered MXene. In plane category n = 1, such as $(Mo_2/_3Ti_1/_3)CT_x$ [3] whereas in out-of-plane category n = 2 or 3, such as Mo_2TiC_2Tx and $Mo_2Ti_3C_3T_x$ [16].

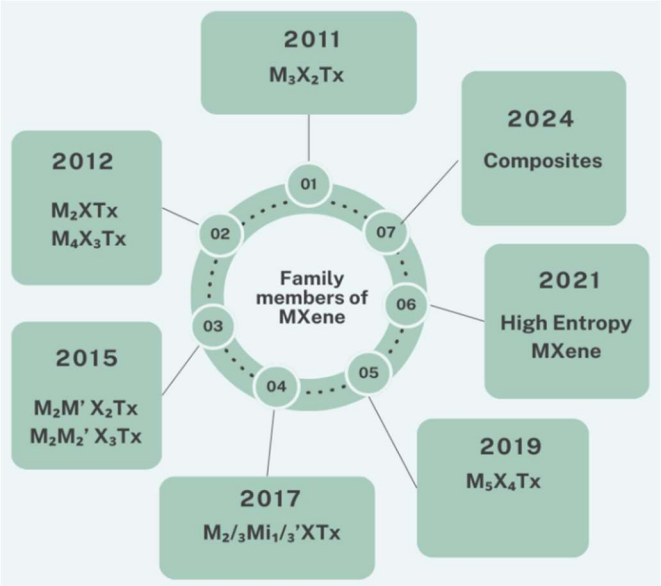

Figure 3. Advancement in the MXene family from 2011 to till date.

As shown by Alnoor et al. in their study, for validating MXene structures, its composition and defect distribution, electron microscopy plays a crucial role [17].

Further advancement in the MXene precursor chemistry specifically in the M and X elements has led to the discovery of other MXene compositions and structures. Later on, Nemani et al. [18] used high-entropy MAX carbide precursors: $TiVCrMoAlC_3$ and $TiVNbMoAlC_3$, for the successfully fabrication of two high-entropy M_4X_3Tx MXenes, $TiVCrMoC_3T_x$ and $TiVNbMoC_3T_x$. This innovation of his findings is shown in **Figure 1**, bottom. Additionally, one more research from the same year has reported the synthesis of a high-entropy M_2XT_x MXene [19]. The continued research in high-entropy MXenes further expands its potential applications in this rapidly advancing field.Fluorine (F), hydroxyl (OH), and oxygen (O) fall under the functional groups (T_x) in MXene. It has been illustrated from the Density Functional Theory (DFT) study that the electronic and magnetic properties are influenced strongly by the choice of these functional groups [20,21]. This is because the presence of functional groups on MXene surface significantly empower its electromagnetic properties, mainly by changing its electrical structure, that can result in changes such as conductivity, band gap, according to the functional group type. E.g. addition of oxygen (−O) functional groups can sometimes transit MXene from metallic into semiconductor, whereas the other

functional groups including fluorine (−F) can help in maintaining its metallic behavior with outstanding conductivity.

In the research carried out by Bae et al., it has been demonstrated that for accurately predicting the MXene behaviour, the selection of DFT methods is very important as different methods leads to varying results. For instance, the study of 22 different M_2CT_x MXenes (where M = Sc, Y, La, Ti, Zr, Hf, V, Nb, Ta, Mo, W, and T = O, F) through DFT and four different methods—Perdew-Burke-Ernzerhof (PBE), SCAN, HSE06, and PBE + U has resulted in new magnetic states in V_2CO_2, V_2CF_2, and Mo_2CF_2 [21].

A mixture of different surface terminations in experimental studies (e.g., F = O, OH), complicates the realization of predicted properties in MXene. However, a study carried out on MXenes in 2020 has successfully resulted in uniform surface terminations [22]. This achievement has proved that the findings of electronic and magnetic properties as predicted by DFT over the past decade can also be attained experimentally. Thus, controlling the MXene properties via surface terminations remains an area of active research which necessitates the further exploration of MXene through both experimental and computational methods.

Compared to other materials, superior performance has been shown by MXenes in the fields of electromagnetic interference (EMI) shielding. If compared with the same thickness, the titanium- based MXenes such as $Ti_3C_2T_x$ and Ti_3CNT_x possesses EMI shielding effectiveness which surpasses even copper and aluminum thin films [23,24]. Further the optimization of MXenes for the EMI shielding properties can be carried out by varying the transition metals used in their composition or by adjusting the number of layers (n), which generally correlates with their electrical conductivity [15]. Furthermore, MXenes combined with polymers are used to create MXene-polymer composites which have been provenly effective in improving EMI shielding capabilities [22]. It has been depicted from the literature that in various polymer matrices, MXenes are increasingly used as filler materials which reflect its significant recognition among various research domains [25]. Due to their hydrophilic property, it allows MXene to form a bond with hydrophilic polymers such as polydiallyldimethylammonium chloride, polyvinyl alcohol, and polyacrylic acid [25]. In comparison to other materials, properties including surface functionalities, extensive compositional range, high aspect ratios, and large surface area of the 2D flakes provide distinctive advantages to MXenes in polymeric composites. When dispersion of MXenes is carried uniformly within polymer matrices, its thermal, morphological, mechanical, and rheological properties can be significantly improved [25].

The research on MXene-polymer nanocomposites has been seen growing rapidly with over 150 journal articles published between 2018 and 2024, as compared to only 50 articles from 2011 to 2017 [25]. Furthermore, conductive polymers such as poly (aniline), polypyrrole, and polystyrene sulfonate have attracted the attention of researchers for their interactions with MXenes. These nanocomposites of MXene-polymer have potential applications in strain sensors, electromagnetic shields, energy storage devices, and gas sensors [26,27]. Additionally, due to this nanocomposite it has also been investigated that the overall shelf life of MXene has also been improved significantly. Since MXenes are prone to oxidation, the incorporation of MXene flakes

in solid polymer nanocomposites also helps in mitigating oxidation rates, which are initially affected by exposure to air, water, and temperature [28,29].

The most widely studied application of MXene is their electrochemical energy storage [10]. **Figure 4** lists some of the properties of MXene which describes one of the reasons why MXenes shows great efficacy in the field of energy storage and its comparison with traditional materials in terms of the properties is summarized through **Table 1**. Since their electronic and ionic conductivity is very high, they act as an extremely suitable material in batteries and supercapacitors. With the latest advancements in MXene compositions and composites, their energy storage performance has significantly improved [30].

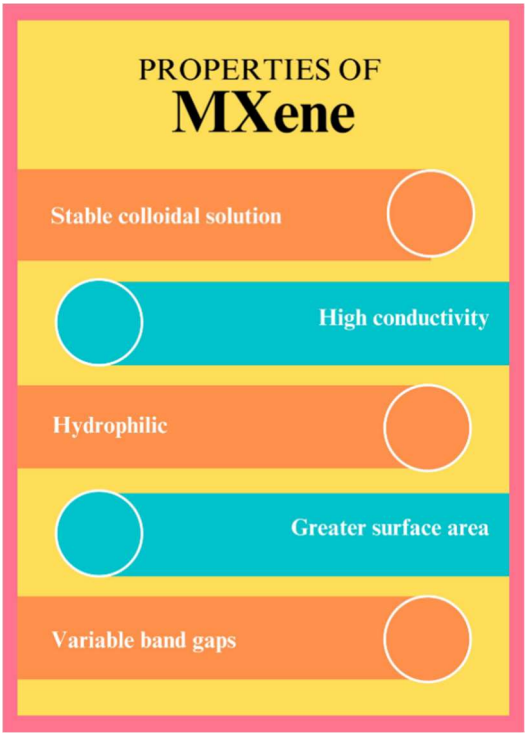

Figure 4. Highlight of various key properties of MXene.

Table 1. MXene advantages over traditional materials.

Property	MXene Materials	Traditional Materials	Advantages	References
Electrical Conductivity	High electrical conductivity (comparable to metals)	Lower conductivity, especially in oxide materials (e.g., MnO_2, ZnO)	Faster electron transfer, enhanced response times in sensors and energy storage	[31]
Surface Area and Layered Structure	Large surface area and tunable layered structure	Often lower surface area and limited tunability	Greater ion-accessibility, better electrode performance in supercapacitors	[32]
Mechanical Flexibility	Highly flexible and can form freestanding films	Limited flexibility in many traditional ceramics and oxides	Suitable for flexible and wearable energy devices and sensors	[31,33]
Surface Chemistry	Abundant surface terminations (e.g., −OH, −F) enable functionalization	Often difficult to functionalize	Enables targeted chemical interactions, enhancing sensitivity and selectivity	[32]
Thermal Stability	Stable under high temperatures, especially nitrides (MXenes)	Variable; many degrade at high temperatures	Suitable for high-temperature applications like industrial sensors	[31]
Environmental Impact	Generally lower toxicity with safe synthesis routes being developed	Some traditional materials, e.g., cobalt, are harmful to environment	More eco-friendly options for sustainable applications	[31]

For instance, Organi et al. in their study successfully synthesized a freestanding, ultralightweight, additive-free $Ti_3C_2T_x$ MXene aerogel using unidirectional freeze casting. This study demonstrated that strain resistance up to 50% can be achieved with $Ti_3C_2T_x$ aerogel. Because of the aerogel technology, electrochemical performance, including high specific capacity, excellent rate performance, and outstanding cyclic stability is achieved. During the aerogel fabrication, the flakes restacking problem in MXene is prevented which eliminates the need for electrochemical cycling to achieve maximum capacity. In this study it also has been mentioned that the orientation of 2D flakes within the MXene structure also influenced the mechanical and electrical properties of the aerogels. Thus, the outstanding electro-mechanical properties achieved suggest that these aerogels can act as a promising candidate for high-quality strain sensors [34].

Further Shao et al., synthesized $Ti_3C_2T_x$ MXene because of the property of its hydrophilic nature which enhances the transportation of electrolyte ions in aqueous solution. The performance metrics obtained from this approach showed a specific capacitance of 245 F/g, energy density of 35 Wh/kg, and a power density of 2500 W/kg. These results proved the application of MXene-based electrodes in supercapacitor, especially in aqueous systems where fast ion transfer benefits its energy storage. Traditional electrode materials generally face drawbacks towards ion transportation, energy density, and capacitive performance [35].

Afterwards, a study by Liu et al. showed the introduction of PANI into $Ti_3C_2T_x$ synthesising $Ti_3C_2T_x$/PANI composite, for improving the specific capacitance to 530 F/g and achieving 52 Wh/kg energy density. The research revealed that with the integration of polyaniline (PANI) the pseudocapacitive behavior is promoted which leads to improving both the capacity and stability that is vital for energy storage applications [36].

Later, research by Zhao explored the modification of $Ti_3C_2T_x$ MXene by $Ni(OH)_2$, presenting the capacitance of 700 F/g and an energy density of 138.4 Wh/kg. The novelty of this article showed that with incorporating $Ni(OH)_2$ in MXene, it boosts its redox activity thus facilitating higher energy and stability suitable for robust, power-demanding applications [37].

Feng et al. (2022) presented the development of MXene/carbon nanocomposites for enhancing the performance of fabricated flexible energy storage devices. The research focused on designing a hybrid structure which combined MXene's property of high electrical conductivity with structural stability of nanocarbons. The result forms a hyrid material showing the capability of delivering capacitive value of 380 F/g and an energy density of 47 Wh/kg. The novelty from this study lies in optimizing the configuration of layers such as efficient electron pathways of

MXenes and strength and flexibility of nanocarbon which helped in providing a practical and portable energy storage solutions. This unique strategy possibles the composite material to yield high power density, making it suitable for flexible electronic applications and wearable devices [38]. **Table 2** highlights some more publications showing the comparison of MXene based on their performance metrics:

Table 2. Comparing different MXene compositions based on their performance metrics.

Material	Capacitance (F/g)	Energy Density (Wh/kg)	Power Density (W/kg)	Cycles	References
$Ti_3C_2T_x$ flakes	375	38	8000	10,000	[39]
$Ti_3C_2T_x$ nanofluids	300	33	5000	8000	[40]
$Ti_3C_2T_x$/AuNPs (Symmetric SC)	696.67	138.4	2076	5000	[31]
$Ti_3C_2T_x$/PANI@M-$Ti_3C_2T_x$ Hybrid	530	52	480	-------	[41]
$Ti_3C_2T_x$ with graphene	254	35.28	18.14	5000	[42]

The exceptional mechanical strength, bending rigidity, and control over 2D flake thicknesses of MXene flakes also make them a promising candidate for tribological applications [43]. For example, to improve the antifrictional properties of base oil, the addition of just 0.8 wt% $Ti_3C_2T_x$ did a great job [44]. Huang et al. [43] in their research achieved superlubricity by coating $Ti_3C_2T_x$ MXene on a silicon substrate which resulted in a friction coefficient of 0.0067 ± 0.0017, that is 3.3 times lower if only silicon substrate is used. This discovery opens new paths for exploring MXene coatings as innovative solid lubricants for various applications.

2. Challenges faced by industries

The massive adoption of MXenes in industries has faced a lot of challenges related to environmental impact and production costs. For efficient synthesis of MXene, selecting an appropriate technique is also very important as it has a huge impact on its production efficiency, quality and cost-effectiveness. From the literature, it has been seen those methods for instance, chemical etching and exfoliation, show different results of MXenes in terms of surface area, morphology, and layer thickness [45]. All these properties are directly linked in affecting the material's electrochemical, mechanical, and thermal performance, which are vital for applications involving energy storage and catalysis. In addition to this, scalability, environmental impact, and economic viability are also affected by the right choice of manufacturing technique. Thus, it is very crucial to optimize these techniques so that desired material properties and production efficiency can be achieved. In **Figure 5** all these challenges related to the production of MXene are illustrated. For the large-scale production of MXene, reactor choice is a crucial parameter as.

Figure 5. Illustration showing various challenges affecting the quality of MXene synthesized.

It impacts material quality, scalability, and cost measurements.

During reactor selection, operational parameters such as temperature, pressure, and mixing are affected, which further influences the chemical and structural properties of MXenes. Further, the design of the reactor should also be chosen in such a way that the yield, production rate, and energy consumption will be in good shape. Thus, to produce MXenes for numerous fields, the choice of reactor plays a pivot role. Additionally, factors such as reactor material composition and safety design are very important in obtaining its overall performance.

It should also be kept in mind that appropriate precursors selection for the right quality MXene is also an important factor crucial for limiting cost and enhancing material quality. The composition and qualities of the final MXene product formed are highly affected by the choice of precursors. To minimize production costs, affordable and easily available precursors can help in this scenario. Additionally, the right quantity of precursor material influences the purity and uniformity of MXenes, which thus results in affecting its capabilities in energy storage devices. However, if the impurities or variations in quantity or quality of precursor are present, it may lead to poor MXene properties, affecting its product quality and reliability. Thus, to carefully balance cost-effectiveness with high-quality MXene, precursor selection plays a crucial role in ensuring the optimal performance and market competitiveness.

Further, the parameter that is also responsible for playing a major role is the consistency in the property of MXene as any variation in this might results in producing inconsistent performance, creating hurdles in fulfilling the requirements of certain applications. This may result in additional testing and controlling the quality measures, further leading to increased production costs. Moreover, flexibility in choosing the material properties will also compromise MXene reliability and effectiveness, and less market acceptance. Thus, it is very important to ensure that the material properties are consistent for optimal product performance, reducing the need for extensive quality control for cost purposes and mitigating waste.

High costs and environmental hazards to raw material pose a significant barrier towards the large-scale production of MXene. To mitigate these issues, changes in chemical usage or precursor materials are carried out. For instance, if transition metal oxides (e.g., TiO_2 instead of Ti) are substituted against transition metals, the cost of fabricating MAX phase can be significantly lowered [46]. Furthermore, the usage of low-cost sources of A layer atoms such as recycled aluminum or silicon, and alternative sources of carbon, such as recycled carbon from tires can also help in reducing the cost problems. As aluminum and recycled carbon is abundantly present in scrap and tires globally, they offer lower costs and reduction in greenhouse gas emissions in comparison to traditional sources [46–48].

One of the research carried out by Jolly et al. [33] uses secondary aluminum, titanium dioxide, and recycled carbon from tires for the synthesis of $Ti_3C_2T_x$ MXene from the Ti_3AlC_2 MAX phase. With this method, MXene exhibited an electrical conductivity of 5857 ± 680 S/cm and comparable electrochemical performance in supercapacitors to that of $Ti_3C_2T_x$ MXenes produced by conventional methods. This approach represents a significant step towards

optimizing the environmental impact and cost-efficiency of MXene production. While traditional MXene fabrication methods are already being explored for

commercial applications, cost- effective and environmentally friendly production methods have the potential to accelerate the broader industrial application of MXenes. The selection of an appropriate technique for MXene bulk manufacturing is crucial due to its substantial impact on production efficiency, material quality, and cost-effectiveness [49]. Various methodologies, including chemical etching and exfoliation, result in MXenes with differing properties such as surface area, morphology, and layer thickness. These properties, in turn, influence the material's electrochemical, mechanical, and thermal performance, which are critical for its applications in energy storage and catalysis.

Moreover, **Table 3** summarizes the application level, advantages, and disadvantages of MXenes in specific industries, including strain sensors, gas sensors, and energy storage devices.

Table 3. Highlighting MXene pros and cons in various fields.

Industry/Application	Level of Application	Advantages	Disadvantages	References
Strain Sensors	Emerging, prototypes in wearable tech	High sensitivity due to conductivity and flexibility, allowing precise strain detection	Limited long-term stability in humid conditions	[50,51]
		Capable of detecting small strains with high gauge factor	Potential oxidation reduces conductivity over time	[52]
Gas Sensors	Research phase, early development	Tunable surface chemistry for selective detection (e.g., NO_2, NH_3), rapid response time	Susceptible to oxidation in air, requiring surface passivation for stability	[53]
		Fast response and recovery times due to high surface area	Sensitivity can be affected by environmental factors (e.g., humidity) 26	[54]
Energy Storage Devices	Commercial research and development	High conductivity, enabling fast charge/discharge rates suitable for supercapacitors and batteries	Limited by low voltage window in aqueous supercapacitors	[55,56]
		High capacity and cycling stability, suited for long-term applications	Synthesis cost and scalability challenges in large-scale manufacturing	[57,58]

3. Future scope

The improvement in synthesizing MXene is widely dependent on innovative technologies and breakthroughs. Modern reactor designs, precursor choice, optimization of synthesis method, environmental conditions and cost parameters are the major parameters for enhancing the quality and properties of MXene. Further, the industrial-scale production of MXene is highly influenced if the academia and industries collaborate. The results generated by academic research provide insights into its foundation, novel synthesis methods, and the latest material discoveries. Whereas, with industry it shapes it practically in terms of applications and scalability requirements. This vital interaction between academics and industries accelerates the outcomes of research findings to practical applications, thus enhancing production efficiency, minimizing costs, and improving quality. This collaborative ecosystem, driven by the exchange of knowledge and resources between academic and industrial sectors, fosters advancements in MXene manufacturing that are both theoretically robust and commercially viable for diverse applications. Further, the innovative composites of MXene with new materials and MXene composition with its family

members can also revolutionize the industry with the best combination which can result in improved energy storage devices.

4. Conclusion

Ultimately, this review focuses on depicting MXene materials as the pioneers in the area of advanced materials, showing its significant potential in various sectors such as electronics, solar, energy storage, and batteries. However, synthesizing MXene came across various challenges related to maintaining quality, cost, and consistency. Environmental and safety concerns are also addressed within the review. It offers a comprehensive roadmap for researchers, industry professionals, and policymakers, fostering scientific advancements and facilitating the widespread adoption of MXene materials. This collaborative effort between academia and industry is essential for leveraging MXene's capabilities to address contemporary challenges and drive innovation across multiple domains. Since the discovery of MXene in 2011, explosive growth has been witnessed on the research of this 2D material, with over 8300 research articles successfully published in more than 400 journals in 62 countries [59]. The number of published articles has been showing an upward trend, with over 3000 manuscripts alone published in 2022, as compared to 1493 and 226 in 2020 and 2017. This reflects its progressive growth as the increase in material's relevance has broaden the scope of its applications. Additionally, the data from google scholar reveals a sharp rise in interest for "MXene" globally since 2015, aiming to reflect its overall growth in research engagement. The publication surge, combined with the its compositions and glorified online interest, highlights the rapid expansion and immense potential of MXenes across various scientific and industrial fields.

Conflict of interest: The authors declare no conflict of interest.

References

1. Naguib M, Kurtoglu M, Presser V, et al. Two-Dimensional Nanocrystals Produced by Exfoliation of Ti_3AlC_2. Advanced Materials. 2011; 23(37): 4248–4253. doi: 10.1002/adma.201102306
2. Anasori B, Lukatskaya MR, Gogotsi Y. 2D metal carbides and nitrides (MXenes) for energy storage. Nature Reviews Materials. 2017; 2(2). doi: 10.1038/natrevmats.2016.98
3. VahidMohammadi A, Rosen J, Gogotsi Y. The world of two-dimensional carbides and nitrides (MXenes). Science. 2021; 372(6547). doi: 10.1126/science.abf1581
4. Garg R, Agarwal A, Agarwal M. Synthesis and characterization of solution processed MXene. DAE SOLID STATE PHYSICS SYMPOSIUM 2019. 2020; 2265: 030665. doi: 10.1063/5.0016599
5. Sokol M, Natu V, Kota S, et al. On the Chemical Diversity of the MAX Phases. Trends in Chemistry. 2019; 1(2): 210–223. doi: 10.1016/j.trechm.2019.02.016
6. Anasori B, Gogotsi Y, eds. 2D Metal Carbides and Nitrides (MXenes). Springer International Publishing; 2019. doi: 10.1007/978-3-030-19026-2
7. Verger L, Natu V, Carey M, et al. MXenes: An Introduction of Their Synthesis, Select Properties, and Applications. Trends in Chemistry. 2019; 1(7): 656–669. doi: 10.1016/j.trechm.2019.04.006
8. Alhabeb M, Maleski K, Anasori B, et al. Guidelines for Synthesis and Processing of Two-Dimensional Titanium Carbide ($Ti_3C_2T_x$ MXene). Chemistry of Materials. 2017; 29(18): 7633–7644. doi: 10.1021/acs.chemmater.7b02847
9. Ye HZ, Liu XY, Review of recent studies in magnesium matrix composites. Springer nature link. 2004; 39: 6153–6171. doi: 10.1023/B:JMSC.0000043583.47148.31
10. Gogotsi Y, Anasori B. The Rise of MXenes. ACS Nano. 2019; 13(8): 8491–8494. doi: 10.1021/acsnano.9b06394

11. Naguib M, Mashtalir O, Carle J, et al. Two-Dimensional Transition Metal Carbides. ACS Nano. 2012; 6(2): 1322–1331. doi: 10.1021/nn204153h
12. Deysher G, Shuck CE, Hantanasirisakul K, et al. Synthesis of Mo4VAlC4 MAX Phase and Two-Dimensional Mo4VC4 MXene with Five Atomic Layers of Transition Metals. ACS Nano. 2019; 14(1): 204–217. doi: 10.1021/acsnano.9b07708
13. Frey NC, Wang J, Vega Bellido GI, et al. Prediction of Synthesis of 2D Metal Carbides and Nitrides (MXenes) and Their Precursors with Positive and Unlabeled Machine Learning. ACS Nano. 2019; 13(3): 3031–3041. doi: 10.1021/acsnano.8b08014
14. Han M, Maleski K, Shuck CE, et al. Tailoring Electronic and Optical Properties of MXenes through Forming Solid Solutions. Journal of the American Chemical Society. 2020; 142(45): 19110–19118. doi: 10.1021/jacs.0c07395
15. Han M, Shuck CE, Rakhmanov R, et al. Beyond $Ti_3C_2T_x$: MXenes for Electromagnetic Interference Shielding. ACS Nano. 2020; 14(4): 5008–5016. doi: 10.1021/acsnano.0c01312
16. Hong W, Wyatt BC, Nemani SK, et al. Double transition-metal MXenes: Atomistic design of two-dimensional carbides and nitrides. MRS Bulletin. 2020; 45(10): 850–861. doi: 10.1557/mrs.2020.251
17. Alnoor H, Elsukova A, Palisaitis J, et al. Exploring MXenes and their MAX phase precursors by electron microscopy. Materials Today Advances. 2021; 9: 100123. doi: 10.1016/j.mtadv.2020.100123
18. Nemani SK, Zhang B, Wyatt BC, et al. High-Entropy 2D Carbide MXenes: $TiVNbMoC_3$ and $TiVCrMoC_3$. ACS Nano. 2021; 15(8): 12815–12825. doi: 10.1021/acsnano.1c02775
19. Du Z, Wu C, Chen Y, et al. High-Entropy Atomic Layers of Transition-Metal Carbides (MXenes). Advanced Materials. 2021; 33(39). doi: 10.1002/adma.202101473
20. Khazaei M, Mishra A, Venkataramanan NS, et al. Recent advances in MXenes: From fundamentals to applications. Current Opinion in Solid State and Materials Science. 2019; 23(3): 164–178. doi: 10.1016/j.cossms.2019.01.002
21. Bae S, Kang YG, Khazaei M, et al. Electronic and magnetic properties of carbide MXenes—the role of electron correlations. Materials Today Advances. 2021; 9: 100118. doi: 10.1016/j.mtadv.2020.100118
22. Yang Y, Hantanasirisakul K, Frey NC, et al. Distinguishing electronic contributions of surface and sub-surface transition metal atoms in Ti-based MXenes. 2D Materials. 2020; 7(2):025015. doi: 10.1088/2053-1583/ab68e7
23. Kamysbayev V, Filatov AS, Hu H, et al. Covalent surface modifications and superconductivity of two-dimensional metal carbide MXenes. Science. 2020; 369(6506): 979–983. doi: 10.1126/science.aba8311
24. Iqbal A, Shahzad F, Hantanasirisakul K, et al. Anomalous absorption of electromagnetic waves by 2D transition metal carbonitride Ti 3 CNT x (MXene). Science. 2020; 369(6502): 446–450. doi: 10.1126/science.aba7977
25. Carey M, Barsoum MW. MXene polymer nanocomposites: a review. Materials Today Advances. 2021; 9: 100120. doi: 10.1016/j.mtadv.2020.100120
26. Yue Y, Liu N, Liu W, et al. 3D hybrid porous Mxene-sponge network and its application in piezoresistive sensor. Nano Energy. 2018; 50: 79–87. doi: 10.1016/j.nanoen.2018.05.020
27. Garg R, Agarwal A, Agarwal M. A review on MXene for energy storage application: effect of interlayer distance. Materials Research Express. 2020; 7(2): 022001. doi: 10.1088/2053-1591/ab750d
28. Chae Y, Kim SJ, Cho SY, et al. An investigation into the factors governing the oxidation of two-dimensional Ti_3C_2MXene. Nanoscale. 2019; 11(17): 8387–8393. doi: 10.1039/c9nr00084d
29. Habib T, Zhao X, Shah SA, et al. Oxidation stability of $Ti_3C_2T_x$ MXene nanosheets in solvents and composite films. npj 2D Materials and Applications. 2019; 3(1). doi: 10.1038/s41699-019-0089-3
30. Garg R, Agarwal A, Agarwal M. Effect of vanadium doping on MXene-based supercapacitor. Journal of Materials Science: Materials in Electronics. 2021; 32(17): 22046–22059. doi: 10.1007/s10854-021-06668-x
31. Mustafa B, Lu W, Wang Z, et al. Ultrahigh Energy and Power Densities of d-MXene-Based Symmetric Supercapacitors. Nanomaterials. 2022; 12(19): 3294. doi: 10.3390/nano12193294
32. N.K. PS, Jeong SM, Rout CS. MXene-carbon-based hybrid materials for supercapacitor applications. Energy Advances. 2024; 2. doi: 10.1039/D3YA00502J
33. Rong C, Su T, Li Z, et al. Elastic properties and tensile strength of 2D $Ti_3C_2T_x$ MXene monolayers. Nature Communications. 2024; 15(1). doi: 10.1038/s41467-024-45657-6
34. Orangi J, Tetik H, Parandoush P, et al. Conductive and highly compressible MXene aerogels with ordered microstructures as high-capacity electrodes for Li-ion capacitors. Materials Today Advances. 2021; 9: 100135. doi: 10.1016/j.mtadv.2021.100135

35. Shao H, Lin Z, Xu K, et al. Electrochemical study of pseudocapacitive behavior of $Ti_3C_2T_x$ MXene material in aqueous electrolytes. Energy Storage Materials. 2019; 18: 456–461. doi: 10.1016/j.ensm.2018.12.017
36. Usman KAS, Qin S, Henderson LC, et al. $Ti_3C_2T_x$ MXene: from dispersions to multifunctional architectures for diverse applications. Materials Horizons. 2021; 8(11): 2886–2912. doi: 10.1039/d1mh00968k
37. Ma R, Chen Z, Zhao D, et al. $Ti_3C_2T_x$ MXene for electrode materials of supercapacitors. Journal of Materials Chemistry A. 2021; 9(19): 11501–11529. doi: 10.1039/d1ta00681a
38. Hu M, Cheng R, Li Z, et al. Interlayer engineering of $Ti_3C_2T_x$ MXenes towards high capacitance supercapacitors. Nanoscale. 2020; 12(2): 763–771. doi: 10.1039/c9nr08960h
39. Fan Y, Mei X, Ye L, et al. Tailoring $Ti_3C_2T_x$ MXene Flake Sizes for Modified Electrochemical Performance: A Top-down Approach. Current Physics. 2024; 1(1). doi: 10.2174/0127723348268837231206095532
40. Samylingam I, Kadirgama K, Samylingam L, et al. Review of $Ti_3C_2T_x$ MXene Nanofluids: Synthesis, Characterization, and Applications. Engineering, Technology & Applied Science Research. 2024; 14(3): 14708–14712. doi: 10.48084/etasr.7504
41. N. K. PS, Jeong SM, Rout CS. MXene–carbon based hybrid materials for supercapacitor applications. Energy Advances. 2024; 3(2): 341–365. doi: 10.1039/d3ya00502j
42. Nahirniak S, Ray A, Saruhan B. Challenges and Future Prospects of the MXene-Based Materials for Energy Storage Applications. Batteries. 2023; 9(2): 126. doi: 10.3390/batteries9020126
43. Huang S, Mutyala KC, Sumant AV, et al. Achieving superlubricity with 2D transition metal carbides (MXenes) and MXene/graphene coatings. Materials Today Advances. 2021; 9: 100133. doi: 10.1016/j.mtadv.2021.100133
44. Liu Y, Zhang X, Dong S, et al. Synthesis and tribological property of Ti3C2T X nanosheets. Journal of Materials Science. 2016; 52(4): 2200–2209. doi: 10.1007/s10853-016-0509-0
45. Garg R, Agarwal A, Agarwal M. Synthesis and optimisation of MXene for supercapacitor application. Journal of Materials Science: Materials in Electronics. 2020; 31(21): 18614–18626. doi: 10.1007/s10854-020-04404-5
46. Jolly S, Paranthaman MP, Naguib M. Synthesis of Ti3C2Tz MXene from low-cost and environmentally friendly precursors. Materials Today Advances. 2021; 10: 100139. doi: 10.1016/j.mtadv.2021.100139
47. Modaresi R, Müller DB. The Role of Automobiles for the Future of Aluminum Recycling. Environmental Science & Technology. 2012; 46(16): 8587–8594. doi: 10.1021/es300648w
48. Naskar AK, Bi Z, Li Y, et al. Tailored recovery of carbons from waste tires for enhanced performance as anodes in lithium-ion batteries. RSC Advances. 2014; 4(72): 38213. doi: 10.1039/c4ra03888f
49. Garg R, Agarwal A, Agarwal M. Performance of Copper Sulfide Hollow Rods in a Supercapacitor Based on Flexible Substrates. Journal of Electronic Materials. 2021; 50(12): 6974–6980. doi: 10.1007/s11664-021-09162-6
50. Shao B, Chen X, Chen X, et al. Advancements in MXene Composite Materials for Wearable Sensors: A Review. Sensors. 2024; 24(13): 4092. doi: 10.3390/s24134092
51. Chu T, Wang G, Zhang X, et al. High-Density Dual-Structure Single-Atom Pt Electrocatalyst for Efficient Hydrogen Evolution and Multimodal Sensing. Nano Letters. 2024; 24(31): 9666–9674. doi: 10.1021/acs.nanolett.4c02428
52. Chen H, Zhuo F, Zhou J, et al. Advances in graphene-based flexible and wearable strain sensors. Chemical Engineering Journal. 2023; 464: 142576. doi: 10.1016/j.cej.2023.142576
53. Devaraj M, Rajendran S, Hoang TKA, et al. A review on MXene and its nanocomposites for the detection of toxic inorganic gases. Chemosphere. 2022; 302: 134933. doi: 10.1016/j.chemosphere.2022.134933
54. Ding W, Yu J, Tsow F, et al. Highly sensitive and reversible MXene-based micro quartz tuning fork gas sensors with tunable selectivity. npj 2D Materials and Applications. 2024; 8(1). doi: 10.1038/s41699-024-00452-1
55. Wang Z, Han R, Zhang H, et al. An Intrinsically Nonflammable Electrolyte for Prominent-Safety Lithium Metal Batteries with High Energy Density and Cycling Stability. Advanced Functional Materials. 2023; 33(24). doi: 10.1002/adfm.202215065
56. Chu T, Zhou Z, Tian P, et al. Nanofluidic sensing inspired by the anomalous water dynamics in electrical angstrom-scale channels. Nature Communications. 2024; 15(1). doi: 10.1038/s41467-024-51877-7
57. Wu Y, Sun M. Recent progress of MXene as an energy storage material. Nanoscale Horizons. 2024; 2. doi: 10.1039/D3NH00402C
58. Liang X, Chen Y, Jiao Z, et al. MXene-transition metal sulfide composite electrodes for supercapacitors: Synthesis and electrochemical characterization. Journal of Energy Storage. 2024; 88: 111634. doi: 10.1016/j.est.2024.111634

59. Saravanan P, Rajeswari S, Kumar JA, et al. Bibliometric analysis and recent trends on MXene research – A comprehensive review. Chemosphere. 2022; 286: 131873. doi: 10.1016/j.chemosphere.2021.131873

Academic Publishing Pte. Ltd.

Add: 73 Upper Paya Lebar Road #07-02B-01 Centro Bianco Singapore 534818

Tel: +65 83184869

E-mail: editorial_office@acad-pub.com

Web: http://ojs.acad-pub.com/